



The MFiX Third Edition V and V Manual

Release Third Edition

MFS Development Group

Jan 13, 2021

TABLE OF CONTENTS

1	Header	1
1.1	List of Figures	2
1.2	List of Equations	2
1.3	List of Tables	2
2	Executive Summary	3
3	Introduction	5
3.1	Verification and Validation	5
3.2	Verification Test Selection Criteria	5
3.3	Testing Frequency	7
3.4	Case files and datasets	7
3.5	Organization	7
4	Method of Manufactured Solutions (MMS)	9
4.1	MMS Procedure Overview	10
4.2	MMS-EX01: One dimensional steady state Burger’s equation	13
4.3	MMS-EX02: One dimensional steady state heat equation	16
4.4	MMS-EX03: One dimensional transient heat equation	18
4.5	MMS01: Single-phase, 2D, sinusoidal functions	25
4.6	MMS02: Two-phase, 3D, curl-based functions with constant volume fraction	28
4.7	MMS03: Two-phase, 3D, curl-based functions with variable volume fraction	30
4.8	MMS04: No-slip wall BC, single-phase, 3D, curl-based functions	33
4.9	MMS05: Free-slip wall BC, single-phase, 3D, curl-based functions	34
4.10	MMS06: Pressure outflow BC, single-phase, 3D, curl-based functions	36
5	Fluid Model Code Verification Test Cases	39
5.1	FLD01: Steady, 2D Poiseuille flow	40
5.2	FLD02: Steady, 1D heat conduction	44
5.3	FLD03: Steady, lid-driven square cavity	46
5.4	FLD04: Gresho vortex problem	50
5.5	FLD05: Steady, 2D Couette flow	56
5.6	FLD06: Steady, 2D multi-component species transport	61
5.7	FLD07: Steady, 2D fully-developed, turbulent channel flow	64
5.8	FLD08: Steady, 2D turbulent pipe flow	67
6	MFIX-DEM Code Verification Test Cases	73
6.1	DEM01: Freely-falling particle	75
6.2	DEM02: Bouncing particle	79
6.3	DEM03: Two stacked, compressed particles	81
6.4	DEM04: Slipping on a rough surface	83

6.5	DEM05: Oblique particle collision	85
6.6	DEM06: Single particle, terminal velocity	88
7	MFIX-PIC Code Verification Test Cases	95
7.1	PIC01: Terminal velocity	95
7.2	PIC02: Advection in time varying flow field – velocity interpolation	97
7.3	PIC03: Advection in time varying flow field – parcel volume deposition	100
7.4	PIC04: Particle-Settling in Fluid	103
7.5	PIC05: Evaporation	108
7.6	PIC06: Rayleigh-Taylor Instability	111
7.7	PIC07: Minimum fluidization	112
8	Manufactured Solution Mathematical Forms	119
8.1	MMS02 manufactured solutions	121
8.2	MMS03 manufactured solutions	123
8.3	MMS04 manufactured solutions	124
8.4	MMS05 manufactured solutions	125
9	Analytical solution for particle-settling in fluid	127
10	References	131
A	MMS02 manufactured solutions	133
B	MMS03 manufactured solutions	135
C	MMS04 manufactured solutions	137
D	MMS05 manufactured solutions	139
	Bibliography	141

NETL

NATIONAL ENERGY TECHNOLOGY LABORATORY

MFIX Documentation Volume 3: Verification and Validation Manual Second Edition

November, 2018

Preliminary – Do not cite or quote

Office of Fossil Energy

NETL-PUB-22050



Disclaimer

This report was prepared as an account of work sponsored by an agency of the United States Government. Neither the United States Government nor any agency thereof, nor any of their employees, makes any warranty, express or implied, or assumes any legal liability or responsibility for the accuracy, completeness, or usefulness of any information, apparatus, product, or process disclosed, or represents that its use would not infringe privately owned rights. Reference therein to any specific commercial product, process, or service by trade name, trademark, manufacturer, or otherwise does not necessarily constitute or imply its endorsement, recommendation, or favoring by the United States Government or any agency thereof. The views and opinions of authors expressed therein do not necessarily state or reflect those of the United States Government or any agency thereof.

Cover Illustration: Describe cover photo

Suggested Citation: J. Musser, A. Vaidheeswaran, and M.A. Clarke, eds. *MFIX Documentation Volume 3: Verification and Validation Manual*; 2nd ed. NETL-PUB-22050; NETL Technical Report Series; U.S. Department of Energy, National Energy Technology Laboratory: Morgantown, WV, 2018.

Keywords:

MFIX; Verification; Validation; Multiphase; Method of Manufactured Solutions; Computational Fluid Dynamics; Discrete Element Method; Two-Fluid Model

MFIX Documentation Volume 3: Verification and Validation Manual

J. Musser¹, A. Vaidheeswaran^{1,2}, and M.A. Clarke^{1,2}

1 Research and Innovation Center, National Energy Technology Laboratory

2 West Virginia University Research Corporation

NETL-PUB-22050

November, 2018

NETL-PUB-22050

NETL Contacts:

J. Musser, Principal Investigator

William A. Rogers, Technical Portfolio Lead

Bryan Morreale, Executive Director, Research and Innovation Center

This page is intentionally blank.

1.1 List of Figures

1.2 List of Equations

Eq.4.1 Arbitrary Partial Differential Equation

Eq.4.2 Burger Equation

Eq.4.3 Burger Equation Representation

FIXME: etc.

1.3 List of Tables

Acronyms and Abbreviations

BC Boundary Condition

CFD Computational Fluid Dynamics

CV Control Volume

CI Continuous Integration

DEM Discrete Element Model

EE Eulerian-Eulerian

MFIX Multiphase Flow with Interphase eXchanges

MMS Method of Manufactured Solutions

MPPIC Multiphase Particle-In-Cell

PDE Partial Differential Equation

SQA Software Quality Assurance

TFM Two-Fluid Model

V&V Verification and Validation

UQ Uncertainty Quantification

EXECUTIVE SUMMARY

The MFIX Verification and Validation Manual aims to document verification tests and validation cases for the MFIX suite. Additionally, this manual attempts to capture best practices for verification and validation as part of a broader approach to software quality assurance. The goal is to perform a systematic verification of features available in MFIX for correctness and numerical accuracy.

Contributors:

(Alphabetical by last name)

Sofiane Benyahia

Aniruddha Choudhary

Mary Ann Clarke

Jean-François Dietiker

William Fullmer

Janine Galvin

Aytekin Gel

Chris Guenther

Tingwen Li

Mark Meredith

Aaron Morris

Jordan Musser

Thomas O'Brien

Sreekanth Pannala

William Rogers

Mehrdad Shahnam

Madhava Syamlal

Avinash Vaidheeswaran

The editors thank all contributors, especially our colleagues in the NETL Multiphase Flow Science Group, for their assistance and feedback in the creation and maintenance of this document.

INTRODUCTION

The MFIX Verification and Validation Manual, referred to herein as the V&V Manual, aims to document verification tests and validation cases for the MFIX suite. Additionally, this manual attempts to capture best practices for V&V as part of a broader approach to software quality assurance (SQA). The goal is to perform a systematic verification of features available in the code for correctness and numerical accuracy. Future work will include validation cases to assess the suitability of the physical models implemented within MFIX. The V&V Manual also serves as a guide for periodic and automated testing of the software by the developers.

3.1 Verification and Validation

For the purpose of this manual, the terms *verification* and *validation* are defined as follows [7]

- **Verification:** The process of determining that a numerical model implementation accurately represents the developer's conceptual description of the model and the mathematical solution to the model.
- **Validation:** The process of determining the degree to which a model is an accurate representation of the real world from the perspective of the intended uses of the model.

Roache [22] succinctly describes verification as an assessment on “solving the *equations right*” whereas validation is “solving the *right equations*.” Fig. 3.1 illustrates the relationship between verification and validation processes schematically.

Verification deals with the mathematics of the simulation and involves assessing the correctness of the computer code and numerical algorithms (i.e., code verification) as well as the accuracy of the numerical solution (i.e., solution verification). Validation deals with the physics of the problem and assesses whether the selected mathematical model satisfactorily predicts the physics of interest. Roache [24] further noted the distinction between verification and validation as, “Verification is a mathematics issue; not a physics issue.” Hence, verification precedes validation.

3.2 Verification Test Selection Criteria

Verification test cases are selected based upon the following criteria:

- Each test case should exercise one or more sub-models for a physical phenomenon
- Simulations must be computationally inexpensive to facilitate regular testing
- There should be minimal overlap between tests

The preference and thereby quality of a test is assessed on the following criteria:

- (Most preferable) Examination of numerical error between the exact solution and the numerical solution for problems where an analytical solution is available (i.e., verification using method of exact solutions) or a manufactured solution is obtainable

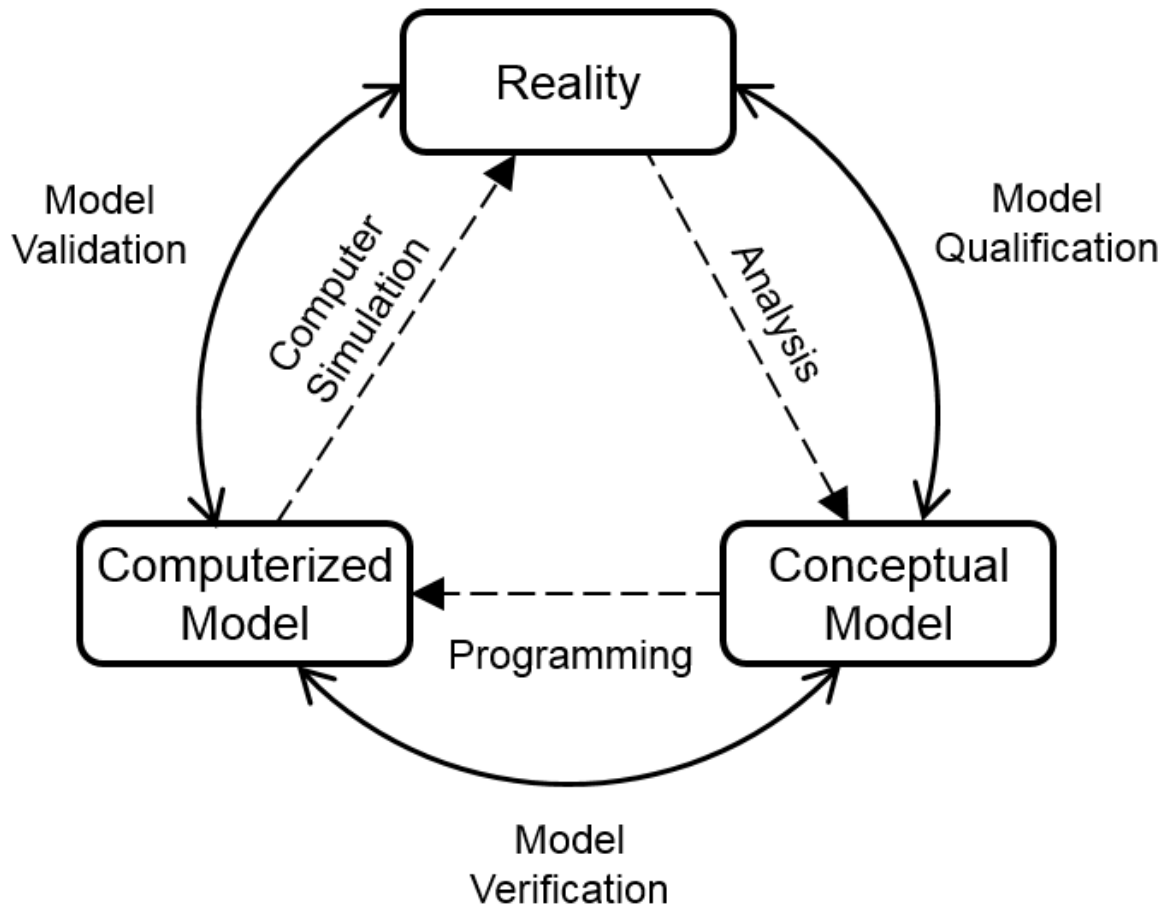


Fig. 3.1: Verification and validation process [28][18].

- (Less preferable) Comparison of numerical solutions to established results in literature (i.e., similar to validation, but using benchmark problems)
- (Least preferable) Comparison of numerical solutions to results obtained from previous versions of the same code (i.e., regression test) or from another verified code (i.e., code comparison)

3.3 Testing Frequency

Cases presented within this document are tested at various intervals as part of the SQA process. Before 2014, code integrity in MFiX was tracked through a series of nightly regression tests based on an open source software testing framework called QMTest, which provided a single snapshot on a daily basis [31]. This method was replaced by a continuous integration (CI) server for greater testing and archival flexibility.

Cases that execute quickly are tested whenever modifications are committed to the source code repository to quickly detect any issues generated by the changes. However, computationally burdensome verification and validation cases are tested less frequently to prevent overwhelming the CI server. A summary table at the start of each chapter indicates the frequency at which each case is tested.

3.4 Case files and datasets

Case files and datasets for the tests outlined in this document are provided with the MFiX source code under the **mfix/tests** directory. All presented data are representative of results from the current MFiX release unless explicitly noted.

3.5 Organization

Chapter 2 provides verification tests that use the Method of Manufactured Solution (MMS) to determine whether the observed order of error reduction with grid refinement matches the formal order. Order testing with MMS is considered to be a very rigorous procedure for code verification.

Chapter 3 provides verification and validation test cases using MFiX Fluid Model which represents the framework for solving gas-phase equations used in Two-Fluid Model (MFiX-TFM), Discrete Element Model (MFiX-DEM) and Particle-In-Cell (MFiX-PIC) model. Chapter 4 provides examples of verification problems using MFiX-DEM while verification and validation test cases using MFiX-PIC are presented in Chapter 5. Fig. 3.2 shows the scope of the V&V activity covered in this manual.

MFiX Verification and Validation Manual	Verification	Code Verification	<p>Method of Manufactured Solutions: Chapter 2</p> <ul style="list-style-type: none"> Mathematically rigorous method for testing order of accuracy Test implementation of baseline governing equations Applied to mathematical (i.e., non-physical) cases
			<p>Benchmark Problems: Chapters 3, 4 & 5</p> <ul style="list-style-type: none"> Solving simple ODEs and PDEs To test different aspects of MFiX Applied to problems with simplified physics having analytical solutions or well-documented results from literature
			<p>Unit Tests</p> <ul style="list-style-type: none"> Testing a software module for expected behavior To test correctness of various closure models
		Solution Verification	<p>Numerical Error Estimation</p> <ul style="list-style-type: none"> Assess errors due to grid size, time-step, iterative tolerance, round-off, statistical sampling etc. Applied to real-world problems
	Validation	Comparison of computational solution with high-quality experimental data (Chapters 3, 4 & 5)	
	Uncertainty Quantification	<ul style="list-style-type: none"> Identification and characterization of uncertainties in simulations Sensitivity analysis, PIRT (Phenomena Identification and Ranking Table) analysis Propagation of input uncertainties to quantify their effect on quantities of interest 	

Fig. 3.2: Scope of MFiX verification and validation activity covered in this manual. (Greyed parts indicate future or ongoing activities not presented in the current version of this document.)

METHOD OF MANUFACTURED SOLUTIONS (MMS)

Order of accuracy testing (or ‘order testing’) is considered a rigorous method for performing code verification. During order testing, the formal order of accuracy of a numerical scheme is compared to the observed order of accuracy. The observed order is the order at which the discretization error (which is the difference between the numerical solution to the discrete equations and the exact solution to the PDEs) decreases with systematic mesh refinement. However, the exact solution to a PDE is unknown for most practical problems. In this scenario, the Method of Manufactured Solutions (MMS) [23] can be used where a selected analytical function (called a ‘manufactured solution’) is forced to be the exact solution by modifying the PDE through additional source terms.

The MMS test cases presented in this chapter are summarized in [Table 4.1](#). These test cases offer an increasing level of computational complexity to isolate any potential problems in the source code. Three explanatory test cases that employ various simplifying assumptions are provided to assist the reader in understanding the MMS. Additional test cases were selected based upon their ability to invoke various parts of the MFIX code, and present physically acceptable data. All cases are executed in serial mode unless explicitly noted.

Table 4.1: Summary of MMS tests by feature.

	EX01	EX02	EX03	01	02	03	04	05	06
Frequency†	X	X	X	M	M	M	M	M	M
Dimension	1D	1D	1D	2D	3D	3D	3D	3D	3D
Multiphase					✓	✓			
Continuity				✓	✓				✓
Momentum	✓			✓	✓	✓	✓	✓	✓
Thermal Energy		✓	✓		✓	✓			
Species Mass									
Granular Energy					✓	✓			
Turbulence									
No-slip Wall BC							✓		
Free-slip Wall BC								✓	
Pressure Outflow									✓
Distributed Memory									
Shared Memory									

† C-Incorporated into the continuous integration server; M-Monthly; Q-Quarterly; D-Disabled; X-Manual

4.1 MMS Procedure Overview

To better instruct the reader, the procedure for using a MMS to conduct an order of accuracy test is summarized by example [26][19] :

1. Allow any partial differential equation in n-dimensions to be represented through the notation:

$$L[u(x_1, x_2, \dots, x_n, t)] = 0 \quad (4.1)$$

For example, a one-dimensional non-linear Burger equation:

$$u_t + uu_x = \alpha u_{xx} \quad (4.2)$$

would be represented as:

$$L[u(x, t)] = u_t + uu_x - \alpha u_{xx} = 0 \quad (4.3)$$

2. Make up a manufactured solution to the proposed partial differential equation. The chosen solution does not need to represent the solution to a physical problem. The MMS is a mathematical exercise to determine if a piece of software will accurately calculate a solution to its prescribed numerical order.

For example, allow: $U(x, t) = A + \sin(x + Ct)$ where A and C are constants, to be a solution to $L[u(x, t)]$.

The key is that whatever one chooses for $U(x, t)$, it must be mathematically analytic, meaning fully differentiable with continuous derivatives to at least the order of the partial differential equation one is trying to solve over the full domain of the problem. In this example, the constant value function A and the sinusoidal function $\sin(x + Ct)$ obviously meet these criteria. Do not choose functions that display discontinuities of any type for any derivative if the domain of interest extends *through* those discontinuities. In addition, it is important that all terms in a given manufactured solution are of similar magnitude. This assures that solutions are not dominated by a single term which might skew order of accuracy results.

It is essential to choose solutions that do not engage physical constraints within the code that is under evaluation. For example, MFiX issues an error message and stops all calculations if the temperature in any computational cell falls below 250 Kelvin. So, if testing the energy equation, the manufactured solution should never present a value less than 250, as this value is contextually interpreted as an unphysical temperature.

3. Apply the manufactured solution to the partial differential equation being solved. This means create the derivatives represented in the original problem and substitute them into the equation.

For example, using $U(x, t) = A + \sin(x + Ct)$ as a manufactured solution for $L[u(x, t)] = u_t + uu_x - \alpha u_{xx} = 0$ requires

$$L[u(x, t)]_{U(x, t)} = \frac{\partial}{\partial t}(U(x, t)) + U(x, t) \frac{\partial}{\partial x}(U(x, t)) - \alpha \frac{\partial^2}{\partial x^2}(U(x, t)) = 0 \quad (4.4)$$

After substitution,

$$L[u(x, t)]_{U(x, t)} = C \cos(x + Ct) + (A + \sin(x + Ct))(\cos(x + Ct)) - \alpha(-\sin(x + Ct)) = 0 \quad (4.5)$$

Or,

$$L[u(x, t)]_{U(x, t)} = (A + C) \cos(x + Ct) + \sin(x + Ct) \cos(x + Ct) + \alpha \sin(x + Ct) = 0 \quad (4.6)$$

$L[u(x, t)]_{U(x, t)}$ represents what are called *source terms* in MMS. Thinking about this using notation:

$$L[u(x, t)] = 0 = L[u(x, t)]_{U(x, t)} \quad (4.7)$$

Or,

$$L[u(x, t)] - L[u(x, t)]_{U(x, t)} = 0 \quad (4.8)$$

After calculation, any arithmetic difference between the numerical solution and the exact solution is assumed to originate from the numerical method.

4. To properly solve a partial differential equation of the form $L[u(x_1, x_2, \dots, x_n, t)] = 0$, one needs appropriately chosen initial and boundary values.

So, by example, assume that the physical domain of interest is $x \in [0, 1]$ and allow $t \in [0, \infty)$.

First, force the initial condition of $u(x, 0)$ to align with that of the manufactured solution, $U(x, 0)$ by choosing,

$$u(x, 0) = U(x, 0) = A + \sin(x + C(0)) = A + \sin(x) \quad (4.9)$$

Then, select boundary conditions in any meaningful way, forcing alignment between the proposed partial differential equation and the manufactured solution. For example, perhaps fixed boundary conditions are useful. These are sometimes called Dirichlet boundary conditions. Applying a fixed boundary condition means choose functions for fixed boundary locations that will be maintained through all time-steps. It does not mean that a boundary must have the same value for all time, although that is a possibility (the function chosen might be a constant).

So, for this example, an appropriate fixed boundary condition would be:

$$\begin{aligned} u(0, t) &= U(0, t) = A + \sin(0 + Ct) = A + \sin(Ct) \\ u(1, t) &= U(1, t) = A + \sin(1 + Ct) \end{aligned} \quad (4.10)$$

Note that in this example, the *fixed* (Dirichlet) boundary condition varies with time.

The type of boundary condition is insignificant to the method of manufactured solutions. One can easily choose Neumann (flux conditions at the boundary), Cauchy (a mix of fixed conditions and at least one derivative in the direction of the normal of the boundary), Robin (weighted combinations of Neumann and Dirichlet conditions over all boundaries) or mixed conditions (different boundary condition types on different subsets of the boundary) as each partial differential equation application is explored.

By example, a different solution to our proposed problem will occur if we shift to a *mixed* boundary condition such that:

$$\begin{aligned} u(0, t) &= U(0, t) = A + \sin(0 + Ct) = A + \sin(Ct) \text{ (Dirichlet)} \\ \frac{\partial}{\partial x}(u(1, t)) &= \frac{\partial}{\partial x}(U(1, t)) = \frac{\partial}{\partial x}(A + \sin(1 + Ct)) = \cos(1 + Ct) \text{ (Neumann)} \end{aligned} \quad (4.11)$$

In this way, the method of manufactured solutions allows the investigator to examine how the application of different boundary conditions affects the overall veracity of numerical approximations within the context of problems where solutions can be found through explicit hand calculation.

5. Theoretically, when a manufactured exact solution is known, computer algorithms applied to imitate that result should converge systematically toward *exactness* as the calculation space is ever more refined. Ideally, one might expect an eventual numerical result to differ from an exact solution by no more than \mathcal{O} (machine epsilon). Of course, the theoretical threshold of solution quality varies widely from this value as there are few calculations that can be held to such a high standard. For example, computers estimate all transcendental functions with truncated power series on computers, regardless of what a programmer types into code, and these functions are inherently burdened with this approximation error.

However, one can systematically refine a mesh and recalculate the solution to proposed problems in search of exactness. Once the arithmetic difference between the discretized solution and a manufactured solution remains constant, regardless of further mesh refinement, one has discovered the best numerical solution possible for a given code and a given problem. If the error between discretized solution and manufactured solution is acceptable by some standard, a code can be considered numerically *verified*. Note that this verification is limited to those code components invoked when setting up a MMS. As is the case for MFiX, most codes are far too complex to complete a full verification in a single MMS.

6. Global discretization error, DE_{\downarrow} , is the arithmetic difference between the computer (approximate or discrete) evaluation of the manufactured solution to a by hand (exact) solution. The script \downarrow is to remind the user of mesh \downarrow level.

Rather than evaluate discretization error one cell at a time, one can further consider global discretization error through various mathematical norms. An L_1 norm is an average absolute error over all cell locations ($ijk = 1, \dots, n$) in a calculation represented through an absolute difference.

$$L_1 : \quad \|\text{DE}_{\uparrow}\|_1 = \frac{\sum_{ijk=1}^n |\text{DE}_{\uparrow,ijk}|}{n} \quad (4.12)$$

An L_2 norm is a root mean square error over all cell locations ($ijk = 1, \dots, n$).

$$L_2 : \quad \|\text{DE}_{\uparrow}\|_2 = \sqrt{\frac{\sum_{ijk=1}^n |\text{DE}_{\uparrow,ijk}|^2}{n}} \quad (4.13)$$

An L_∞ norm is the maximum error in any single cell location ($ijk = 1, \dots, n$).

$$L_\infty = \|\text{DE}_{\uparrow}\|_\infty = |\text{DE}_{\uparrow,ijk}| \quad (4.14)$$

7. As mesh size, h , changes, one collects the normed values of global discretization error and applies them to create an observed order, p .

$$p = \frac{\ln\left(\frac{\|\text{DE}_{\uparrow+1}\|}{\|\text{DE}_{\uparrow}\|}\right)}{\ln\left(\frac{h_{\uparrow+1}}{h_{\uparrow}}\right)} = \frac{\ln\left(\frac{\|\text{DE}_{\uparrow+1}\|}{\|\text{DE}_{\uparrow}\|}\right)}{\ln(r)} \quad (4.15)$$

In this notation, mesh level, \uparrow , is largest at the coarsest mesh, and smallest at the most refined mesh. One will also see the observed order formula where the ratio between two mesh sizes (as seen in the denominator of p) is called a mesh refinement factor, r . Furthermore, the term *grid size measure*, \check{h} , is a ratio formed by comparing the number of divisions making up the finest mesh to the current mesh. Fig. 4.1 works to clarify these definitions within the context of observed order, and illustrates an observed order plot where $r = 2$, between subsequent mesh levels. Note that the use of grid size measure eliminates the need for any units in graphical representations of observed order.

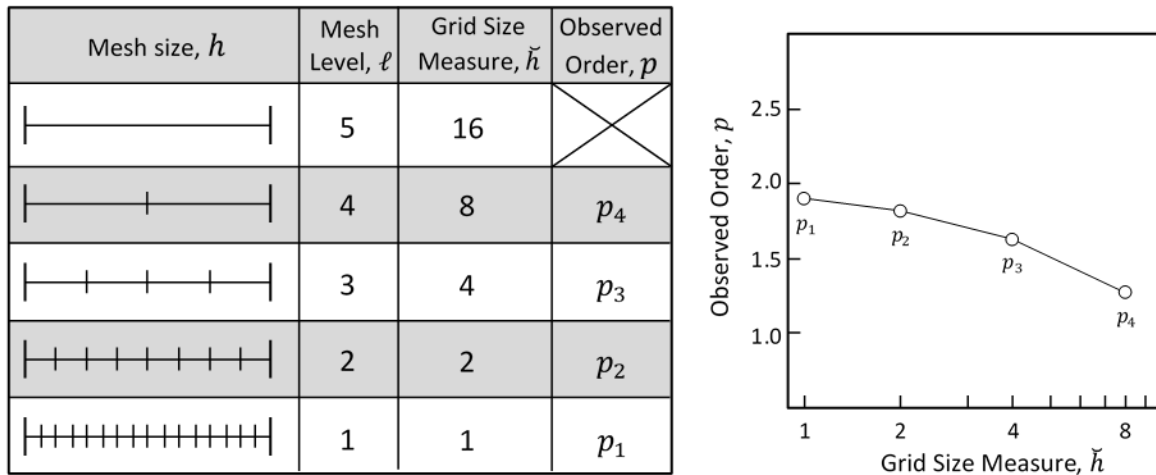


Fig. 4.1: Procedure for order of accuracy testing.

Ideally, one makes as many simulations as necessary to show that p is constant, thereby inferring that the best possible numerical solution has been made, and further simulation is unwarranted.

Note that the norm chosen for the calculation of observed order may affect the outcome of this assessment. For example, the most challenging norm related above is L_∞ , as it isolates the largest error in any given simulation. The least challenging norm is L_1 , as it will most easily mask localized high level error with areas of good agreement across any given domain.

4.2 MMS-EX01: One dimensional steady state Burger's equation

4.2.1 Description

The gas-phase momentum equations in MFIX have the following generalized form:¹

$$\frac{\partial}{\partial t} (\varepsilon_g \rho_g u_{gi}) + \frac{\partial}{\partial x_j} (\varepsilon_g \rho_g u_{gj} u_{gi}) = -\frac{\partial P_g}{\partial x_i} + \frac{\partial \tau_{gij}}{\partial x_j} + \varepsilon_g \rho_g g_i + \mathcal{S}_{gi} \quad (4.16)$$

where,

$$\tau_{gij} = 2\mu_g \left[\frac{1}{2} \left(\frac{\partial u_{gi}}{\partial x_j} + \frac{\partial u_{gj}}{\partial x_i} \right) - \frac{1}{3} \frac{\partial u_{gk}}{\partial x_k} \delta_{ij} \right] \quad (4.17)$$

To build on the previous example, the momentum equations can be recast as the one-dimensional steady state Burger's equation by imposing the following simplifying assumptions:²

1. A steady state simulation is needed to remove the momentum equations' transient term.
2. Calculations are restricted to one dimension.
3. The domain is of unit length in the x-axial direction: $x \in [0, 5]$.
4. The gas volume fraction and density are set to one, $\varepsilon_g = 1$ and $\rho_g = 1$.
5. The gas viscosity is chosen as $\mu_g = 3/4$.
6. Gravity and all other source terms are set to zero, $g = 0$ and $\mathcal{S}_{gi} = 0$.
7. Finally, because the pressure solver is integrated with the momentum equations, it is important to decouple the pressure correction step from the calculation.

The momentum equations with the above simplifications reduce to the one-dimensional Burger's equation,

$$u_g \frac{\partial u_g}{\partial x} - \frac{\partial^2 u_g}{\partial x^2} = 0 \quad (4.18)$$

where the subscript indicating dimensionality has been dropped for notational clarity.

Following the method of manufactured solutions, the partial differential equation is recast as:

$$L(x) = uu_x - u_{xx} \quad (4.19)$$

MMS requires the selection of a manufactured solution. Arbitrarily, choose any suitable analytic form of appropriate continuous, differential order. In this case, note that whatever manufactured solution is chosen must be continuously differentiable through its second derivative. Aside from asymptotic functions that may exhibit unphysical local changes, most any analytic function will be a suitable choice for this application. So, keeping things simple, as in the prior explanation,

$$U(x) = 0.5 + \sin(x) \quad (4.20)$$

Then, apply this form to $L(x)$:

$$L(x)_{U(x)} = (0.5 + \sin(x)) \frac{\partial}{\partial x} (0.5 + \sin(x)) - \frac{\partial^2}{\partial x^2} (0.5 + \sin(x)) \quad (4.21)$$

$$L(x)_{U(x)} = (0.5 + \sin(x)) (\cos(x)) - (-\sin(x)) \quad (4.22)$$

¹ The conservative form of the fluid momentum equations is presented here, however, the non-conservative form is solved in MFIX. The non-conservative form is obtained by subtracting the continuity equation from the conservative form.

² Assumptions that reduce model complexity are typically avoided when using the MMS. However, this example intentionally simplifies the momentum equations to make the example easier to follow.

$$L(x)_{U(x)} = 0.5 \cos(x) + \cos(x) \sin(x) + \sin(x) \quad (4.23)$$

Finally, cast appropriate initial and/or boundary conditions. For this case, since time is inconsequential, no initial condition is warranted. Focus then shifts to boundary conditions. With the domain of interest being $x \in [0, 1]$, fixed boundary conditions are given by:

$$\begin{aligned} U(0) &= 0.5 + \sin(0) = 0.5 \\ U(1) &= 0.5 + \sin(5) \end{aligned} \quad (4.24)$$

4.2.2 Setup

Initially, only the x-direction momentum equation on a domain with unit dimensions is considered. Subsequently, the setup is executed in the y- and z- directions to determine if problem orientation influences the observed order.

Table 4.2: MMS-EX01 Setup, Initial and Bounday Conditions.

Computational/Physical model		
1D, Steady-state, incompressible		
Single-phase (no solids)		
No gravity		
Turbulence equations are not solved (Laminar)		
Uniform mesh		
Central scheme		
Geometry		
Coordinate system	Cartesian	
Domain length, $L(x)$	1.0	(m)
Material [†]		
Fluid density, ρ_g	1.0	($\text{kg}\cdot\text{m}^{-3}$)
Fluid viscosity, μ_g	0.75	($\text{Pa}\cdot\text{s}$)
Initial Conditions		
Pressure (<i>gauge</i>), P_g	0.0	(Pa)
Fluid x-velocity, u_g	1.0	($\text{m}\cdot\text{sec}^{-1}$)
Boundary Conditions [‡]		
East/West (x)	Mass inflow (MMS)	
All other boundaries	Cyclic	

[†] Material properties selected to ensure comparable contribution from convection and diffusion terms.

[‡] The manufactured solution imposed on the east / west boundaries is given by Eq.4.24.

User-defined functions specific to the MMS implementation in MFIX are used to introduce the source term. Specifically, for each discretized x-momentum computational cell, equation Eq.4.23 is evaluated and subtracted from the right hand side of the linear equation. Once the simulation has converged, the L_1 , L_2 and L_∞ error norms are computed by referencing equation Eq.4.24.

4.2.3 Results

Following the outline of MMS methodology, three separate 1-dimensional systems (x, y and z) were created, each having 4, 8, 16, 32, 64, and 128 cells, using the steady state Burger’s equation and manufactured solution previously described.

An observed order for each direction is calculated using L_1 , L_2 and L_∞ error norms. The following tables and figure illustrate these data. One can quickly see from the tabled L -norms and subsequently calculated observed order that direction does not have a large influence on these values. All data points to a 2nd order (p) convergence of the steady state Burger’s equation using MFIX. In the present input-deck construction, whereby the numerical method implemented is *central differencing* method, this is the best outcome to expect.

Table 4.3: Observed Order, p , for steady state Burger’s equation using $U(x) = 1 + \sin(x)$ on $0 \leq x \leq 1$.

Mesh	L_1 -norm	L_2 -norm	L_∞ -norm	$p(L_1)$	$p(L_2)$	$p(L_\infty)$
4	2.4834E-01	2.5853E-01	3.1909E-01	N/A	N/A	N/A
8	5.2081E-02	5.3318E-02	7.0000E-02	2.2535	2.2776	2.1886
16	1.1771E-02	1.2317E-02	1.6652E-02	2.1455	2.1139	2.0716
32	2.8250E-03	2.9965E-03	4.1128E-03	2.0589	2.0393	2.0176
128	6.9383E-04	7.4135E-04	1.0251E-03	2.0256	2.0151	2.0043

Hence, these data imply that the terms engaged in the momentum equation through the evaluation of the steady state Burger’s equation are numerically closed on 2nd order approximations which is correct and *verified* by the method of manufactured solutions.

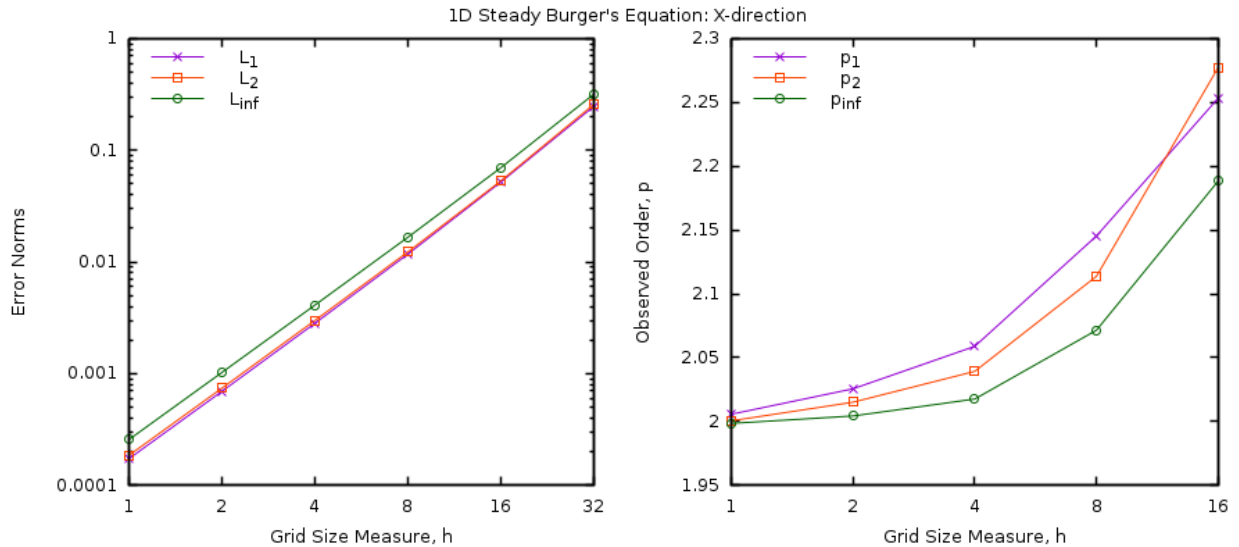


Fig. 4.2: Observed Order, MMS Solution to 1-D steady state Burger’s equation in MFIX, using $U(x) = 1 + \sin(x)$ on $0 \leq x \leq 1$.

As a final observation, note that observed order appears to increase with decreasing spatial mesh. However, *as expected*, L -norms decrease with increasing mesh density, indicating a better overall solution.

4.3 MMS-EX02: One dimensional steady state heat equation

4.3.1 Description

The gas phase energy equations in MFIX are:

$$\varepsilon_g \rho_g C_{pg} \left[\frac{\partial T_g}{\partial t} + U_{gi} \frac{\partial T_g}{\partial x_j} \right] = - \frac{\partial}{\partial x_j} \left(-\varepsilon_g \kappa_g \frac{\partial T_g}{\partial x_j} \right) - \sum_{n=1}^{N_g} h_{gn} R_{gn} + \mathcal{S}_g \quad (4.25)$$

The energy equations can be recast as the one-dimensional heat equation by imposing the following simplifying assumptions:³

1. A steady state simulation is needed to remove the energy equations' transient term.
2. Calculations are restricted to one dimension.
3. The domain length in the x-axial direction is $x \in [0, 5]$.
4. The gas volume fraction, density, thermal conductivity, and specific heat are set to one, $\varepsilon_g = 1$, $\rho_g = 1$, $\kappa_g = 1$, and $C_{pg} = 1$.
5. The gas momentum equations are not solved and initial velocity field is set to zero so that the convective term is zero.
6. There are no chemical reactions, interphase mass transfer or other sources of energy implying: $\sum_{n=1}^{N_g} h_{gn} R_{gn} + \mathcal{S}_g = 0$.

On re-evaluation of the energy equations, the following one-dimensional form (aka the steady state heat equation) emerges:

$$\frac{\partial^2 T_g}{\partial x^2} = 0 \quad (4.26)$$

Following the method of manufactured solutions, the partial differential equation is recast as:

$$L(x) = (T_g)_{xx} = 0 \quad (4.27)$$

MMS requires the selection of a manufactured solution. Because this is a steady-state form, the manufactured solution is chosen not to incorporate a time variable for simplicity. Arbitrarily, choose any suitable analytic form of appropriate continuous, differential order. In this case, observe that whatever manufactured solution we choose must be continuously differentiable through its second spatial derivative. Also note, in MFIX, temperature is calculated absolutely and is restricted as: $250 < u < 4000$ (which represents the Kelvin scale). Values outside of these bounds cause a fatal error within the code. So, in this case, there is a caveat that requires the manufactured solution chosen cannot present out-of-bound values on any domain of interest. In this example, the domain, $0 \leq x \leq 5$, and the manufactured solution:

$$T_g(x) = 500 + (1 + x^3) = 501 + x^3 \quad (4.28)$$

work within the MFIX constraints. Continuing to follow the MMS, this solution is applied to $L(x)$:

$$L(x)_{T_g(x)} = \frac{\partial^2}{\partial x^2} (501 + x^3) \quad (4.29)$$

$$L(x)_{T_g(x)} = 6x \quad (4.30)$$

Then, appropriate initial and/or boundary conditions are cast. For this case, since time is inconsequential, no initial condition is warranted. Focus then shifts to boundary conditions.

On the domain of interest: $x \in [0, 5]$, Dirichlet boundary conditions are:

$$\begin{aligned} T_g(0) &= 501 + 0^3 = 501 \\ T_g(5) &= 501 + 5^3 = 501 + 125 = 626 \end{aligned} \quad (4.31)$$

³ Again, simplifying assumptions are typically avoided when using the MMS. However, this example intentionally simplifies the energy equations to make the example easier to follow.

4.3.2 Setup

This case is designed to test the energy equation implementation.

Table 4.4: MMS-EX02 Setup, Initial and Boundary Conditions.

Computational/Physical model		
1D, Steady-state, incompressible		
Single-phase (no solids)		
No gravity		
Turbulence equations are not solved (Laminar)		
Uniform mesh		
Central scheme		
Geometry		
Coordinate system	Cartesian	
Domain length, L (x)	5.0	(m)
Material [†]		
Fluid density, ρ_g	1.0	($\text{kg}\cdot\text{m}^{-3}$)
Fluid viscosity, μ_g	1.0	(Pa·s)
Fluid specific heat, C_{pg}	1.0	($\text{J}\cdot\text{kg}^{-1}\cdot\text{K}^{-1}$)
Initial Conditions		
Pressure (<i>gauge</i>), P_g	0.0	(Pa)
Temperature, T_g	550.0	(K)
Boundary Conditions [‡]		
East/West (x)	(MMS)	
All other boundaries	Adiabatic Walls	

[†] Material properties selected to ensure comparable contribution from convection and diffusion terms.

[‡] The manufactured solution imposed on the east / west boundaries is given by Eq.4.31.

User defined functions specific to the MMS implementation in MFIX are used to introduce the source term. Specifically, for each computational cell, Eq.4.30 is evaluated and subtracted from the right hand side of the linear equation. Once the simulation has converged, the L_1 , L_2 and L_∞ error norms are computed by referencing Eq.4.28.

4.3.3 Results

Following the outline of MMS methodology, three separate 1-dimensional systems (x, y and z) were created, each having 8, 16, 32, 64, 128, and 256 cells, using the steady state heat equation and manufactured solution previously described.

An observed order for each direction is calculated using L_1 , L_2 and L_∞ error norms. The following tables and figure illustrate these data. One can quickly see from the tabled L -norms and subsequently calculated observed order that direction does not have a large influence on these values. All data points to a 2nd order (p) convergence of the steady state heat equation using MFIX.

Hence, these data imply that the diffusion term engaged in the energy equation through the evaluation of the steady state heat equation is numerically closed on 2nd order approximations which is correct and *verified* by the method of manufactured solutions.

Table 4.5: Observed Order, p , for steady state heat equation using $U(x) = 501 + x^3$ on $0 \leq x \leq 5$.

Mesh	L_1 -norm	L_2 -norm	L_∞ -norm	$p(L_1)$	$p(L_2)$	$p(L_\infty)$
8	7.3242E-01	8.4407E-01	1.3733E+00	N/A	N/A	N/A
16	1.8311E-01	2.1133E-01	3.5477E-01	2.0000	1.9979	1.9527
32	4.5776E-02	5.2852E-02	9.0122E-02	2.0000	1.9995	1.9769
64	1.1444E-02	1.3214E-02	2.2709E-02	2.0000	1.9999	1.9886
128	2.8610E-03	3.3036E-03	5.6997E-03	2.0000	2.0000	1.9943
256	7.1525E-04	8.2590E-04	1.4277E-03	2.0000	2.0000	1.9972

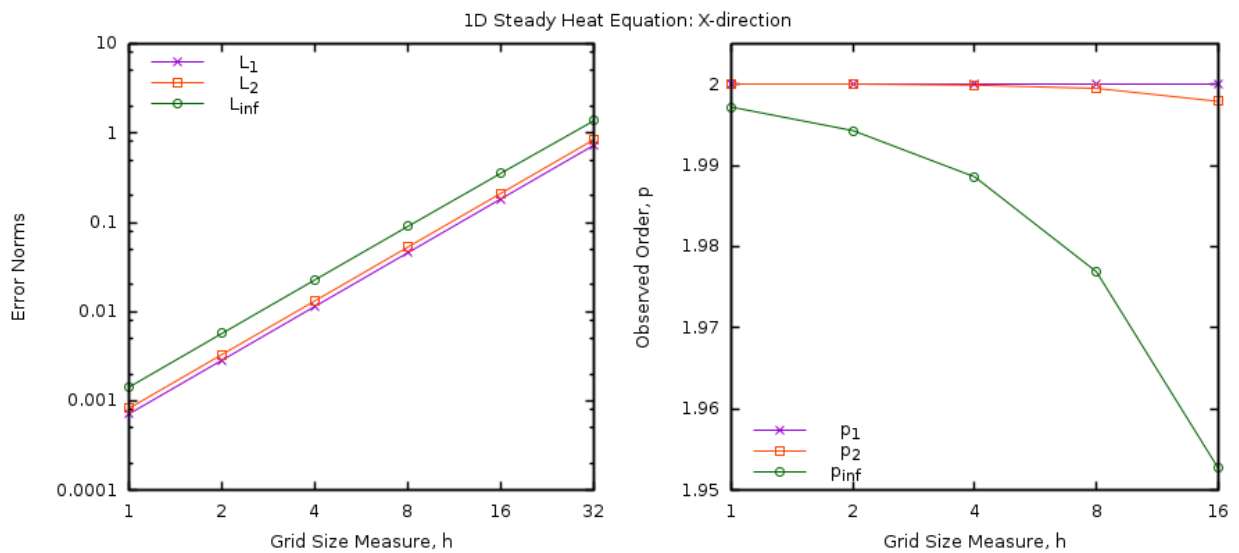


Fig. 4.3: Observed Order, MMS Solution to 1-D steady state heat equation in MFIX, using $U(x) = 501 + x^3$ on $0 \leq x \leq 5$.

4.4 MMS-EX03: One dimensional transient heat equation

4.4.1 Description

Again consider the gas phase energy equations in MFIX given by equation (2-25) in the previous example. The energy equations can be recast as the 1-dimensional transient heat equation by imposing the following simplifying assumptions:

1. Calculations are restricted to one dimension.
2. The domain length in the x -axial direction is $x \in [0, 1]$.
3. The gas volume fraction, density, thermal conductivity, and specific heat are set to one, $\varepsilon_g = 1$, $\rho_g = 1$, $\kappa_g = 1$, and $C_{pg} = 1$.
4. The gas momentum equations are not solved and initial velocity field is set to zero so that the convective term is zero.

5. There are no chemical reactions, interphase mass transfer or other sources of energy implying: $\sum_{n=1}^{N_g} h_{gn} R_{gn} + S_g = 0$.

On re-evaluation of the energy equations, the following one-dimensional form (aka the transient heat equation) emerges:

$$\frac{\partial T_g}{\partial t} - \frac{\partial^2 T_g}{\partial x^2} = 0 \quad (4.32)$$

Following the MMS approach, the partial differential equation is recast as:

$$L(x, t) = \frac{\partial T_g}{\partial t} - \alpha \frac{\partial^2 T_g}{\partial x^2} = 0 \quad (4.33)$$

As MMS requires the selection of a manufactured solution, a suitable analytic form of appropriate continuous, differential order is chosen. In this case, note that whatever manufactured solution is picked must be continuously differentiable through its second spatial derivative and first temporal derivative. In addition, for illustrative purposes, the manufactured solution is chosen so that time will appear in the boundary conditions. For simplicity, MMS-EX02 is modified by incorporating a time value, t , as:

$$T_g(x, t) = T_{g0} + T_{gx} \cos(A_{T_{gx}} \pi x) + T_{gt} \cos(A_{T_{gt}} \pi t) + T_{gtx} \cos(A_{T_{gtx}} \pi t x) \quad (4.34)$$

with a simple domain: $\{t \geq 0, 0 \leq x \leq 1\}$.

Then, this form is applied to $L(x, t)$:

$$L(x, t)_{T_g(x, t)} = \frac{\partial}{\partial t} T_g(x, t) - \alpha \frac{\partial^2}{\partial x^2} T_g(x, t) \quad (4.35)$$

$$\begin{aligned} L(x, t)_{T_g(x, t)} = & -T_{gt} (A_{T_{gt}} \pi) \sin(A_{T_{gt}} \pi t) - T_{gtx} (A_{T_{gtx}} \pi x) \sin(A_{T_{gtx}} \pi t x) \\ & + \alpha T_{gx} (A_{T_{gx}} \pi)^2 \cos(A_{T_{gx}} \pi x) + \alpha T_{gtx} (A_{T_{gtx}} \pi)^2 \cos(A_{T_{gtx}} \pi t x) \end{aligned} \quad (4.36)$$

Then, appropriate initial and/or boundary conditions are cast. For this case, an appropriate initial condition is:

$$T_g(x, 0) = T_{g0} + T_{gx} \cos(A_{T_{gx}} \pi x) + T_{gt} + T_{gtx} \quad (4.37)$$

Focus then shifts to boundary conditions. On the spatial domain of interest: $x \in [0, 1]$, boundary conditions become:

$$\begin{aligned} T_g(0, t) &= T_{g0} + T_{gx} + T_{gt} \cos(A_{T_{gt}} \pi t) + T_{gtx} \\ T_g(1, t) &= T_{g0} + T_{gx} \cos(A_{T_{gx}} \pi) + T_{gt} \cos(A_{T_{gt}} \pi t) + T_{gtx} \cos(A_{T_{gtx}} \pi t) \end{aligned} \quad (4.38)$$

Note that these boundary conditions, while Dirichlet in nature, are dependent on time. The parameters chosen in the manufactured solution are summarized below:

Table 2-4: Parameters used in MMS applied to transient heat conduction

Table 4.6: Parameters used in MMS applied to transient heat conduction

T_{g0}	500 K
T_{gx}	10 K
T_{gt}	100 K
T_{gtx}	10 K
$A_{T_{gx}}$	2.0
$A_{T_{gt}}$	2.0
$A_{T_{gtx}}$	2.0

4.4.2 Setup

This case is designed to test the energy equation implementation.

Table 4.7: MMS-EX03 Setup, Initial and Boundary Conditions.

Computational/Physical model		
1D, Steady-state, incompressible		
Single-phase (no solids)		
No gravity		
Turbulence equations are not solved (Laminar)		
Uniform mesh		
Central scheme		
Geometry		
Coordinate system	Cartesian	
Domain length, L (x)	1.0	(m)
Material [†]		
Fluid density, ρ_g	1.0	(kg·m ⁻³)
Fluid viscosity, μ_g	1.0	(Pa·s)
Fluid specific heat, C_{pg}	1.0	(J·kg ⁻¹ ·K ⁻¹)
Initial Conditions		
Pressure (<i>gauge</i>), P_g	0.0	(Pa)
Temperature, T_g	Set with user routine	(K)
Boundary Conditions [‡]		
East/West (x)	(MMS)	
All other boundaries	Adiabatic Walls	

[†] Material properties selected to ensure comparable contribution from convection and diffusion terms.

[‡] The manufactured solution imposed on the east / west boundaries is given by equation (2-38). In this case, because boundary conditions change with time, they must be managed by creating a user-defined function (in MFiX, update the standard function `usr1.f`).

User defined functions specific to the MMS implementation in MFiX are used to introduce the source term. Specifically, for each computational cell, equation (2-36) is evaluated and subtracted from the right hand side of the linear equation. Once the simulation has converged, the L_1 , L_2 and L_∞ error norms are computed using equation (2-34).

4.4.3 Analysis variation for mixed variable problems

When analyzing a problem where both transient and spatial order verification must be conducted simultaneously, care must be taken with problem set up. As a first step, to examine temporal order, spatial discretization must be held constant (fixed grid); then, to examine spatial order, temporal discretization must be held constant (fixed time step). Holding either discretization at a constant level introduces a fixed error that applies to all calculations in that group. In a problem such as this, one imagines discretization error as being in two parts:

$$DE = DE_{\text{temporal}} + DE_{\text{spatial}} \quad (4.39)$$

When one of these errors is constant, the normed error that is collected to represent overall discretization error contains that constant, albeit one cannot preconceive its value. For example, consider that time step is held constant, and that this

choice results in constant temporal discretization error, k :

$$\|DE\| = \|k + DE_{\text{spatial}}\| \quad (4.40)$$

Note that the existence of k destroys the notion of equation (2-15) for calculating a one-variable observed order by masking DE_{spatial} . To eliminate the effect of k , observed order, \hat{p} , must be calculated in such a way as to naturally remove its presence. This can be done through subtraction as:

$$\hat{p} = \frac{\ln \left(\frac{\|DE_{\uparrow+2}\| - \|DE_{\uparrow+1}\|}{\|DE_{\uparrow+1}\| - \|DE_{\uparrow}\|} \right)}{\ln(r)} \quad (4.41)$$

with the caveat that at least 3 levels of spatial mesh are needed to isolate \hat{p} . Then, a similar calculation can be conducted by refining time step and using a fixed spatial mesh.

If the reader now allows themselves a *thought experiment*, they might be curious how error might manifest itself when the observed order associated with space and the observed order associated with time are equal or non-equal. If equal, and a naïve approach to order calculation is made, one might not detect that an analysis like (2-15) is invalid. However, when non-equal, the naïve approach will result in utter confusion. (Yes, we did it.)

To run a combined analysis without the above step where either temporal or spatial discretization is held constant, [19] provides a useful table illustrating refinement factors needed to accurately isolate observed order of spatially and temporally mixed problems in two discretization levels instead of three, by assuring that the spatial and temporal discretization error terms are scaled together as solutions approach their asymptotic range. A portion of that table is given here, as it applies to the problem at hand, where the expectation is a spatial order of 2, and a temporal order of 1.

Table 4.8: Mixed analysis refinement factors [Ober_book]; highlighted row for expected spatial order =2, and expected temporal order = 1 based on known MFiX routines

Expected p	Expected q	r_x	r_t	Error ratio
2	1	2	4	4
2	2	2	$\sqrt[2]{4}$	4
2	3	2	$\sqrt[3]{4}$	4
2	4	2	$\sqrt[4]{4}$	4

Likewise, Richards [21] summarily defines $r_t = (r_x)^{\frac{p}{q}}$. Using the suggestions from this table (formula) for an expected spatial order, $p = 2$, and an expected temporal order, $q = 1$, a calculated observed spatial order, \hat{p} , and a calculated observed temporal order, \hat{q} are computed as described in [19]:

$$\hat{p} = \frac{\ln \left(\frac{\|DE_{t+1}\|}{\|DE_t\|} \right)}{\ln(r_x)}, \hat{q} = \frac{\ln \left(\frac{\|DE_{t+1}\|}{\|DE_t\|} \right)}{\ln(r_t)} \quad (4.42)$$

In the following result section, the calculations derived from both methodologies are illustrated.

4.4.4 Results

Both methodologies described in section 2.4.3 were implemented to examine temporal and spatial orders of accuracy in the transient heat equation as it applies to MFiX.

Temporal order of accuracy

The temporal order of accuracy is determined by fixing the grid size and performing simulations by reducing the time step size. In this case, with spatial domain set to $x \in [0, 1]$, 16 cells were used corresponding to a coarse discretization. Expectation is that spatial error was significant.

The following time step sizes were used: 1.25E-4s, 6.25E-5s, 3.13E-5s, 1.56E-5s, 7.81E-6s, and 3.91E-6s, resulting in a refinement factor, r , equal to 2. The observed order of accuracy, \hat{p} , converges to 1 which is equal to the formal order of the first-order Euler time stepping method utilized in MFIX.

Table 4.9: L norms and the observed order for the unsteady heat equation – temporal order of accuracy⁴

h	L_1 -norm	L_2 -norm	L_∞ -norm	$q(L_1)$	$q(L_2)$	$q(L_\infty)$
1	9.4156E-02	1.1189E-01	1.9267E-01	1.00	0.95	1.00
2	9.4175E-02	1.1182E-01	1.9260E-01	1.00	0.90	1.00
4	9.4214E-02	1.1168E-01	1.9244E-01	1.00	0.77	1.00
8	9.4291E-02	1.1143E-01	1.9214E-01	1.00	0.36	1.00
16	9.4444E-02	1.1101E-01	1.9153E-01	N/A	N/A	N/A
32	9.4751E-02	1.1047E-01	1.9031E-01	N/A	N/A	N/A

An example calculation, using $h = 1, 2, 4$ and L_1 -norm is given:

$$\hat{q} = \frac{\ln\left(\frac{\|DE_{\downarrow+2}\| - \|DE_{\downarrow+1}\|}{\|DE_{\downarrow+1}\| - \|DE_{\downarrow}\|}\right)}{\ln(r)} = \frac{\ln\left(\frac{9.4214E-02 - 9.4175E-02}{9.4175E-02 - 9.4156E-02}\right)}{\ln\left(\frac{1.25E-4}{6.25E-5}\right)} = 1.00$$

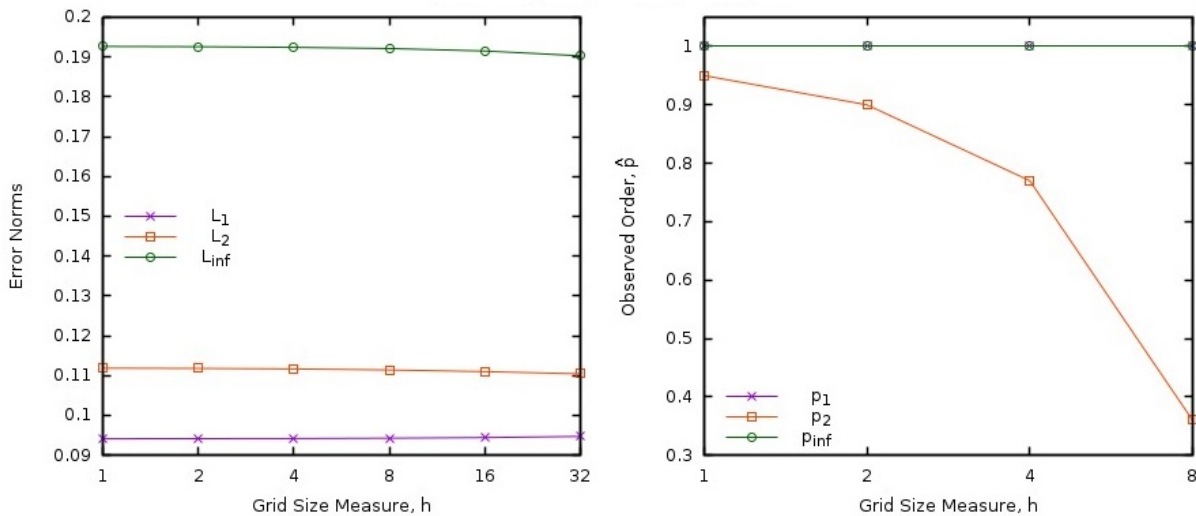


Fig. 4.4: Observed Temporal Order of Accuracy, MMS Solution to 1-D transient heat equation in MFIX

⁴ Significant digits shown in table may not result in shown values of \hat{p} because of round-off error. If the reader runs these simulations and holds all significant digits for calculation, \hat{p} values will match those shown.

Spatial order of accuracy

Likewise, spatial order of accuracy is estimated by maintaining a constant time step, 0.005s in this case. On a spatial domain of $x \in [0, 1]$, grid sizes were 3.12E-2m, 1.56E-2m, 7.81E-3m, 3.91E-3m and 1.95E-3m, resulting in a refinement factor, r , equal to 2. The observed order of accuracy, \hat{p} , converges to 2 which is equal to the formal order of the centered differencing scheme (diffusion term).

Table 4.10: L norms and the observed order for the unsteady heat equation – spatial order of accuracy⁵

h	L_1 -norm	L_2 -norm	L_∞ -norm	$\rho(L_1)$	$\rho(L_2)$	$\rho(L_\infty)$
1	5.7762E-01	6.2875E-01	8.4644E-01	2.00	2.01	1.99
2	5.7783E-01	6.2884E-01	8.4627E-01	2.00	2.03	2.01
4	5.7867E-01	6.2920E-01	8.4559E-01	2.00	2.11	2.04
8	5.8204E-01	6.3068E-01	8.4285E-01	N/A	N/A	N/A
16	5.9554E-01	6.3708E-01	8.3158E-01	N/A	N/A	N/A

An example calculation, using $h = 1, 2, 4$ and L_1 -norm is given:

$$\hat{p} = \frac{\ln\left(\frac{\|DE_{\downarrow+2}\| - \|DE_{\downarrow+1}\|}{\|DE_{\downarrow+1}\| - \|DE_{\downarrow}\|}\right)}{\ln(r)} = \frac{\ln\left(\frac{5.7867E-01 - 5.7783E-01}{5.7783E-01 - 5.7762E-01}\right)}{\ln\left(\frac{3.12E-2}{1.56E-2}\right)} = 2.00$$

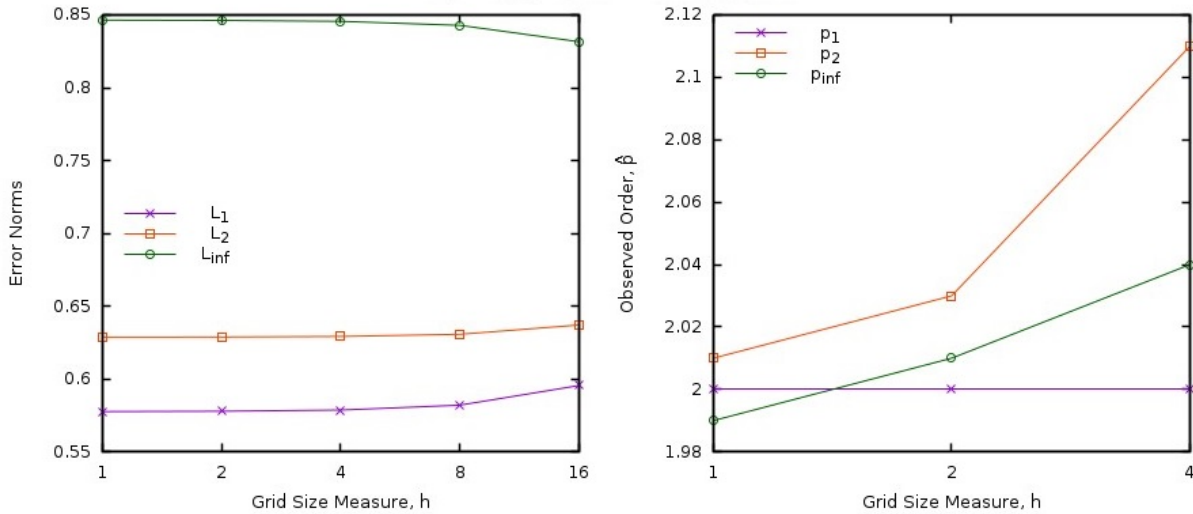


Fig. 4.5: Observed Spatial Order of Accuracy, MMS Solution to 1-D transient heat equation in MFiX

⁵ Significant digits shown in table may not result in shown values of \hat{p} because of round-off error. If the reader runs these simulations and holds all significant digits for calculation, \hat{p} values will match those shown.

Combined order analysis

Having tested temporal and spatial discretization independently, a combined order analysis is performed by choosing grid size, Δx , and time step size, Δt , according to the descriptions in section 2.4.3. Based on the observed order of accuracies, it can be concluded that the energy equation in MFiX is reduced to a Forward Time Centered Space numerical scheme. In such a case, the pertinent non-dimensional number is the Fourier number given by,

$$Fo = \alpha \frac{\Delta t}{\Delta x^2} \tag{4.43}$$

where α represents a diffusivity constant.

The stability criterion for a Forward Time Centered Space scheme is $Fo < \frac{1}{2}$. $Fo = 0.32$ was chosen in this study, while α is set to 1. The grid sizes used were 1.25E-1m, 6.25E-2m, 3.13E-2m, 1.56E-2m and 7.81E-3m. The corresponding time-step sizes are obtained as,

$$\Delta t = Fo \frac{\Delta x^2}{\alpha} \tag{4.44}$$

Note that this observation is in complete agreement with the table presented in section 2.4.3 where the analysis expectation is a problem with spatial order equal 2, and temporal order equal 1, thereby producing $r_t = (r_x)^{\frac{2}{q}} \rightarrow \Delta t = Fo (\Delta x)^{\frac{2}{q}}$.

The orders of accuracy were calculated using Equations (2-42). The tables below show that the results from combined order analysis are consistent with the individual verification tests, giving a calculated observed temporal order, $\hat{q} = 1$ and a calculated observed spatial order, $\hat{p} = 2$.

Regardless of temporal or spatial analysis, the calculated norms used in combined order analysis are identical. This idea is illustrated in the following figure and tables.

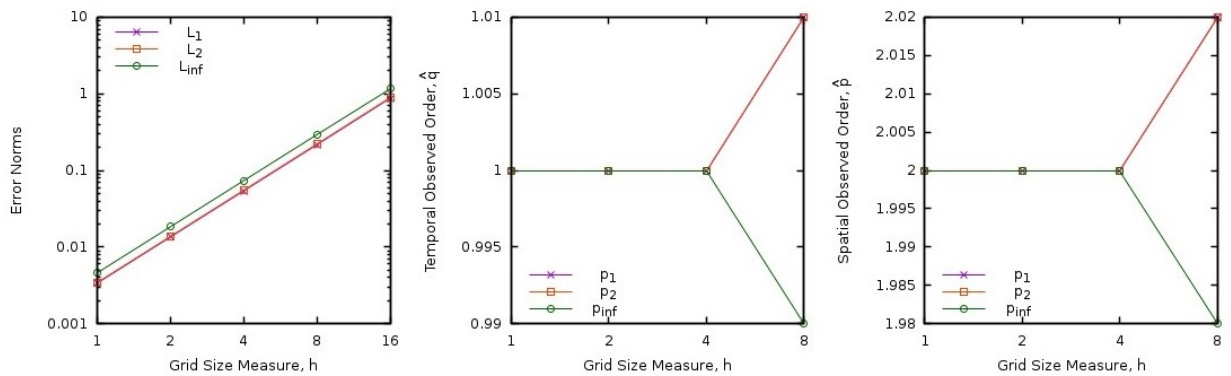


Fig. 4.6: Observed Temporal and Spatial Orders of Accuracy using Combined order analysis, MMS Solution to 1-D transient heat equation in MFiX

The key difference in calculation is the management of the denominator (related to refinement factor) for \hat{q} and \hat{p} . As explained previously, in this case, the refinement factor for time is $r_t = 4$, and the refinement factor for space is $r_x = 2$.

Table 4.11: L norms and the observed order in combined order analysis for the unsteady heat equation – temporal order of accuracy

h	L_1 -norm	L_2 -norm	L_∞ -norm	$q(L_1)$	$q(L_2)$	$q(L_\infty)$
1	3.3848E-03	3.4552E-03	4.6133E-03	1.00	1.00	1.00
2	1.3542E-02	1.3823E-02	1.8453E-02	1.00	1.00	1.00
4	5.4204E-02	5.5336E-02	7.3780E-02	1.00	1.00	1.00
8	2.1741E-01	2.2202E-01	2.9422E-01	1.01	1.01	0.99
16	8.7873E-01	8.9901E-01	1.1638E+00	N/A	N/A	N/A

Table 4.12: L norms and the observed order in combined order analysis for the unsteady heat equation – spatial order of accuracy

h	L_1 -norm	L_2 -norm	L_∞ -norm	$\rho(L_1)$	$\rho(L_2)$	$\rho(L_\infty)$
1	3.3848E-03	3.4552E-03	4.6133E-03	2.00	2.00	2.00
2	1.3542E-02	1.3823E-02	1.8453E-02	2.00	2.00	2.00
4	5.4204E-02	5.5336E-02	7.3780E-02	2.00	2.00	2.00
8	2.1741E-01	2.2202E-01	2.9422E-01	2.02	2.02	1.98
16	8.7873E-01	8.9901E-01	1.1638E+00	N/A	N/A	N/A

An example calculation, using $h = 2$ and 4 , with L_1 -norm is given:

$$\hat{q} = \frac{\ln\left(\frac{5.4204E-02}{1.3542E-02}\right)}{\ln(4)} = 1.00, \hat{p} = \frac{\ln\left(\frac{5.4204E-02}{1.3542E-02}\right)}{\ln(2)} = 2.00$$

4.5 MMS01: Single-phase, 2D, sinusoidal functions

4.5.1 Description

A sinusoidal divergence-free manufactured solution [12, 13] for the fluid pressure, P_g , and x and y velocity components, u_g and v_g , respectively, is used for the verification of steady-state, single-phase flows on a 2D grid.

$$\begin{aligned} u_g &= u_{g0} (2\pi (x + y)) \\ v_g &= v_{g0} (2\pi (x + y)) \\ P_g &= P_{g0} \cos(2\pi (x + y)) \end{aligned} \tag{4.45}$$

Fig. 4.7 shows a color contour of the pressure field and velocity streamlines for the manufactured solution using constants $P_{g0} = 100$ Pa, $u_{g0} = 5.0$ m · sec⁻¹, and $v_{g0} = 5.0$ m · sec⁻¹.

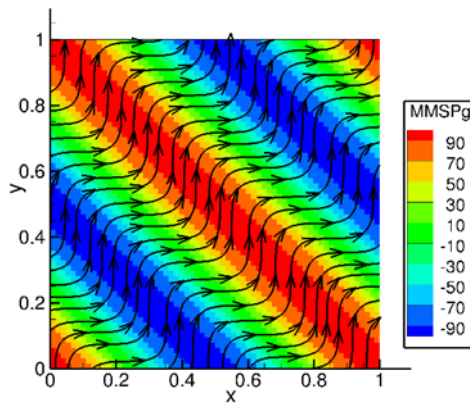


Fig. 4.7: Pressure contours and velocity streamlines for 2D, single-phase, simple sinusoidal manufactured solution on a 64x64 cell grid.

4.5.2 Setup

Table 4.13: MMS-01 Setup, Initial and Boundary Conditions.

Computational/Physical model		
2D, Steady-state, incompressible		
Single-phase (no solids)		
No gravity		
Thermal energy equation is not solved		
Turbulence equations are not solved (Laminar)		
Uniform mesh		
Superbee and Central discretization schemes		
Geometry		
Coordinate system	Cartesian	
x-length	1.0	(m)
y-length	1.0	(m)
Material [†]		
Fluid density, ρ_g	1.0	(kg·m ⁻³)
Fluid viscosity, μ_g	1.0	(Pa·s)
Initial Conditions		
Pressure (<i>gauge</i>), P_g	0.0	(Pa)
x-velocity, u_g	5.0	(m·s ⁻¹)
y-velocity, v_g	5.0	(m·s ⁻¹)
Boundary Conditions [‡]		
All boundaries	Mass inflow	

[†] Material properties selected to ensure comparable contribution from convection and diffusion terms.

[‡] The manufactured solution is imposed on all boundaries (i.e., Dirichlet specification).

4.5.3 Results

Numerical solutions were obtained using both Superbee and Central discretization schemes for 8x8, 16x16, 32x32, 64x64, and 128x128 grid meshes. The Superbee scheme order of accuracy tests show a first-order rate of convergence for pressure under the L_∞ norm as illustrated in Fig. 4.8 (a), whereas the formal order for this scheme is two. The largest errors in pressure are local to boundary cells along the West ($y=0$) and South ($x=0$) edges of the domain as shown in Fig. 4.9 (a). This is an artifact of the staggered grid implementation in MFIX where only a single ghost cell layer is present along West and South boundaries, reducing higher-order upwind schemes to first-order. This effect also occurs along the Bottom ($z=0$) edge of the domain for three-dimensional simulations. Further investigation is needed to determine to what extent the errors introduced at the boundary propagate into the domain interior.

The Central scheme results, depicted in Fig. 4.8 (b), show second order accuracy for all variables. The formal order for the Central scheme is recovered because no up-winding is performed, thereby averting solution deterioration at the boundaries. The errors in pressure near the boundaries are consistent with the scheme's formal order as can be seen from Fig. 4.9 (b).

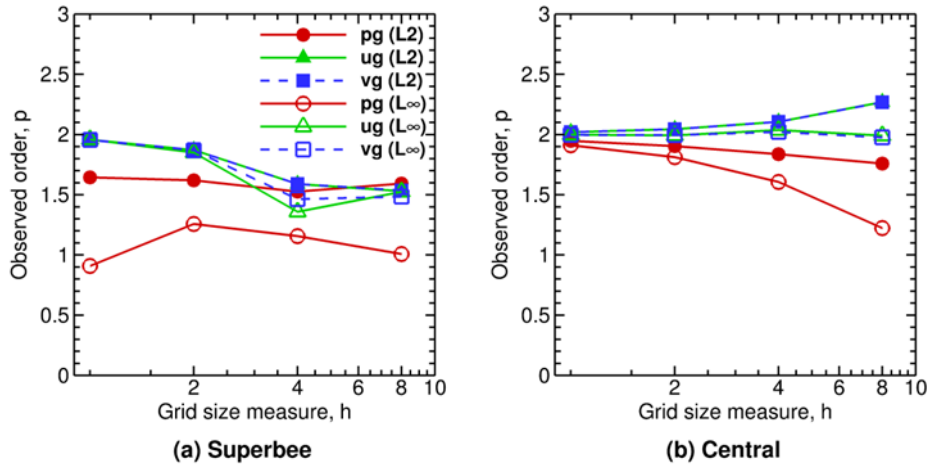


Fig. 4.8: Observed orders of accuracy for 2D, single-phase, sinusoidal manufactured solution. (a) Superbee scheme, (b) Central scheme.

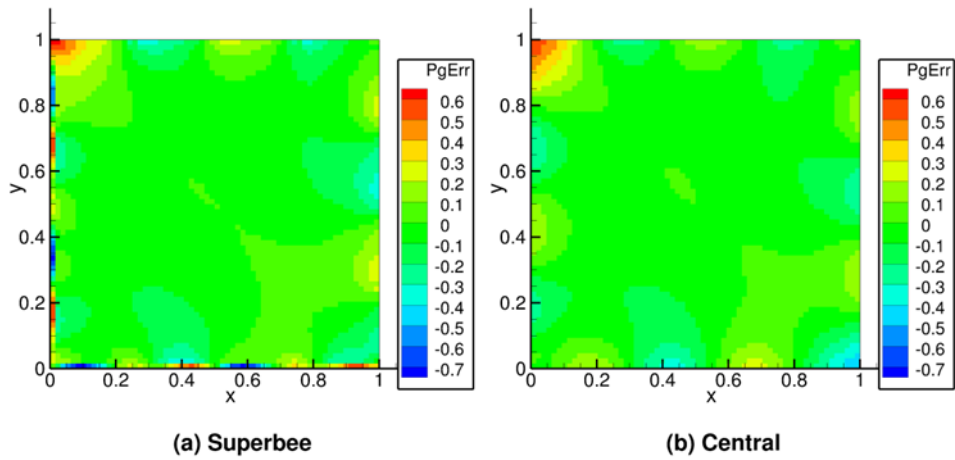


Fig. 4.9: Errors in pressure for 2D, single-phase, sinusoidal manufactured solution for grid resolution (64x64). (a) Superbee scheme, (b) Central scheme

4.5.4 Notes

During initial testing, it was discovered that the strain-tensor cross terms for the momentum equations were not calculated within steady-state sub-iterations which lead to large errors (not shown). These errors do not appear in cases with zero shear at the boundaries. Transient simulations recalculate these cross-terms at the start of each time-step making it difficult to determine the effect on the solution. The significance of this simplification (likely done to reduce computational expense) on real-world application problems is unknown and should be investigated. For MMS tests, this issue was circumvented by recalculating the cross-terms of the strain-tensor at each sub-iteration.

4.6 MMS02: Two-phase, 3D, curl-based functions with constant volume fraction

4.6.1 Description

Assuming that gas and solid volume fractions (i.e., ε_g and ε_s) remain constant, we can see from gas and solid continuity equations that both fluid and solid velocity fields are divergence-free (for constant density of fluid and solids). A manufactured solution for the fluid-phase velocity field is defined using the curl-based approach developed in [5]. For the solid-phase velocity field, a set of simple sinusoidal functions is selected (same as those shown in Eq.4.45). The manufactured solutions for scalar quantities (pressure, gas temperature, and solid temperature) can be multivariate functions of sines and cosines as defined in Eq.8.1. The selected functions for all concerned variables are shown over a 3D domain in Fig. 4.10 through Fig. 4.12.

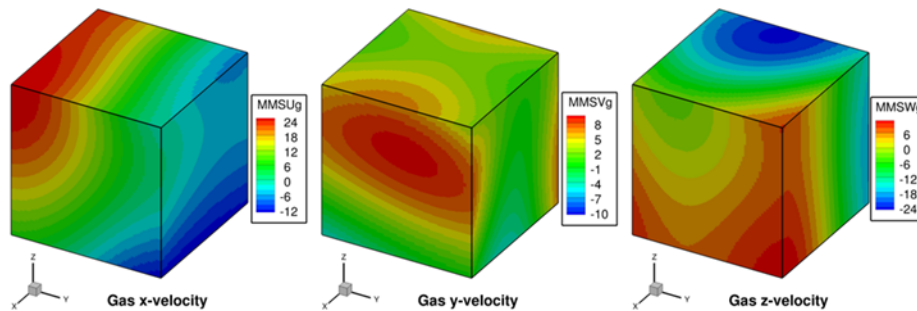


Fig. 4.10: Gas phase momentum equation manufactured solutions for 3D, steady-state, two-phase flow verification test case.

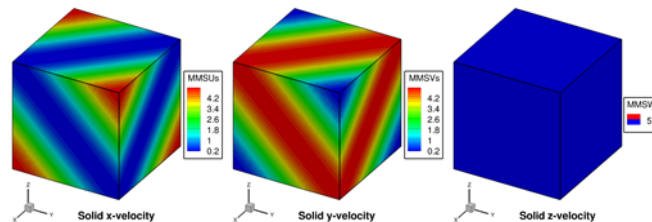


Fig. 4.11: Solids phase momentum equation manufactured solutions for 3D, steady-state, two-phase flow verification test case.

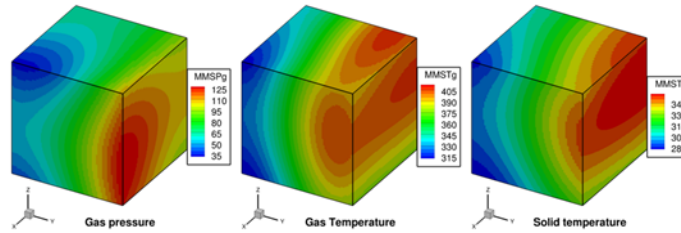


Fig. 4.12: Scalar field manufactured solutions for 3D, steady-state, two-phase flow verification test case.

4.6.2 Setup

Table 4.14: MMS-02 Setup, Initial and Boundary Conditions.

Computational/Physical model		
3D, Steady-state, incompressible		
Two-phase		
No gravity		
Drag model is turned off		
Friction model is turned off		
Thermal energy equations are solved		
Granular energy equation is not solved		
Turbulence equations are not solved (Laminar)		
Central scheme		
Geometry		
Coordinate system	Cartesian	
Domain length, L (x)	1.0	(m)
Domain height, H (y)	1.0	(m)
Domain width, W (z)	1.0	(m)
Material[†]		
Fluid density, ρ_g	1.0	($\text{kg}\cdot\text{m}^{-3}$)
Fluid viscosity, μ_g	1.0	(Pa·s)
Fluid specific heat, C_{pg}	0.05	($\text{J}\cdot\text{kg}^{-1}\cdot\text{K}^{-1}$)
Fluid thermal conductivity, k_g	1.0	($\text{J}\cdot\text{kg}^{-1}\cdot\text{K}^{-1}\cdot\text{s}^{-1}$)
Solids density, ρ_s	2.0	($\text{kg}\cdot\text{m}^{-3}$)
Solids viscosity, μ_s	2.0	(Pa·s)
Solids specific heat, C_{ps}	0.1	($\text{J}\cdot\text{kg}^{-1}\cdot\text{K}^{-1}$)
Solids thermal conductivity, k_s	2.0	($\text{J}\cdot\text{kg}^{-1}\cdot\text{K}^{-1}\cdot\text{s}^{-1}$)
Initial Conditions		
Pressure (<i>gauge</i>), P_g	0.0	(Pa)
Fluid x-velocity, u_g	10.0	($\text{m}\cdot\text{s}^{-1}$)
Fluid y-velocity, v_g	10.0	($\text{m}\cdot\text{s}^{-1}$)
Fluid z-velocity, w_g	10.0	($\text{m}\cdot\text{s}^{-1}$)
Solids x-velocity, u_s	5.0	($\text{m}\cdot\text{s}^{-1}$)
Solids y-velocity, v_s	5.0	($\text{m}\cdot\text{s}^{-1}$)
Solids z-velocity, w_s	5.0	($\text{m}\cdot\text{s}^{-1}$)
Fluid temperature, T_g	350.0	(K)
Solids temperature, T_s	300.0	(K)

continues on next page

Table 4.14 – continued from previous page

Computational/Physical model		
Gas volume fraction, ε_g	0.7	–
Boundary Conditions ‡		
All boundaries	Mass inflow	

† Material properties selected to ensure comparable contribution from convection and diffusion terms. Specified values are constant to avoid the introduction of constitutive laws.

‡ The manufactured solution is imposed on all boundaries (i.e., Dirichlet specification).

4.6.3 Results

Numerical solutions were obtained using the Central discretization scheme for 8x8, 16x16, 32x32, 64x64, and 128x128 grid meshes. The observed order approaches second order for both L_2 and L_∞ norms using the Central scheme, as shown in Fig. 4.13. This indicates that the numerical discretization terms have been implemented correctly for all derivative terms within the gas momentum equations, solid momentum equations, gas pressure correction equation, gas energy equation, and solid energy equation.

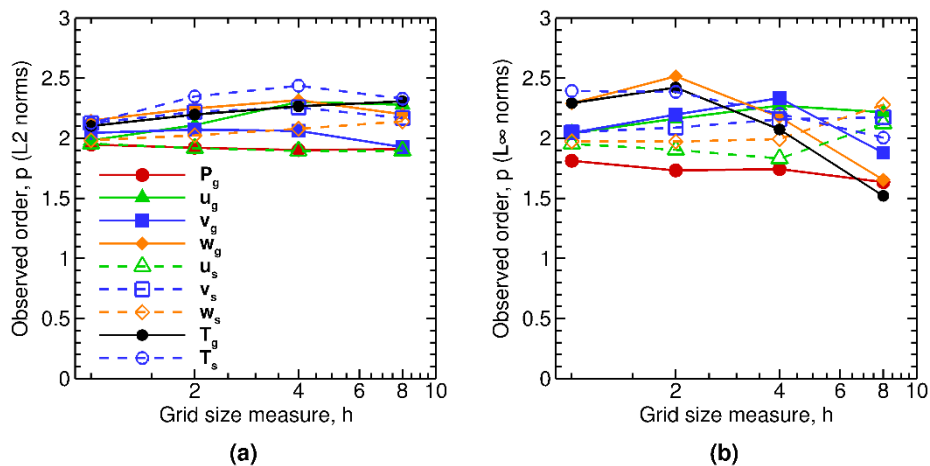


Fig. 4.13: Observed orders of accuracy for 3D, two-phase flows (constant volume fraction) using (a) L_2 norms, and (b) L_∞ norms of the discretization error.

4.7 MMS03: Two-phase, 3D, curl-based functions with variable volume fraction

4.7.1 Description

The volume fraction is selected as a function with sufficient variation in all directions while ensuring that the packed bed volume fraction ($\varepsilon_g = 0.42$) is not reached. The velocity manufactured solutions are now selected to satisfy the continuity equations (not divergence-free velocity conditions as in Section 4.6). The resulting manufactured solutions for gas volume fraction and fluid velocity variables are shown in Fig. 4.14. The mathematical form of the manufactured solutions is discussed in Section 8.

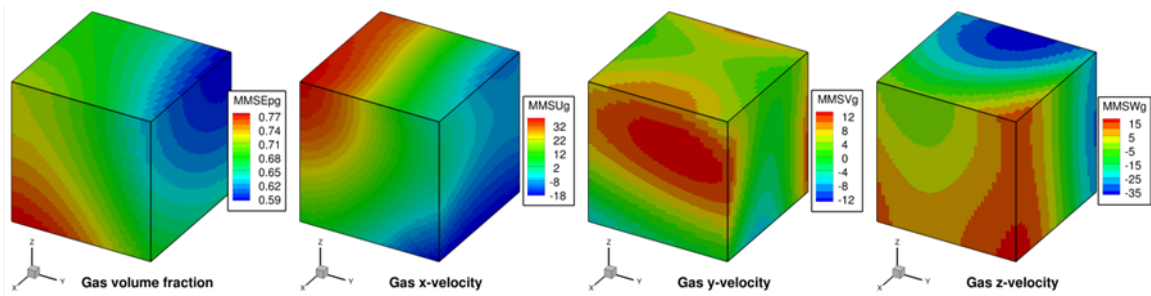


Fig. 4.14: Manufactured solutions for 3D, variable volume fraction, two-phase verification.

4.7.2 Setup

Table 4.15: MMS-03 Setup, Initial and Boundary Conditions.

Computational/Physical model		
3D, Steady-state, incompressible		
Two-phase		
No gravity		
Drag model is turned off		
Friction model is turned off		
Thermal energy equations are solved		
Granular energy equation is not solved		
Turbulence equations are not solved (Laminar)		
Non-uniform mesh		
Central scheme		
Geometry		
Coordinate system	Cartesian	
Domain length, L (x)	1.0	(m)
Domain height, H (y)	1.0	(m)
Domain width, W (z)	1.0	(m)
Material †		
Fluid density, ρ_g	1.0	($\text{kg}\cdot\text{m}^{-3}$)
Fluid viscosity, μ_g	1.0	(Pa·s)
Fluid specific heat, C_{pg}	0.05	($\text{J}\cdot\text{kg}^{-1}\cdot\text{K}^{-1}$)
Fluid thermal conductivity, k_g	1.0	($\text{J}\cdot\text{kg}^{-1}\cdot\text{K}^{-1}\cdot\text{s}^{-1}$)
Solids density, ρ_s	2.0	($\text{kg}\cdot\text{m}^{-3}$)
Solids viscosity, μ_s	2.0	(Pa·s)
Solids specific heat, C_{ps}	0.1	($\text{J}\cdot\text{kg}^{-1}\cdot\text{K}^{-1}$)
Solids thermal conductivity, k_s	2.0	($\text{J}\cdot\text{kg}^{-1}\cdot\text{K}^{-1}\cdot\text{s}^{-1}$)
Initial Conditions		
Pressure (<i>gauge</i>), P_g	0.0	(Pa)
Fluid x-velocity, u_g	10.0	($\text{m}\cdot\text{s}^{-1}$)
Fluid y-velocity, v_g	10.0	($\text{m}\cdot\text{s}^{-1}$)
Fluid z-velocity, w_g	10.0	($\text{m}\cdot\text{s}^{-1}$)
Solids x-velocity, u_s	5.0	($\text{m}\cdot\text{s}^{-1}$)
Solids y-velocity, v_s	5.0	($\text{m}\cdot\text{s}^{-1}$)

continues on next page

Table 4.15 – continued from previous page

Computational/Physical model		
Solids z-velocity, w_s	5.0	(m·s ⁻¹)
Fluid temperature, T_g	350.0	(K)
Solids temperature, T_s	300.0	(K)
Gas volume fraction, ε_g	MMS	–
Boundary Conditions ‡		
All boundaries	Mass inflow	

† Material properties selected to ensure comparable contribution from convection and diffusion terms. Specified values are constant to avoid the introduction of constitutive laws.

‡ The manufactured solution is imposed on all boundaries (i.e., Dirichlet specification).

4.7.3 Results

Numerical solutions were obtained using the Central discretization scheme for 8x8, 16x16, 32x32, 64x64, and 128x128 grid meshes. Iterative convergence was not achieved when continuity equations were solved with a variable volume fraction field. To achieve convergence, the continuity variables (ε_g , ρ_g , and P_g) were kept fixed by specifying the fields for these variables using the manufactured solution in the initial conditions routine, and discarding their iterative solution within the main solver routine. Thus, the continuity and pressure equations were not solved in this case. This restricts the ability to make any observations about the accuracy of these equations. The observed order of accuracy matches the formal order as shown in Fig. 4.15 for both velocity and energy variables.

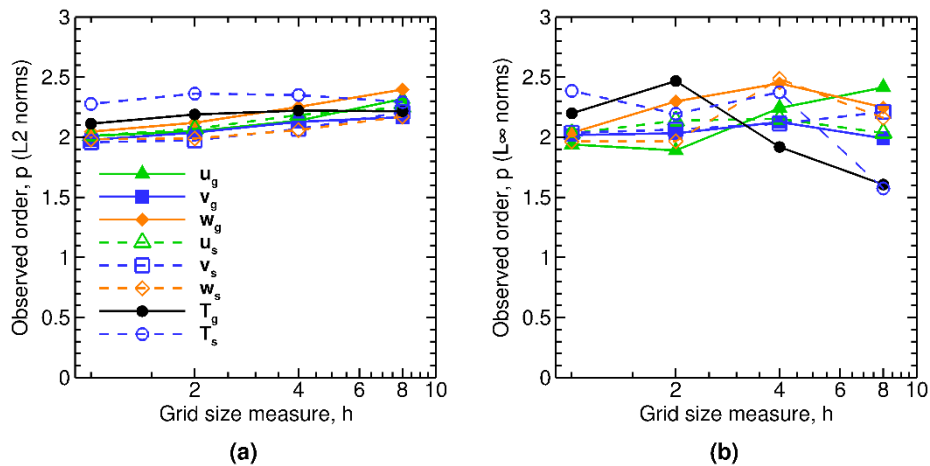


Fig. 4.15: Observed orders of accuracy for 3D, two-phase flows (variable volume fraction) using (a) L_2 norms, and (b) L_∞ norms of the discretization error.

4.8 MMS04: No-slip wall BC, single-phase, 3D, curl-based functions

4.8.1 Description

The no-slip wall boundary condition in MFiX is verified using the techniques described in [5]; the manufactured solution is selected such that it satisfies both the divergence-free constraint and the no-slip wall boundary condition. Specifically, the no-slip wall boundary condition requires that the velocity at the (stationary) no-slip wall is zero. The manufactured solution is generated using the curl-based derivation to ensure divergence-free velocity fields [5] along with the technique given in [2] to ensure that the velocity component functions approach the value of zero at each boundary tested. The manufactured solution for the velocity field used for the verification of no-slip wall is given as [6]:

$$\vec{V} = S^2 (\vec{\nabla} \times \vec{H}) + 2S (\nabla S \times \vec{H}) \quad (4.46)$$

where, \vec{V} is the velocity field vector, S is the mathematical equation of the boundary being tested, and \vec{H} is a general vector field consisting of sinusoidal expressions. The manufactured solution for pressure is selected as in Eq.8.1 since there are no constraints on pressure with this boundary condition.

4.8.2 Setup

This case is setup for single-phase flows on a domain with unit dimensions; the boundary tested is the West boundary (i.e., $x = 0$).

Table 4.16: MMS-04 Setup, Initial and Boundary Conditions.

Computational/Physical model		
3D, Steady-state, incompressible		
Single-phase (no solids)		
No gravity		
Thermal energy equations are not solved		
Turbulence equations are not solved (Laminar)		
Non-uniform mesh		
Central scheme		
Geometry		
Coordinate system	Cartesian	
Domain length, L (x)	1.0	(m)
Domain height, H (y)	1.0	(m)
Domain width, W (z)	1.0	(m)
Material [†]		
Fluid density, ρ_g	1.0	(kg·m ⁻³)
Fluid viscosity, μ_g	1.0	(Pa·s)
Initial Conditions		
Pressure (<i>gauge</i>), P_g	MMS	(Pa)
Fluid x-velocity, u_g	5.0	(m·s ⁻¹)
Fluid y-velocity, v_g	5.0	(m·s ⁻¹)
Fluid z-velocity, w_g	5.0	(m·s ⁻¹)
Boundary Conditions [‡]		
West boundary	No-slip wall	
All other boundaries	Mass inflow	

† Material properties selected to ensure comparable contribution from convection and diffusion terms.

‡ The manufactured solution is imposed on all boundaries (i.e., Dirichlet specification).

4.8.3 Results

Numerical solutions were obtained using the Central discretization scheme for 8x8, 16x16, 32x32, 64x64, and 128x128 grid meshes. Iterative convergence was not achieved for this case when pressure was solved. Hence, the pressure variable (P_g) was fixed by specifying pressure using the manufactured solution in the initial conditions routine and discarding the pressure solution in the main solver routine. The observed order of accuracy matches the formal order as shown in Fig. 4.16 for the velocity variables.

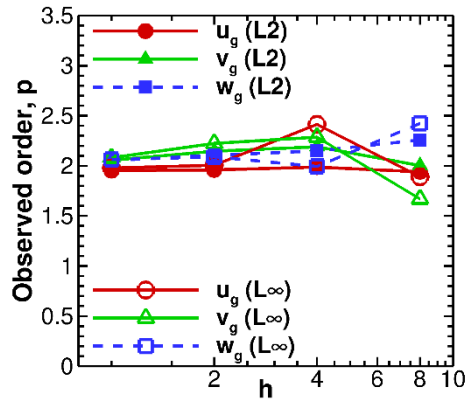


Fig. 4.16: Observed orders of accuracy for no-slip wall verification (3D, single-phase flows) using L_2 and L_∞ norms of the discretization error.

4.9 MMS05: Free-slip wall BC, single-phase, 3D, curl-based functions

4.9.1 Description

The free-slip wall boundary condition in MFIX is verified using the techniques described in [5] where the manufactured solution is selected such that it satisfies both the divergence-free constraint and the free-slip wall boundary condition. Specifically, the normal velocity component is zero at the (stationary) free-slip wall while the tangential velocity component is imposed by specifying appropriate values in the ghost cells adjacent to the wall. This results in a zero gradient condition normal to the free-slip wall for the tangential velocity components only. The manufactured solution for the velocity field used for the verification of a free-slip wall is given as [6]:

$$\vec{V} = \vec{V}_0 + S^3 (\vec{\nabla} \times \vec{H}) + 3S^2 (\nabla S \times \vec{H}) \quad (4.47)$$

where, \vec{V} is the velocity field vector, $\vec{V}_0 = \{0, v_0, w_0\}^T$ consists of non-zero scalar constants for v_0 and w_0 , S is the mathematical equation of the boundary tested (i.e., $S \equiv x = 0$), and \vec{H} is a general vector field consisting of sinusoidal expressions. The pressure manufactured solution is selected as in Eq.8.1 since there are no constraints on pressure with this boundary condition.

4.9.2 Setup

This case is setup for single-phase flows on a domain with unit dimensions; the boundary tested is the West boundary (i.e., $x = 0$).

Table 4.17: MMS-05 Setup, Initial and Boundary Conditions.

Computational/Physical model		
3D, Steady-state, incompressible		
Single-phase (no solids)		
No gravity		
Thermal energy equations are not solved		
Turbulence equations are not solved (Laminar)		
Non-uniform mesh		
Central scheme		
Geometry		
Coordinate system	Cartesian	
Domain length, L (x)	1.0	(m)
Domain height, H (y)	1.0	(m)
Domain width, W (z)	1.0	(m)
Material [†]		
Fluid density, ρ_g	1.0	(kg·m ⁻³)
Fluid viscosity, μ_g	1.0	(Pa·s)
Initial Conditions		
Pressure (<i>gauge</i>), P_g	MMS	(Pa)
Fluid x-velocity, u_g	5.0	(m·s ⁻¹)
Fluid y-velocity, v_g	5.0	(m·s ⁻¹)
Fluid z-velocity, w_g	5.0	(m·s ⁻¹)
Boundary Conditions [‡]		
West boundary	Free-slip wall	
All other boundaries	Mass inflow	

[†] Material properties selected to ensure comparable contribution from convection and diffusion terms.

[‡] The manufactured solution is imposed on all boundaries (i.e., Dirichlet specification).

4.9.3 Results

Numerical solutions were obtained using the Central discretization scheme for 8x8, 16x16, 32x32, 64x64, and 128x128 grid meshes. Iterative convergence could not be achieved for this case when pressure was solved. Hence, the pressure variable (P_g) was fixed by specifying pressure using the manufactured solution in the initial conditions routine and discarding the pressure solution in the main solver routine. The observed order of accuracy matches the formal order as shown in Fig. 4.17 for the velocity variables.

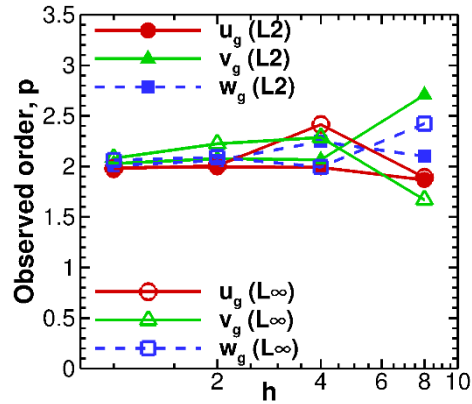


Fig. 4.17: Observed orders of accuracy for free-slip wall verification (3D, single-phase flows) using L_2 and L_∞ norms of the discretization error.

4.10 MMS06: Pressure outflow BC, single-phase, 3D, curl-based functions

4.10.1 Description

The pressure outflow boundary condition in MFIX is verified using the techniques described in [5] where the manufactured solution is selected such that it satisfies both the divergence-free constraint and the pressure outflow condition. Specifically, this boundary condition requires that the pressure and all velocity components at the outflow have zero gradients normal to the wall at the boundary. For verification of the pressure outflow condition, the manufactured solution for the velocity field is given by Eq.4.48 while that for pressure is given by Eq.4.49 [6].

$$\vec{V} = \vec{V}_0 + S^3 (\vec{\nabla} \times \vec{H}) + 3S^2 (\nabla S \times \vec{H}) \quad (4.48)$$

$$P = P_0 + S^2 P_1 \quad (4.49)$$

Here, \vec{V} is the velocity field vector, S is the mathematical equation of the boundary tested (here, $S \equiv y = 1$), P_0 is a non-zero scalar constant, P_1 represents the sinusoidal terms of the general manufactured solution, and \vec{H} is a general vector field consisting of sinusoidal expressions.

4.10.2 Setup

This case is setup for single-phase flows on a domain with unit dimensions; the boundary tested is the North boundary (i.e., $y = 1$).

Table 4.18: MMS-06 Setup, Initial and Boundary Conditions.

Computational/Physical model		
3D, Steady-state, incompressible		
Single-phase (no solids)		
No gravity		
Turbulence equations are not solved (Laminar)		
Non-uniform mesh		
Central scheme		
Geometry		
Coordinate system	Cartesian	
Domain length, L (x)	1.0	(m)
Domain height, H (y)	1.0	(m)
Domain width, W (z)	1.0	(m)
Material [†]		
Fluid density, ρ_g	1.0	(kg·m ⁻³)
Fluid viscosity, μ_g	1.0	(Pa·s)
Initial Conditions		
Pressure (<i>gauge</i>), P_g	0.0	(Pa)
Fluid x-velocity, u_g	5.0	(m·s ⁻¹)
Fluid y-velocity, v_g	5.0	(m·s ⁻¹)
Fluid z-velocity, w_g	5.0	(m·s ⁻¹)
Boundary Conditions [‡]		
North boundary	Pressure outflow	
All other boundaries	Mass inflow (MMS)	

[†] Material properties selected to ensure comparable contribution from convection and diffusion terms.

[‡] The manufactured solution is imposed on all boundaries (i.e., Dirichlet specification).

4.10.3 Results

Numerical solutions were obtained using the Central discretization scheme for 8x8, 16x16, 32x32, 64x64, and 128x128 grid meshes. The observed order of accuracy matches the formal order as shown in Figure 2-15 for both the velocity variables and the pressure. Unlike the test cases verifying the no-slip and free-slip boundary conditions, no convergence issues were encountered since the problem has a physically-realistic outflow boundary.

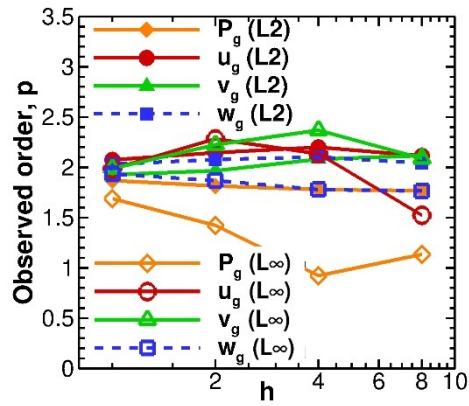


Fig. 4.18: Observed orders of accuracy for pressure outflow verification using L_2 and L_∞ norms of the discretization error.

FLUID MODEL CODE VERIFICATION TEST CASES

The test cases presented in this chapter for the MFiX fluid solver are summarized in [Table 4.1](#). Test cases were selected based on the criteria for verification test selection outlined in [Section 3](#). All cases are executed in serial mode unless explicitly noted.

Table 5.1: Summary of MFiX-FLD tests by feature.

	01	02	03	04	05	06	07	08	09
Frequency [†]	C	C	C	C	M	M	M	M	M
Reference Dataset [‡]	A	A	P	A	A	A	P	P	P
Dimension	2D	1D	2D						
Momentum	✓		✓	✓	✓	✓	✓	✓	✓
Thermal Energy		✓							
Species Mass						✓			
Turbulence							✓	✓	✓
FOUP				✓					
FOUP-DWF									
Superbee	✓	✓	✓	✓	✓		✓	✓	✓
SMART				✓		✓			
ULTRA-QUICK									
QUICKEST				✓					
MUSCL				✓					
van Leer				✓					
Minmod				✓					
Central				✓					
Distributed Memory			✓						
Shared Memory									

[†] C-Incorporated into the continuous integration server; M-Monthly; Q-Quarterly; X-Manual; D-Disabled

[‡] A-Analytical solution; P-Published benchmark data; R-Regression data from previous code versions

5.1 FLD01: Steady, 2D Poiseuille flow

5.1.1 Description

Plane Poiseuille flow is defined as a steady, laminar flow of a viscous fluid between two horizontal parallel plates separated by a distance, H . Flow is induced by a pressure gradient across the length of the plates, L , and is characterized by a 2D parabolic velocity profile symmetric about the horizontal mid-plane as illustrated in Fig. 5.1.

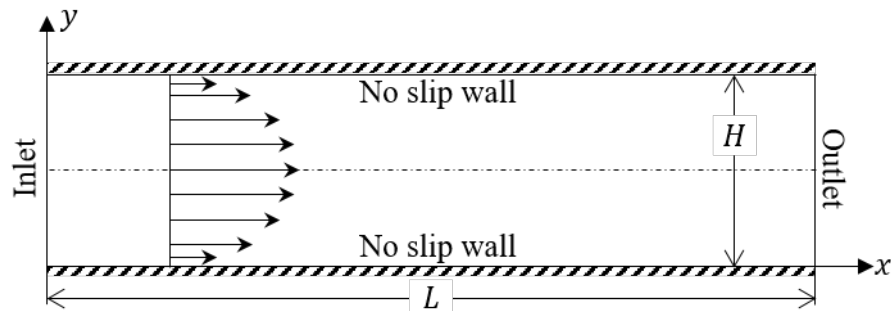


Fig. 5.1: Plane Poiseuille flow between two flat plates of length L , separated by a distance H .

In this problem, the Navier-Stokes equations reduce to a second order, linear, ordinary differential equation (ODE),

$$\mu_g \frac{d^2 u_g}{dy^2} = \frac{dP_g}{dx}, \quad (5.1)$$

where μ_g and P_g are correspondingly the fluid viscosity and pressure, and u_g and v_g are respectively the x and y velocity components. Furthermore, it is assumed that gravitational forces are negligible, the pressure gradient is constant, i.e., $dP_g/dx = C$, and all velocity components are zero at the channel walls. The resulting analytical solution to Eq.5.1 is given as

$$u_g(y) = -\frac{dP_g}{dx} \frac{1}{2\mu_g} y(H - y). \quad (5.2)$$

5.1.2 Setup

```
#####
#
# Author: Aniruddha Choudhary                               Date: Jan 2015 #
# Horizontal channel (rectangular plane Poiseuille flow)    #
#                                                            #
# A pressure gradient is imposed over x-axis cyclic boundaries. The #
# north and south walls are no-slip.                         #
#                                                            #
#####

RUN_NAME = 'FLD01'
DESCRIPTION = 'Steady, 2D Poiseuille Flow'

#
# RUN CONTROL SECTION

UNITS = 'SI'
```

(continues on next page)

(continued from previous page)

```
RUN_TYPE = 'NEW'

ENERGY_EQ = .F.
SPECIES_EQ(0) = .F.

GRAVITY = 0.0

CALL_USR = .T.

#
# NUMERICAL SECTION

MAX_NIT = 200000
TOL_RESID = 1.0E-10

LEQ_PC(1:9) = 9*'NONE'

DISCRETIZE(1:9) = 9*2
NORM_G = 0.0

#
# GEOMETRY SECTION

COORDINATES = 'CARTESIAN'

ZLENGTH = 1.00      NO_K = .T.
XLENGTH = 0.20      IMAX = 8
YLENGTH = 0.01      JMAX = 8

#
# GAS-PHASE SECTION

RO_g0 = 1.0      ! (kg/m3)
MU_g0 = 1.0d-3  ! (Pa.s)

#
# SOLIDS-PHASE SECTION

MMAX = 0

#
# INITIAL CONDITIONS SECTION

IC_X_w(1) = 0.00      ! (m)
IC_X_e(1) = 0.20      ! (m)
IC_Y_s(1) = 0.00      ! (m)
IC_Y_n(1) = 0.01      ! (m)

IC_EP_g(1) = 1.0

IC_P_g(1) = 0.0      ! (Pa)

IC_U_g(1) = 10.0     ! (m/sec)
IC_V_g(1) = 0.0     ! (m/sec)

#
```

(continues on next page)

(continued from previous page)

```

# BOUNDARY CONDITIONS SECTION

! Inlet and outlet: Periodic BC
!-----//

CYCLIC_X_PD = .T.
DELP_X =      240.00    ! (Pa)

! Top and bottom walls: No-slip
!-----//
! Bottom wall
BC_X_w(3) =    0.00    ! (m)
BC_X_e(3) =    0.20    ! (m)
BC_Y_s(3) =    0.00    ! (m)
BC_Y_n(3) =    0.00    ! (m)

BC_TYPE(3) = 'NSW'

! Top wall
BC_X_w(4) =    0.00    ! (m)
BC_X_e(4) =    0.20    ! (m)
BC_Y_s(4) =    0.01    ! (m)
BC_Y_n(4) =    0.01    ! (m)

BC_TYPE(4) = 'NSW'

#-----
# OUTPUT CONTROL SECTION

RES_DT =      1.0      ! (sec)
SPX_DT(1:9) = 9*1.0    ! (sec)

FULL_LOG = .T.

RESID_STRING = 'P0', 'U0', 'V0'

#-----
# DMP SETUP

! NODESI = 1  NODESJ = 1  NODESK = 1

```

5.1.3 Results

The analytical and numerical solutions for x-velocity, u_g , are shown in Fig. 5.2. Only a subset of the numerical solution data points are plotted causing the appearance of a slight shift in presented data points. The observed error demonstrates a second-order rate of convergence with respect to grid size in the y-axial direction. This is attributed to the second-order discretization of the viscous stress term as convection/diffusion terms do not contribute to the solution.

The fluid pressure, P_g , varies linearly along the length of the plates as shown in Fig. 5.3. The largest observed absolute error is bounded above by 10^{-12} and occurs for the finest mesh. This error is attributed to the convergence criteria of the linear equation system.

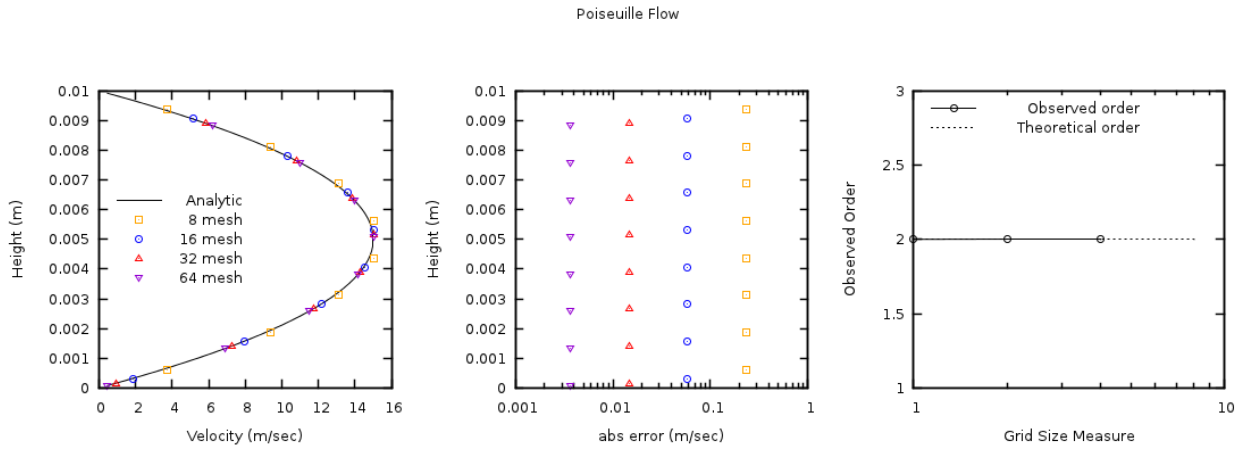


Fig. 5.2: Steady, 2D channel flow x-velocity profile (left), absolute error in x-velocity solution (center), and observed order of accuracy (right) using four grid levels (JMAX = 8, 16, 32, 64).

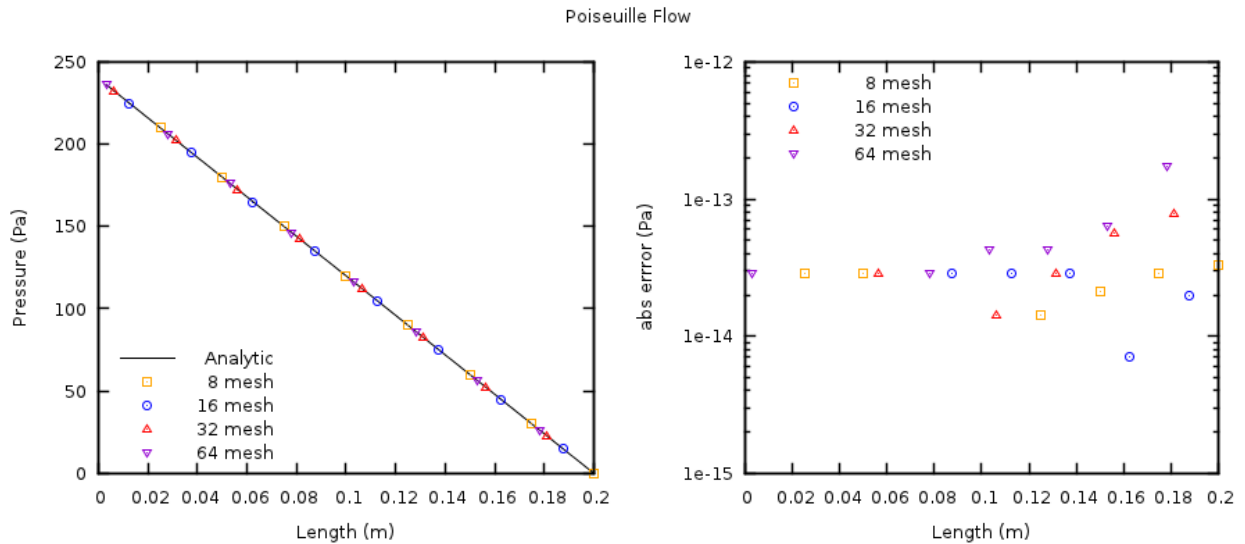


Fig. 5.3: Steady, 2D channel flow pressure profile (left) and absolute error in pressure solution (right) using four grid levels (IMAX = 8, 16, 32, 64).

5.2 FLD02: Steady, 1D heat conduction

5.2.1 Description

Steady-state, one-dimensional heat conduction occurs across a rectangular plane-shaped slab of length L with constant material properties. As shown in Fig. 5.4, two opposing slab boundaries are maintained at constant temperatures. All other faces are perfectly insulated such that the heat flux along these boundaries is zero. Without heat generation, heat transfer through the $x = 0$ face must equal that through the $x = L$ face.

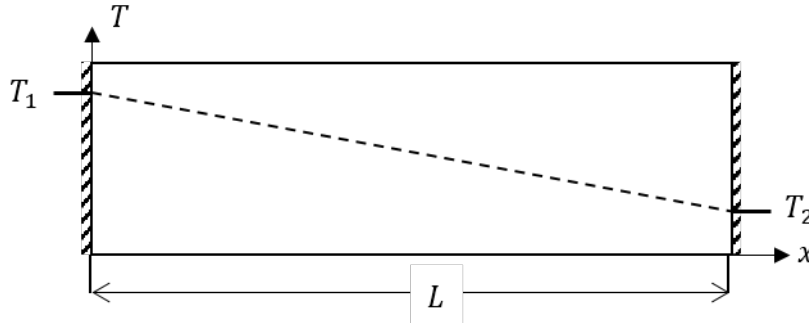


Fig. 5.4: Plane slab with constant material properties and no internal heat generation is shown with constant temperatures specified on opposing faces. The slab is assumed to be perfectly insulated along all other faces.

For constant thermal conductivity, the energy equation reduces to a second order ODE with Dirichlet boundary conditions as given by :eq:fld02eq1. The analytical solution for temperature distribution within the slab follows a line as given by :eq:fld02eq2.

$$\frac{d}{dx} \left(\lambda_g \frac{dT}{dx} \right) = 0; T(x = 0) = T_1; T(x = L) = T_2 \quad (5.3)$$

$$T(x) = T_1 + \frac{(T_2 - T_1)}{L} x \quad (5.4)$$

5.2.2 Setup

```
#####
#
# Author: Aniruddha Choudhary                               Date: May 2015 #
# Steady-state 1D heat conduction through a plane slab.     #
#                                                            #
# Default walls are used for the north/south boundaries as they are #
# adiabatic. The temperature is specified for the east/west walls. #
#####

RUN_NAME = 'FLD02'
DESCRIPTION = 'Steady, 1D heat conduction'

#
# RUN CONTROL SECTION

UNITS = 'SI'
RUN_TYPE = 'NEW'
```

(continues on next page)

(continued from previous page)

```

MOMENTUM_X_EQ = .F.
MOMENTUM_Y_EQ = .F.

ENERGY_EQ = .T.
SPECIES_EQ(0) = .F.

GRAVITY = 0.0

CALL_USR = .T.

#
# NUMERICAL SECTION

Max_nit = 200000
TOL_RESID_T = 1.0E-16

LEQ_PC(6) = 'NONE'

#
# GEOMETRY SECTION

COORDINATES = 'CARTESIAN'

ZLENGTH = 1.00      NO_K = .T.
XLENGTH = 1.00      IMAX = 8
YLENGTH = 1.00      JMAX = 8

#
# GAS-PHASE SECTION

RO_g0 = 1.0      ! (kg/m3)
MU_g0 = 1.0      ! (Pa.s)
C_Pg0 = 1.0      ! (J/kg.K)
K_g0 = 1.0      ! (W/m.K)

#
# SOLIDS-PHASE SECTION

MMAX = 0

#
# INITIAL CONDITIONS SECTION

IC_X_w(1) = 0.0      ! (m)
IC_X_e(1) = 1.0      ! (m)
IC_Y_s(1) = 0.0      ! (m)
IC_Y_n(1) = 1.0      ! (m)

IC_EP_g(1) = 1.0

IC_P_g(1) = 0.0      ! (Pa)
IC_T_g(1) = 350.0    ! (K)

IC_U_g(1) = 0.0      ! (m/sec)
IC_V_g(1) = 0.0      ! (m/sec)

```

(continues on next page)

```

#-----
# BOUNDARY CONDITIONS SECTION

! Specified temperatures at west and east walls
!-----//
BC_X_w(1:2) = 0.0 1.0 ! (m)
BC_X_e(1:2) = 0.0 1.0 ! (m)
BC_Y_s(1:2) = 0.0 0.0 ! (m)
BC_Y_n(1:2) = 1.0 1.0 ! (m)

BC_TYPE(1:2) = 'NSW' 'NSW'

BC_Tw_g(1:2) = 400.0 300.0 ! (K)

#-----
# OUTPUT CONTROL SECTION

RES_DT = 1.0 ! (sec)
SPX_DT(1:9) = 9*1.0 ! (sec)

FULL_LOG = .T.

RESID_STRING = 'T0'

#-----
# DMP SETUP

! NODESI = 1 NODESJ = 1 NODESK = 1

```

5.2.3 Results

The analytical and numerical solutions for temperature, T_g , are shown in Fig. 5.5. Only a subset of the numerical solution data points are plotted causing the appearance of a slight shift in presented data points. The largest observed absolute error is bounded above by 10^{-12} and occurs for the finest mesh. This error is attributed to convergence criteria of the linear equation solver.

5.3 FLD03: Steady, lid-driven square cavity

5.3.1 Description

Lid-driven flow in a 2D square cavity in the absence of gravity is illustrated in Fig. 5.6. The problem definition follows the work of Ghia et al. [10] where the domain is bounded on three sides with stationary walls while one wall, the lid, is prescribed a constant velocity. The cavity is completely filled with a fluid of selected viscosity and the flow is assumed to be incompressible and laminar.

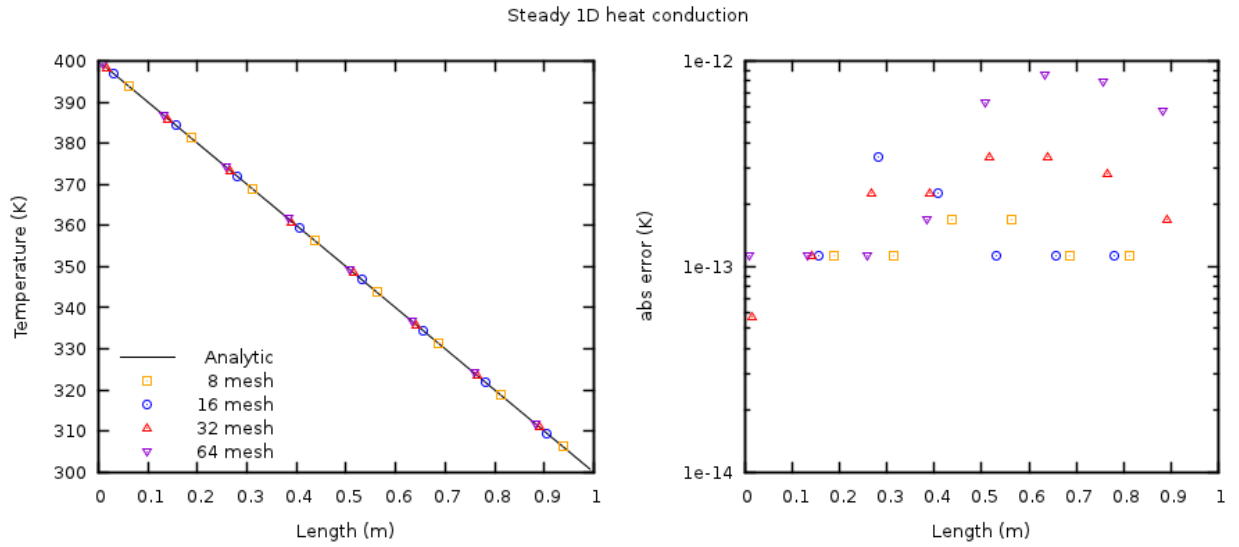


Fig. 5.5: Steady, 1D heat-conduction. (Left) numerical solution vs analytical solution, and (right) absolute error between the analytical and numerical solutions.

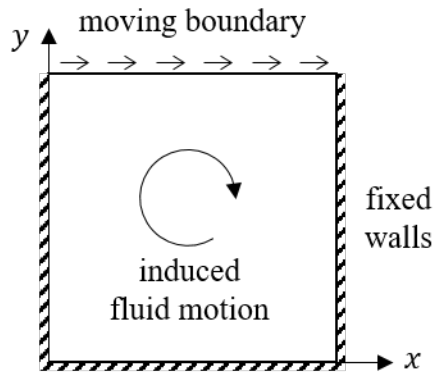


Fig. 5.6: Schematic of the lid-driven square cavity.

5.3.2 Setup

```
#####
#
# Author: M. Syamlal                               Date: Dec 1999 #
# Revised: A. Choudhary and J. Musser              Date: Jun 2015 #
#
# A top wall driven cavity with only fluid phase present in the #
# absence of gravitational forces.                  #
#
# REF: Ghia U., Ghia K.N., and Shin C.T., High-Re Solutions for Incom- #
#       pressible Flow Using the Navier-Stokes Equations and a Multi- #
#       grid Method, Journal of Computational Physics, Volume 48, pages #
#       387-411, 1982. doi: 10.1016/0021-9991(82)90058-4 #
#
#####

RUN_NAME = 'FLD03'
DESCRIPTION = 'Lid-driven cavity'

#-----
# RUN CONTROL SECTION

UNITS = 'SI'
RUN_TYPE = 'NEW'

TSTOP = 1.0d8

DT =      1.0e-2
DT_FAC = 1.0

ENERGY_EQ =      .F.
SPECIES_EQ(0) = .F.

GRAVITY = 0.0

CALL_USR = .T.

#-----
# NUMERICAL SECTION

LEQ_PC(1:9) = 9*'DIAG'

DISCRETIZE(1:9) = 9*2
DETECT_STALL = .F.

NORM_G = 1.0

#-----
# GEOMETRY SECTION

COORDINATES = 'CARTESIAN'

ZLENGTH = 1.0   NO_K = .T.
XLENGTH = 1.0   IMAX = 128
YLENGTH = 1.0   JMAX = 128
```

(continues on next page)

(continued from previous page)

```

#
# GAS-PHASE SECTION

RO_G0 = 1.0      ! (kg/m3)
MU_G0 = 0.01    ! (Pa.sec)

#
# SOLIDS-PHASE SECTION

MMAX = 0

#
# INITIAL CONDITIONS SECTION

IC_X_w(1) = 0.00 ! (m)
IC_X_e(1) = 1.00 ! (m)
IC_Y_s(1) = 0.00 ! (m)
IC_Y_n(1) = 1.00 ! (m)

IC_EP_g(1) = 1.00

IC_U_g(1) = -1.0e-2! (m/sec)
IC_V_g(1) = 0.00 ! (m/sec)

#
# BOUNDARY CONDITIONS SECTION

! West, East and South are default No-Slip Walls (NSW)

! North: Lid with a constant velocity of 1.0 m/s along +x using a
! partial slip wall (PSW) implemented as  $dv/dn + Hw(V-Vw) = 0.0$ 
! where  $Vw$  is the wall speed and  $Hw$  is undefined (Inf).
!-----//
BC_X_w(1) = 0.00 ! (m)
BC_X_e(1) = 1.00 ! (m)
BC_Y_s(1) = 1.00 ! (m)
BC_Y_n(1) = 1.00 ! (m)

BC_TYPE(1) = 'PSW'

BC_Uw_g(1) = 1.00 ! (m/sec)
BC_Vw_g(1) = 0.00 ! (m/sec)

#
# OUTPUT CONTROL SECTION

RES_DT = 5.0d3 ! (sec)
SPX_DT(1:9) = 9*5.0d3 ! (sec)

FULL_LOG = .F.

RESID_STRING = 'P0' 'U0' 'V0'

#
# DMP SETUP

```

(continues on next page)

```
! NODESI = 1 NODESJ = 1 NODESK = 1
```

5.3.3 Results

Numerical solutions were obtained on a 128x128 grid mesh for Reynolds numbers of 100 and 400 by specifying fluid viscosities of 1/100 and 1/400 Pa·s, respectively. A time step of 0.01 second was used and the simulations considered converged when the average L_2 Norms for the x-axis and y-axis velocity components, u_g and v_g , were less than 10^{-8} .

The horizontal velocity at the vertical centerline ($x = 0.5$) and the vertical velocity at the horizontal centerline ($y = 0.5$) are compared with those of Ghia et al. [10] in Fig. 5.7 and Fig. 5.8.

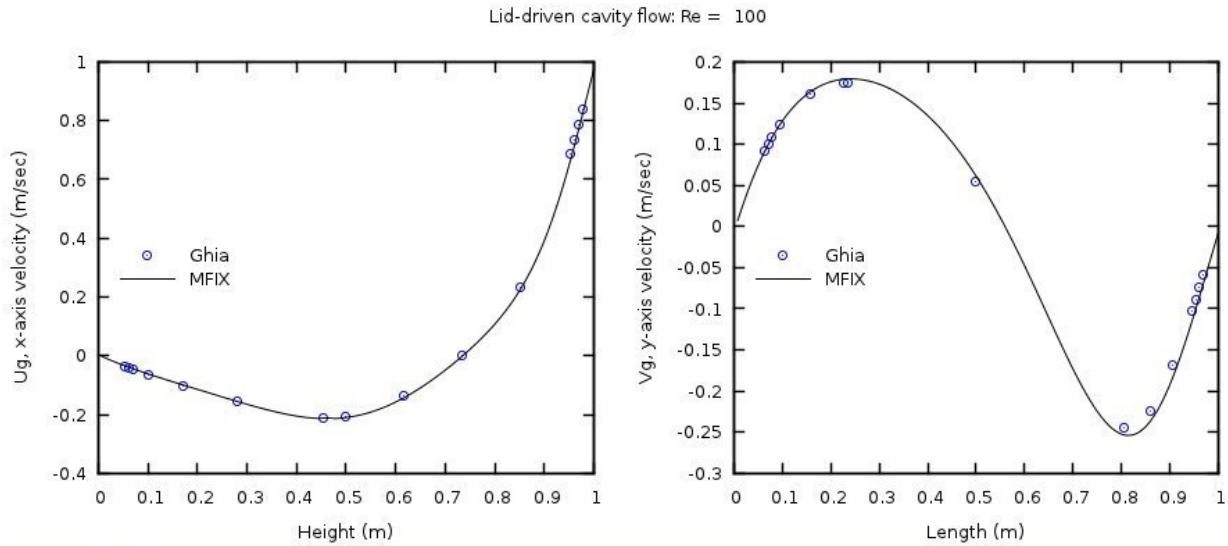


Fig. 5.7: Comparison of velocities at the vertical ($x=0.5$) and horizontal centerlines ($y=0.5$) of the cavity with Ghia et al. [10] for Reynolds number of 100 (128x128 grid).

Similarly, numerical solutions were obtained on a 128x128 grid mesh for Reynolds numbers of 1000 and 3200 by specifying fluid viscosities of 1/1000 and 1/3200 Pa·s, respectively. The horizontal velocity at the vertical centerline ($x = 0.5$) and the vertical velocity at the horizontal centerline ($y = 0.5$) are compared with those of Ghia et al. [10] in Fig. 5.9 and Fig. 5.10. These cases are not included in the continuous integration server test suite.

5.4 FLD04: Gresho vortex problem

5.4.1 Description

The Gresho vortex problem [11] involves a stationary rotating vortex for which the centrifugal forces are exactly balanced by pressure gradients. The angular velocity and pressure distribution varies with radius as given by Eq.5.5;:eq:fld04eq2 [16] while the radial velocity is zero everywhere and the density is one everywhere.

$$u_\phi(r) = \begin{cases} 5r, & 0 \leq r < 0.2 \\ 2 - 5r, & 0.2 \leq r < 0.4; \\ 0, & 0.4 \leq r \end{cases} \quad (5.5)$$

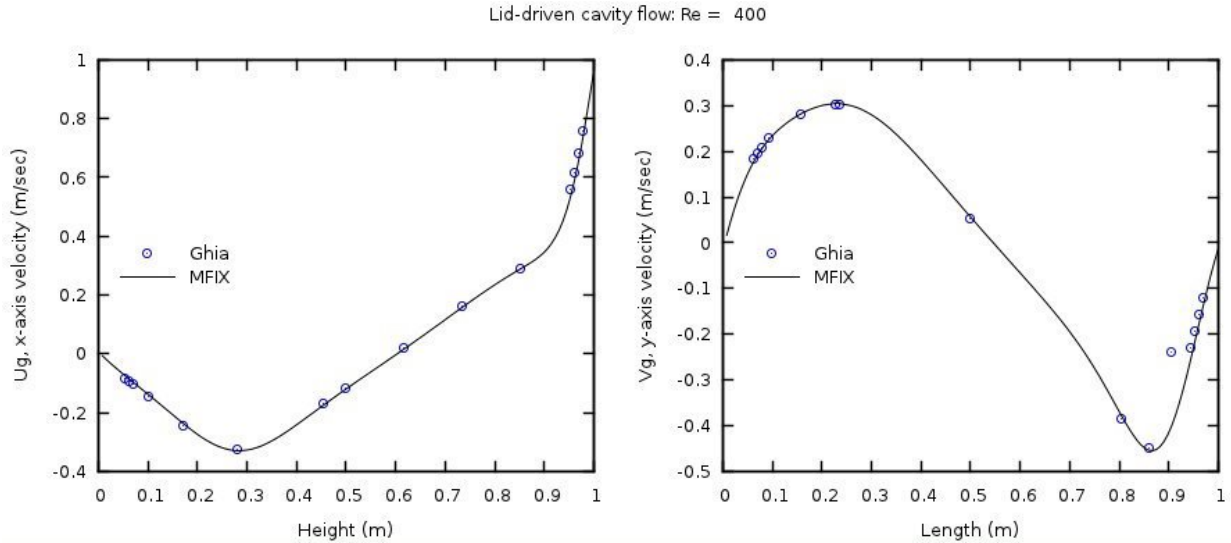


Fig. 5.8: Comparison of velocities at the vertical ($x=0.5$) and horizontal centerlines ($y=0.5$) of the cavity with Ghia et al. [10] for Reynolds number of 400 (128x128 grid).

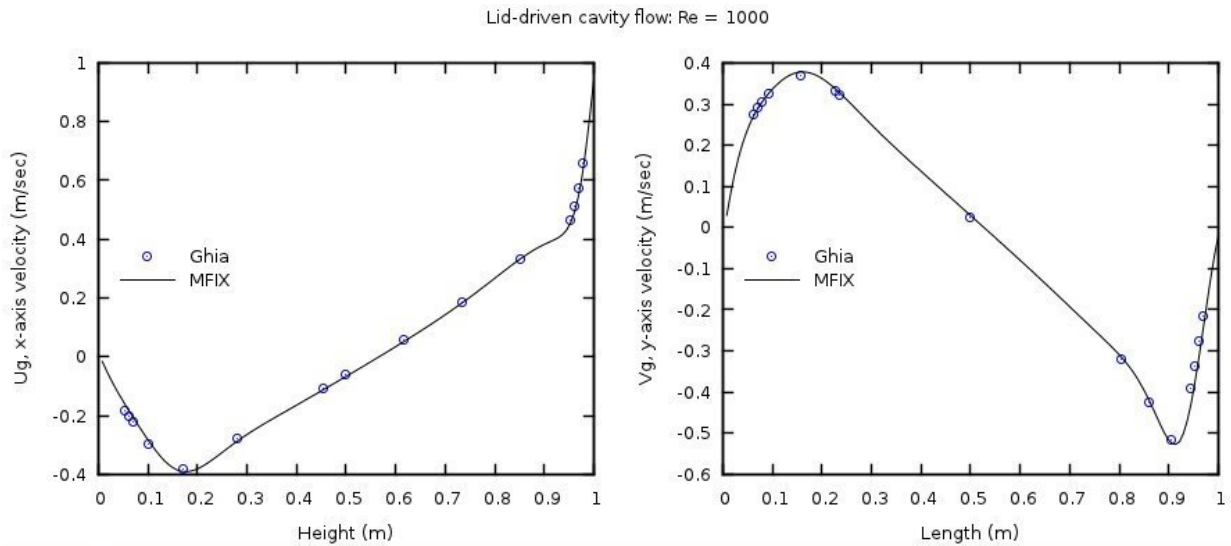


Fig. 5.9: Comparison of velocities at the vertical ($x=0.5$) and horizontal centerlines ($y=0.5$) of the cavity with Ghia et al. [10] for Reynolds number of 1000 (128x128 grid).

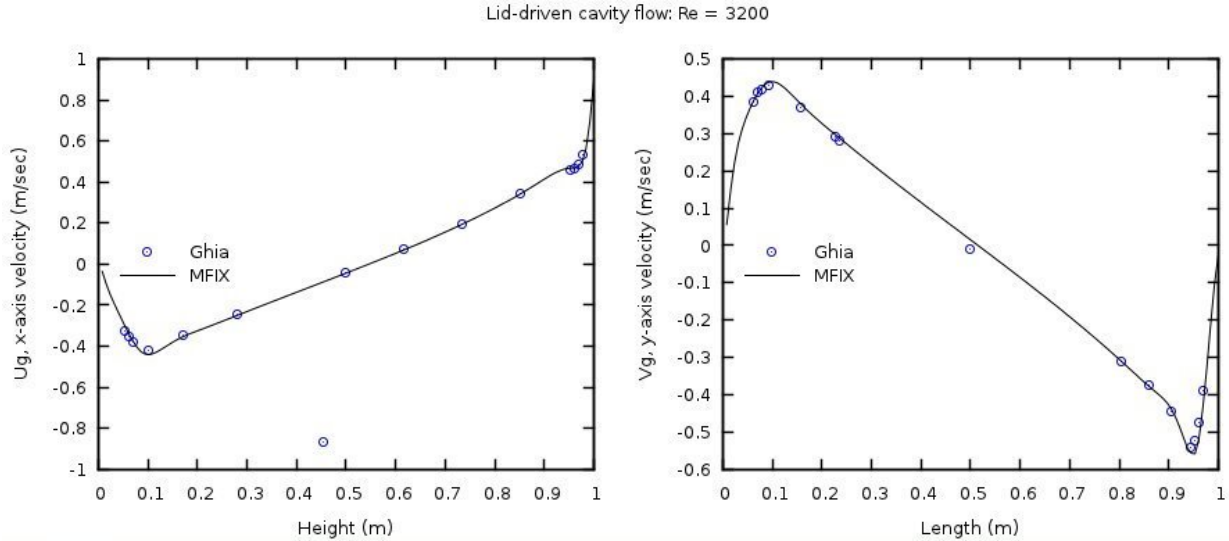


Fig. 5.10: Comparison of velocities at the vertical ($x=0.5$) and horizontal centerlines ($y=0.5$) of the cavity with Ghia et al. [10] for Reynolds number of 3200 (128x128 grid).

$$p(r) = \begin{cases} 5 + 12.5r^2, & 0 \leq r < 0.2 \\ 9 - 4\ln 0.2 + 12.5r^2 - 20r + 4\ln r, & 0.2 \leq r < 0.4 \\ 3 + 4\ln 2, & 0.4 \leq r \end{cases} \quad (5.6)$$

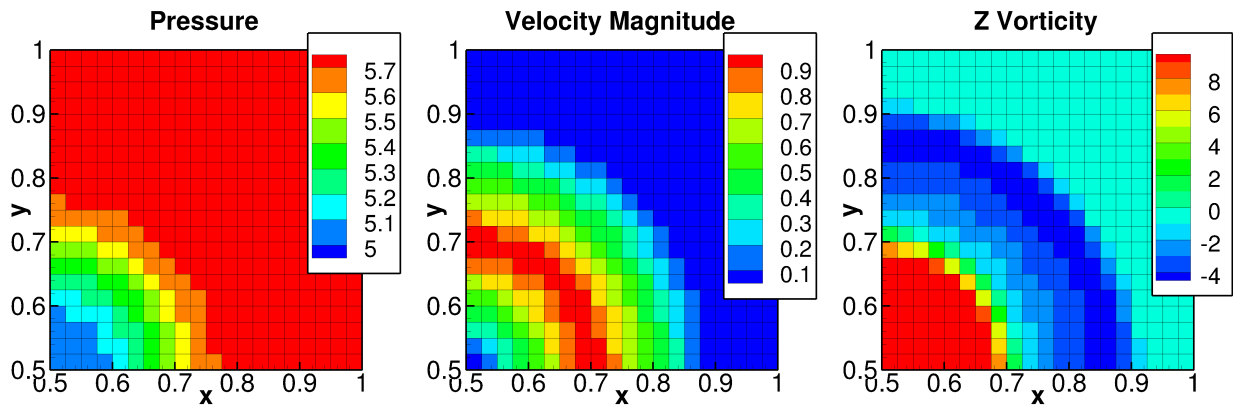


Fig. 5.11: Exact solution for the Gresho vortex problem (shown for $(\mathbf{x}, \mathbf{y}) \in (0.5, 1) \times (0.5, 1)$)

This problem is setup as a time-independent solution to the incompressible, homogeneous Euler equations. The exact solution is symmetric about the horizontal and the vertical axes and is shown for the quadrant of $(x, y) \in (0.5, 1) \times (0.5, 1)$ in Figure 3-11, where $(0.5, 0.5)$ is the center of the vortex. The simulation is initialized with the exact solution and periodic conditions on all boundaries of a 2D domain of unit dimensions (i.e., $(x, y) \in (0, 1) \times (0, 1)$). Different numerical schemes in MFIX are used to find the numerical solution after three seconds which are then compared with an exact solution to assess the quality of the results.

5.4.2 Setup

```

#####
#
# Author: Aniruddha Choudhary                      Date: Jun 2015 #
# Gresho problem: A stationary rotating vortex.      #
#                                                    #
# References:                                       #
# [1] Liska, R. & Wendroff, B. (2003). Comparison of Several #
# Difference Schemes on 1D and 2D Test Problems for the #
# Euler Equations. #
# SIAM J. Sci. Comput., 25, 995--1017. #
# doi: 10.1137/s1064827502402120 #
# #
# [2] Gresho, P. M. & Chan, S. T. (1990). On the theory of #
# semi-implicit projection methods for viscous incompressible flow #
# and its implementation via a finite element method that also #
# introduces a nearly consistent mass matrix. #
# Part 2: Implementation. #
# International Journal for Numerical Methods in Fluids, #
# 11, 621--659. #
# doi: 10.1002/fld.1650110510 #
# #
#####

RUN_NAME = 'FLD04'
DESCRIPTION = 'Gresho vortex problem'

#
# RUN CONTROL SECTION

UNITS = 'SI'
RUN_TYPE = 'NEW'

TSTOP = 3.0

DT = 1.0e-2
DT_FAC = 1.0

ENERGY_EQ = .F.
SPECIES_EQ(0) = .F.

GRAVITY = 0.0

CALL_USR = .T.

#
# NUMERICAL SECTION

MAX_NIT = 100000

TOL_RESID = 1.0e-4

LEQ_PC(1:9) = 9*'DIAG'

#

```

(continues on next page)

```

# GEOMETRY SECTION

COORDINATES = 'CARTESIAN'

ZLENGTH = 1.0    NO_K = .T.
XLENGTH = 1.0    IMAX = 40
YLENGTH = 1.0    JMAX = 40

#
# GAS-PHASE SECTION

RO_G0 = 1.0      ! (kg/m3)
MU_G0 = 0.0      ! (Pa.sec)

#
# SOLIDS-PHASE SECTION

MMAX = 0

#
# INITIAL CONDITIONS SECTION

IC_X_w(1) = 0.00 ! (m)
IC_X_e(1) = 1.00 ! (m)
IC_Y_s(1) = 0.00 ! (m)
IC_Y_n(1) = 1.00 ! (m)

IC_EP_g(1) = 1.00

IC_U_g(1) = 1.00 ! (m/sec)
IC_V_g(1) = 0.00 ! (m/sec)

#
# BOUNDARY CONDITIONS SECTION

! West, East, South, and North: Periodic BCs
!-----//

CYCLIC_X = .T.
CYCLIC_Y = .T.

#
# OUTPUT CONTROL SECTION

RES_DT = 0.1 ! (sec)
SPX_DT(1:9) = 9*0.1 ! (sec)

FULL_LOG = .T.

RESID_STRING = 'P0' 'U0' 'V0'

#
# DMP SETUP

! NODESI = 1  NODESJ = 1  NODESK = 1

```

5.4.3 Results

MFiX simulations of the Gresho vortex problem were carried out with nine spatial discretization schemes. The final flow vorticity is illustrated in Fig. 5.12 with the exact vorticity provided for reference at left. FOUP and FOUP using downwind factors are identical as expected, therefore only results for FOUP are shown. FOUP clearly fails to capture the vorticity distribution over the entire domain; Minmod and QUICKEST fail to accurately capture this distribution in the region of $0.1 m \leq r \leq 0.3 m$ (e.g., $0.6m \leq x \leq 0.8m$ along $y = 0.5$).

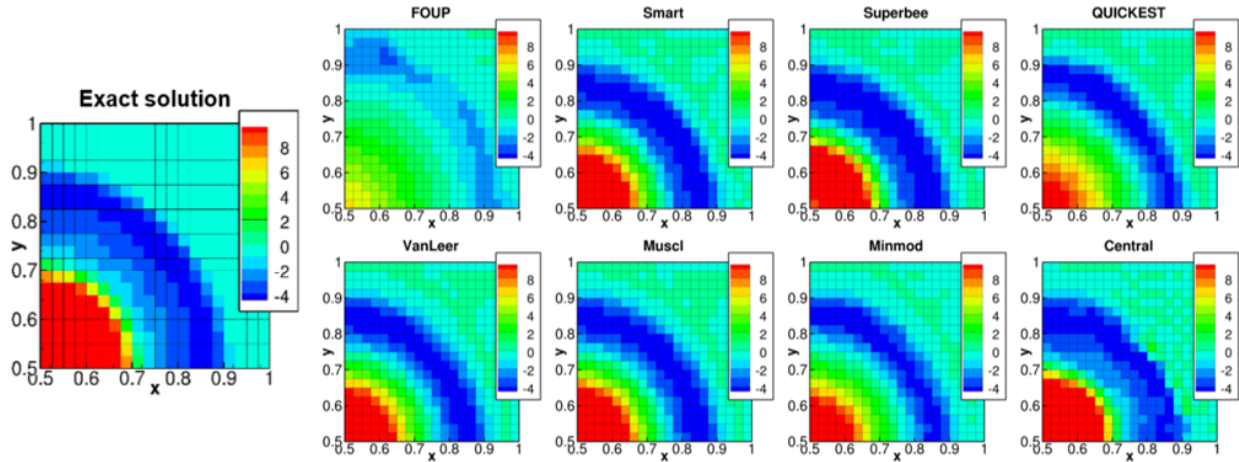


Fig. 5.12: Comparison of vorticity by different numerical schemes with the exact solution (at $T = 3$ s).

The total kinetic energy of the flow is included in Table 5.2. FOUP has the greatest loss of kinetic energy, followed by QUICKEST, and Minmod. Central scheme maintains the best agreement followed by SMART and MUSCL.

Table 5.2: Total kinetic energy of the flow field compared to the exact (initial) value for various spatial discretization schemes.

Scheme	Calculated TKE	Abs. Error	% Rel. Error
FOUP	42.64	91.25	68.15
FOUP w/DWF	42.64	91.25	68.15
Superbee	144.57	10.66	7.69
SMART	130.46	3.44	2.57
QUICKEST	93.47	40.43	30.19
MUSCL	128.45	5.45	4.07
van Leer	125.79	8.11	6.05
Minmod	112.95	20.94	15.64
Central	133.70	0.20	0.15

As a final measure of solution accuracy, the average L_2 Norm is shown in Table 3-3. Again, FOUP, QUICKEST, and Minmod demonstrate greatest amount of solution error whereas Central, SMART, and Superbee have the least amount of error.

Table 5.3: Average L2 Norms for the gas pressure (P_g), x-axial velocity (U_g) and y-axial velocity (V_g) for various spatial discretization schemes.

Scheme	P_g L ₂ -norm	U_g L ₂ -norm	V_g L ₂ -norm
FOUP	0.1430	0.1468	0.1468
FOUP w/DWF	0.1430	0.0822	0.0822
Superbee	0.0184	0.0182	0.0182
SMART	0.0078	0.0163	0.0163
QUICKEST	0.0647	0.0612	0.0612
MUSCL	0.0109	0.0200	0.0200
van Leer	0.0149	0.0107	0.0107
Minmod	0.0343	0.0408	0.0408
Central	0.0076	0.0161	0.0161

5.5 FLD05: Steady, 2D Couette flow

5.5.1 Description

Couette flow is a laminar flow of a viscous fluid between two parallel plates separated by a distance, H , with the upper wall moving at velocity, U . Different velocity distributions are obtained depending on the pressure gradient applied to the flow field. The schematic of the problem is shown in Fig. 5.13.

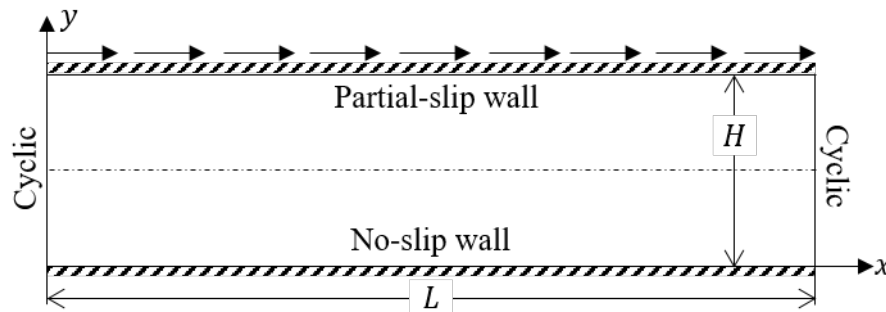


Fig. 5.13: Couette flow between two flat plates of length L , separated by a distance H with the upper wall moving at velocity U .

In this problem, the Navier-Stokes equations reduce to a second order, linear, ordinary differential equation (ODE),

$$\frac{d^2 u_g}{dy^2} = \frac{1}{\mu_g} \frac{dp}{dx} \quad (5.7)$$

where μ_g is the fluid viscosity, and dp/dx is the prescribed pressure drop across the length of the pipe. The no-slip and partial-slip boundary conditions are specified by

$$\begin{aligned} u_g(0) &= 0, \\ u_g(H) &= U. \end{aligned} \quad (5.8)$$

The analytical solution is given by,

$$u_g(y) = \frac{1}{2\mu} \frac{dp}{dx} (y^2 - yH) + U \frac{y}{H} \quad (5.9)$$

5.5.2 Setup

```
#####
#
# Author: Avinash Vaidheeswaran           Date: July 2016 #
# Couette flow problem:                   #
#                                         #
# The south wall is held stationary and the north wall moves with a #
# velocity U. Cyclic boundary conditions along x direction with #
# adverse, zero, and favorable pressure gradients. #
#                                         #
#####

RUN_NAME      = 'FLD05'
DESCRIPTION    = 'Couette flow test cases'

#
# RUN CONTROL SECTION

UNITS = 'SI'
RUN_TYPE = 'NEW'

ENERGY_EQ = .F.
SPECIES_EQ(0) = .F.

GRAVITY = 0.0

CALL_USR = .T.

#
# NUMERICAL SECTION

MAX_NIT = 50000
TOL_RESID = 1.0E-10

LEQ_PC = 9*'NONE'

#
# GEOMETRY SECTION

COORDINATES = 'CARTESIAN'

XLENGTH = 1.00      IMAX = 3
ZLENGTH = 1.00      NO_K = .T.

YLENGTH = 0.01      JMAX = 8

#
# GAS-PHASE SECTION

RO_g0 = 1.00      ! (kg/m3)
MU_g0 = 5.00d-6   ! (Pa.s)

#
# SOLIDS-PHASE SECTION

MMAX = 0
```

(continues on next page)

(continued from previous page)

```

#
# INITIAL CONDITIONS SECTION

IC_X_w(1) = 0.00 ! (m)
IC_X_e(1) = 1.00 ! (m)
IC_Y_s(1) = 0.00 ! (m)
IC_Y_n(1) = 0.01 ! (m)

IC_EP_g(1) = 1.00

IC_P_g(1) = 0.00 ! (Pa)

IC_U_g(1) = 0.00 ! (m/sec)
IC_V_g(1) = 0.00 ! (m/sec)

#
# BOUNDARY CONDITIONS SECTION

! The north wall has a constant velocity of 10.0 m/s, and is set using
! a partial slip wall (PSW):  $dU/dn + hw(U-U_w) = 0$  where  $U_w = 10.0$  m/s
! and  $hw=unspecified$  (i.e., no-slip moving wall).
!-----//
BC_X_w(1) = 0.00 ! (m)
BC_X_e(1) = 1.00 ! (m)
BC_Y_s(1) = 0.01 ! (m)
BC_Y_n(1) = 0.01 ! (m)

BC_TYPE(1) = 'PSW'

BC_Uw_g(1) = 10.00 ! (m/sec)
BC_Vw_g(1) = 0.00 ! (m/sec)

! The south wall is a stationary no-slip wall (NSW).
!-----//
BC_X_w(2) = 0.00 ! (m)
BC_X_e(2) = 1.00 ! (m)
BC_Y_s(2) = 0.00 ! (m)
BC_Y_n(2) = 0.00 ! (m)

BC_TYPE(2) = 'NSW'

! The east and west boundaries are set at runtime as cyclic with a
! specified pressure drop (DELP_X)
!-----//
CYCLIC_X_PD = .TRUE.
DELP_X = -3.0

#
# OUTPUT CONTROL SECTION

RES_DT = 1.

```

(continues on next page)

(continued from previous page)

```

FULL_LOG      = .T.
SPX_DT       = 9*1.

RESID_STRING  = 'P0' 'U0' 'V0'

# _____
# DMP SETUP
    
```

5.5.3 Results

Simulations were conducted for seven pressure drops, $[-3.0, -2.0, -1.0, 0.0, 1.0, 2.0, 3.0]$ Pa, specified across the x-axial cyclic boundaries. Four mesh levels [8, 16, 32, 64] in the y-axial direction were used to assess discretization error.

The analytical and numerical solutions for the zero pressure drop case are shown in Fig. 5.14. For clarity, only a subset of the numerical solutions is presented, resulting in a slight offset/shift in displayed data points. Note that the analytical solution reduces to a linear variation in velocity between the lower and upper walls when the specified pressure drop is zero. For this case, the absolute error in velocity is bounded above by $10^{-6} \text{ m} \cdot \text{sec}^{-1}$ and is observed for the finest grid resolution (64 mesh). Further investigation (not presented) indicated that the increase in numerical error is attributed to the solution mechanism of the linear equation system. This error can be reduced by modifying the default linear equation solver settings (e.g., tighten convergence criteria, increase number of iterations, etc.).

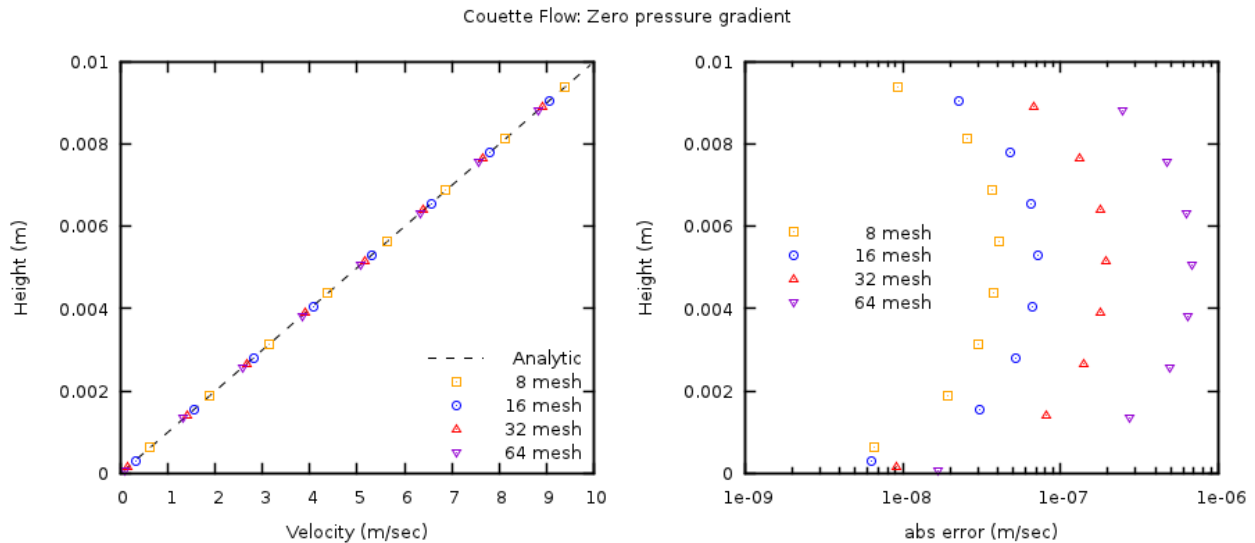


Fig. 5.14: Couette flow with a zero pressure gradient with four grid resolutions.

The analytical and numerical solutions for the adverse and favorable pressure drops are shown in Fig. 5.15 and Fig. 5.16. Again, only a subset of the numerical solutions is presented resulting in a slight offset/shift in displayed data points. These cases demonstrate a second order rate of convergence with respect to grid size which is attributed to the second-order discretization of the viscous stress term.

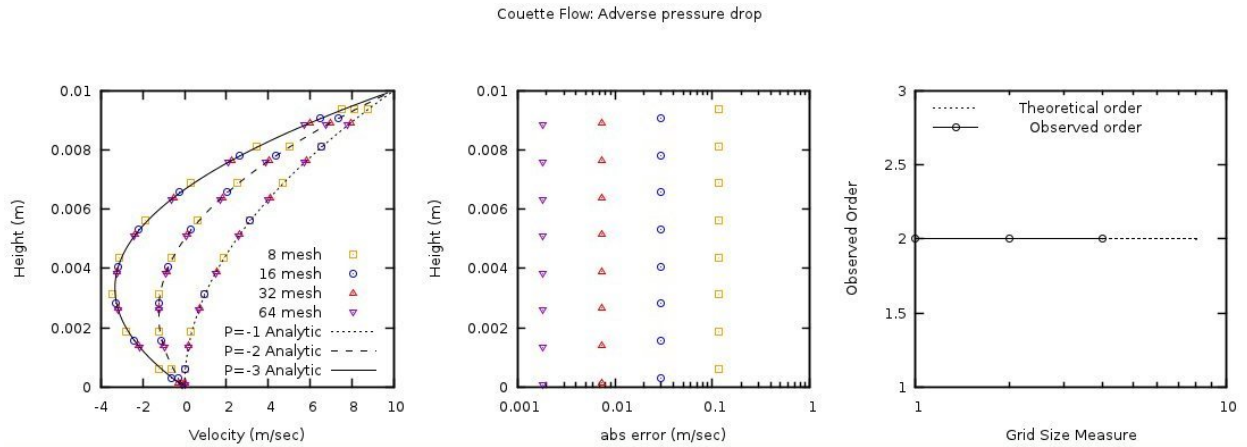


Fig. 5.15: Adverse pressure gradient (-1, -2, -3 Pa) Couette flow with four grid resolutions. Absolute error and observed order of accuracy only shown for -3 Pa pressure gradient.

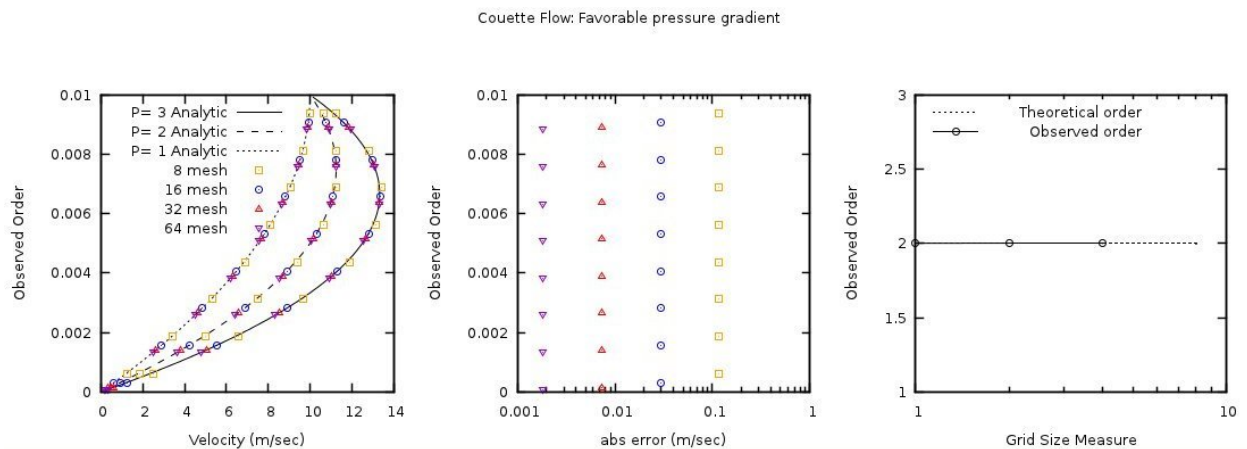


Fig. 5.16: Favorable pressure gradient (1, 2, 3 Pa) Couette flow with four grid resolutions. Absolute error and observed order of accuracy only shown for 3 Pa pressure gradient.

5.6 FLD06: Steady, 2D multi-component species transport

5.6.1 Description

The 2D multi-component species problem investigates the transport of three non-reacting fluid phase species that follow ideal gas behavior. Illustrated in Fig. 5.17, three separate mass inflows are used to inject three distinct gas species into the system. The species mix as the fluid passes through the domain such that they are well-mixed when the fluid reaches the outlet. The resulting species mass fractions, X_{gi} , for the well-mixed flow are given analytically by,

$$X_{gi} = \frac{MW_{gi}}{\sum_k MW_{gk}} \quad (5.10)$$

where MW_{gi} is the molecular weight of the i^{th} gas phase species.

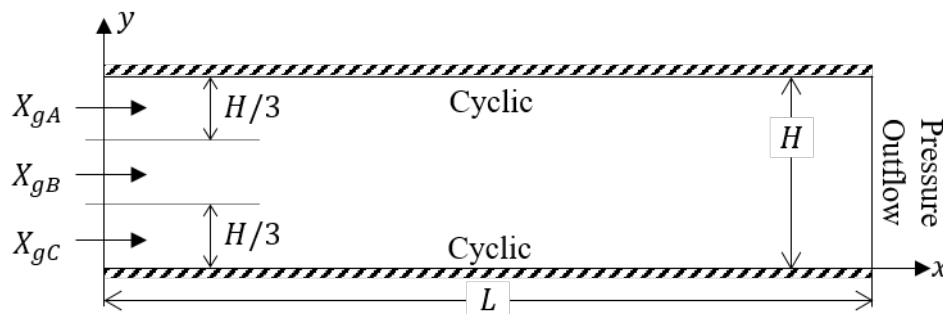


Fig. 5.17: Multicomponent species transport.

5.6.2 Setup

```
#####
#
# Author: Avinash Vaidheeswaran           Date: July 2016 #
# Species transport problem:                #
#                                           #
# Species are introduced through mass infow BCs. The north and south #
# boundaries are free-slip walls. The east boundary is a pressure #
# outlet.                                   #
#                                           #
# ----- CYCLIC BC -----                #
# MI -3->                                -4-> #
# MI -2->                                -4-> PO #
# MI -1->                                -4-> #
# ----- CYCLIC BC -----                #
#                                           #
#####

RUN_NAME = 'FLD06'
DESCRIPTION = 'Species transport test cases'

#
# RUN CONTROL SECTION
```

(continues on next page)

(continued from previous page)

```
UNITS = 'SI'
RUN_TYPE = 'NEW'

TSTOP = 10.0d6

DT = 0.01
DT_FAC = 1.00

ENERGY_EQ = .F.
SPECIES_EQ(0) = .T.

GRAVITY = 0.0

CALL_USR = .T.

#
# NUMERICAL SECTION

DISCRETIZE(1:9) = 9*3
CHI_SCHEME = .T.

NORM_G = 1.0
DETECT_STALL = .F.

TOL_RESID_X = 1.0d-6

#
# GEOMETRY SECTION

COORDINATES = 'CARTESIAN'

ZLENGTH = 1.00      NO_K = .T.
XLENGTH = 2.00      IMAX = 200
YLENGTH = 0.03      JMAX = 3      CYCLIC_Y=.T.

#
# GAS-PHASE SECTION

NMAX_g = 3
SPECIES_g(1) = 'A'
SPECIES_g(2) = 'B'
SPECIES_g(3) = 'C'

MW_g(1) = 1.0
MW_g(2) = 10.0
MW_g(3) = 25.0

DIF_g0= 1.0d-3

#
# SOLIDS-PHASE SECTION

MMAX = 0

#
# INITIAL CONDITIONS SECTION
```

(continues on next page)

(continued from previous page)

```

IC_X_w(1) = 0.00 ! (m)
IC_X_e(1) = 2.00 ! (m)
IC_Y_s(1) = 0.00 ! (m)
IC_Y_n(1) = 0.03 ! (m)

IC_EP_g(1) = 1.00 ! (1)

IC_T_G(1) = 293.15 ! (K)
IC_P_G(1) = 101.0d3 ! (Pa)

IC_U_g(1) = 0.0 ! (m/sec)
IC_V_g(1) = 0.0 ! (m/sec)

IC_X_g(1,1) = 0.03 ! N2
IC_X_g(1,2) = 0.27 ! H2
IC_X_g(1,3) = 0.70 ! H2O

#
# BOUNDARY CONDITIONS SECTION

! The west boundary IN1 is a velocity inlet
!-----//
BC_X_w(1:3) = 0.00 0.00 0.00 ! (m)
BC_X_e(1:3) = 0.00 0.00 0.00 ! (m)
BC_Y_s(1:3) = 0.00 0.01 0.02 ! (m)
BC_Y_n(1:3) = 0.01 0.02 0.03 ! (m)

BC_X_G(1:3,1) = 1.00 0.00 0.00 ! (N2)
BC_X_G(1:3,2) = 0.00 1.00 0.00 ! (H2)
BC_X_G(1:3,3) = 0.00 0.00 1.00 ! (H2O)

BC_TYPE(1:3) = 3*'MI'

BC_EP_g(1:3) = 3*1.00

BC_T_g(1:3) = 3*293.15 ! (Pa)
BC_P_g(1:3) = 3*101.0d3 ! (Pa)

BC_U_g(1:3) = 3*0.25 ! (m/s)
BC_V_g(1:3) = 3*0.00 ! (m/s)

! The east boundary is a pressure outlet.
!-----//

BC_X_w(4) = 2.00 ! (m)
BC_X_e(4) = 2.00 ! (m)
BC_Y_s(4) = 0.00 ! (m)
BC_Y_n(4) = 0.03 ! (m)

BC_TYPE(4) = 'PO'

BC_T_g(4) = 293.15 ! (K)
BC_P_g(4) = 101.0d3 ! (Pa)

```

(continues on next page)

(continued from previous page)

```
#
# OUTPUT CONTROL SECTION

RES_DT =          0.1
SPX_DT(1:9) = 9*0.1

FULL_LOG = .F.
RESID_STRING =    'P0' 'U0' 'V0'

#
# DMP SETUP

! NODESI = 1  NODESJ = 1  NODESK = 1
```

5.6.3 Results

The simulation was performed using the SMART discretization scheme with the χ correction to ensure species conservation. The average L_2 norm for the three species mass fractions were calculated for consecutive time steps. The simulation was considered converged when all three norms were less than 10^{-8} . The species mass fractions at the outflow plane and the L_2 norm between the MFIX and analytical solution are shown in Table 5.4. Two additional simulations were carried out where the solution order of the species equations was varied (e.g., ABC, BCA, CAB). No dependence was found on the solution order of the species equations (results not shown).

Table 5.4: Average species mass fractions at the outflow and average L_2 Norms between the analytical and MFIX species mass fraction for the well-mixed fluid.

Species	MFIX	L_2 norm
A	0.027778	5.86e-7
B	0.277776	2.07e-6
C	0.694446	1.48e-6

5.7 FLD07: Steady, 2D fully-developed, turbulent channel flow

5.7.1 Description

This case uses 2D, fully-developed turbulent channel flow between two horizontal, parallel plates separated by a width, W , to assess the single phase $k-\epsilon$ model in MFIX. Periodic boundaries with a specified pressure drop are imposed in the y -direction as shown in Fig. 5.18.

The pressure drop along the channel is equated to the shear stress at the walls, τ_w .

$$W \frac{dP_g}{dy} = 2\tau_w \tag{5.11}$$

The shear stress is related to the gas density, ρ_g , and friction velocity, v_* ,

$$\tau_w = \rho_g v_*^2, \tag{5.12}$$

where, the friction velocity, is given by the Reynolds number.

$$\text{Re}_\tau = \frac{\rho_g v_* (W/2)}{\mu_g} \tag{5.13}$$

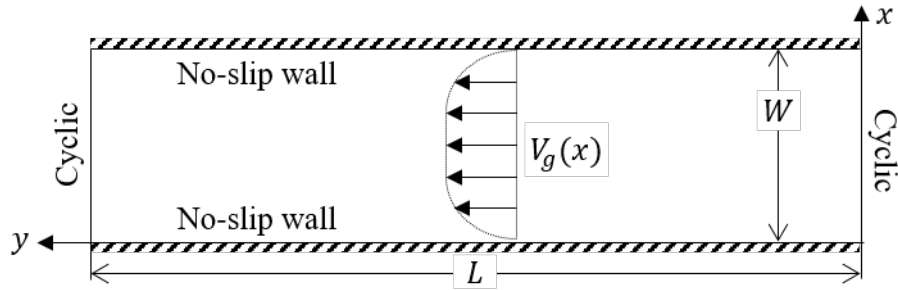


Fig. 5.18: Turbulent flow in a 2D channel

5.7.2 Setup

```
#####
#
# Author: Avinash Vaidheeswaran           Date: July 2016 #
# Turbulent flow in a pipe problem:       #
#                                         #
# Turbulent flow through a channel is simulated and the results are #
# compared with the data from DNS        #
#                                         #
#####

RUN_NAME = 'FLD07'
DESCRIPTION = 'Turbulent channel flow'

#-----
# RUN CONTROL SECTION

UNITS = 'SI'
RUN_TYPE = 'NEW'

TSTOP = 1.0d8

DT = 0.02

ENERGY_EQ = .F.
SPECIES_EQ(0) = .F.

GRAVITY = 0.0

CALL_USR = .T.

#-----
# NUMERICAL SECTION

DISCRETIZE(1:9) = 9*2

NORM_g = 0.0

#-----
# GEOMETRY SECTION

COORDINATES = 'CARTESIAN'
```

(continues on next page)

(continued from previous page)

```

ZLENGTH = 1.00      NO_K = .T.
XLENGTH = 2.00      IMAX = 8
YLENGTH = 1.00      JMAX = 4

#-----
# GAS-PHASE SECTION

RO_g0 = 1.0         ! (kg/m3)
MU_g0 = 1.0d-04    ! (Pa.s)

TURBULENCE_MODEL = 'K_EPSILON'

MU_GMAX = 1.0d6    ! (Pa.s)

#-----
# SOLIDS-PHASE SECTION

MMAX = 0

#-----
# INITIAL CONDITIONS SECTION

IC_X_w(1) = 0.0     ! (m)
IC_X_e(1) = 2.0     ! (m)
IC_Y_s(1) = 0.0     ! (m)
IC_Y_n(1) = 1.0     ! (m)

IC_EP_G(1) = 1.0

IC_P_G(1) = 0.0     ! (Pa)

IC_U_G(1) = 1.0d-6 ! (m/sec)
IC_V_G(1) = 1.0     ! (m/sec)

IC_K_TURB_G(1) = 0.010 ! (m2/s2)
IC_E_TURB_G(1) = 0.001 ! (m2/s3)

#-----
# BOUNDARY CONDITIONS SECTION

! Flow boundaries: Periodic with specified pressure drop
!-----//
CYCLIC_Y_PD = .T.
DELP_Y = @(0.0543496*0.0543496) ! (Pa)

! The east and west boundaries are no-slip walls (NSW)
!-----//

BC_X_w(1:2) = 0.0    2.0 ! (m)
BC_X_e(1:2) = 0.0    2.0 ! (m)
BC_Y_s(1:2) = 0.0    0.0 ! (m)
BC_Y_n(1:2) = 1.0    1.0 ! (m)

BC_TYPE(1:2) = 2*'NSW'

```

(continues on next page)

(continued from previous page)

```

#
# OUTPUT CONTROL SECTION

RES_DT = 1.0d6
SPX_DT(1:9) = 9*1.0

FULL_LOG = .F.
RESID_STRING = 'P0' 'U0' 'V0' 'K0'

#
# DMP SETUP

! NODESI = 1   NODESJ = 2   NODESK = 1

```

5.7.3 Results

The pressure drop in the y-axial direction, domain length and width, and gas density were chosen to reflect the conditions of Lee and Moser [14] for $Re_\tau = 543$. The DNS dataset was accessed on November 10, 2016 from http://turbulence.ices.utexas.edu/channel2015/data/LM_Channel_0550_mean_prof.dat.

Transient simulations were performed for better numerical stability. The solution was considered converged when the L_2 norms for the gas velocity components, u_g and v_g , turbulent kinetic energy, k_g , and rate of turbulent kinetic energy dissipation, ϵ_g , were all less than 10^{-10} .

Simulations were conducted for three mesh levels [6, 12, 18] in the x-axial direction. Mesh levels were selected to ensure that the stream-ways velocity components in computational cells adjacent to the wall were located outside the buffer layer. Specifically, the first stream-ways velocity component should be located at least 30 *wall units* from the wall to be consistent with the $k - \epsilon$ model wall function implementation.

$$\frac{\Delta x}{2} \frac{v_* \rho_g}{\mu_g} > 30 \quad (5.14)$$

The MFiX results are shown in Fig. 5.19 along with the direct numerical simulation (DNS) data of Lee and Moser [14] for $Re_\tau = 543$. The velocity profiles for the three mesh levels are shown on the left whereas the normalized velocity profiles with respect to wall units are shown on the right.

5.8 FLD08: Steady, 2D turbulent pipe flow

5.8.1 Description

This case uses turbulent flow in a pipe of length L and radius R to assess the single phase $k-\epsilon$ model in MFiX. A 2D axisymmetric domain is used to define the pipe geometry, and pressure boundaries are used to induce flow in the positive y-axial direction as shown in Fig. 5.20. The results are compared with the experimental data of Zagarola and Smits [36].

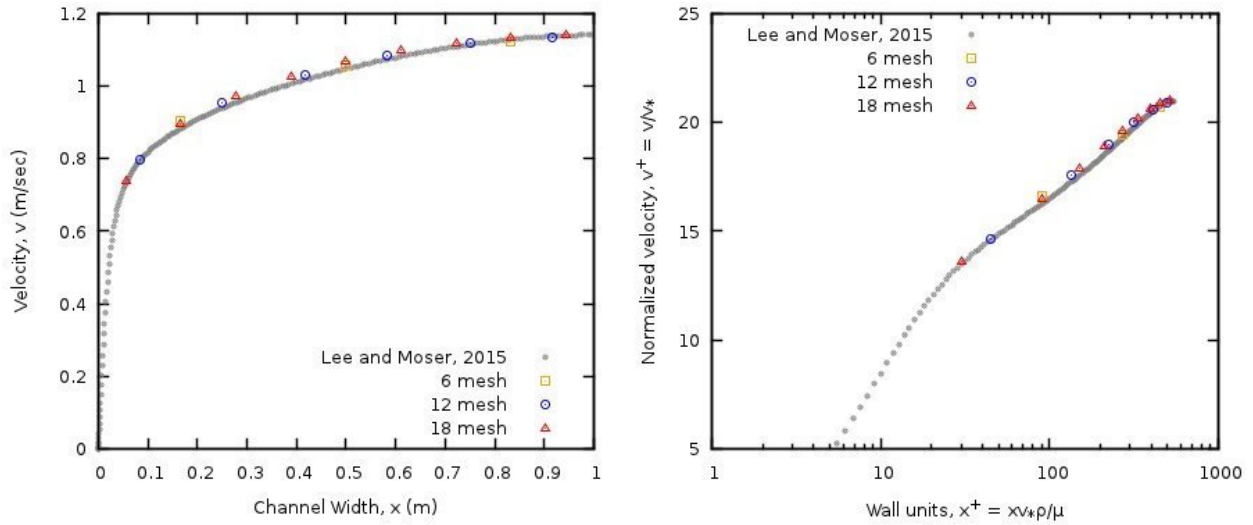


Fig. 5.19: 2D, fully developed, turbulent channel flow with the DNS data of Lee and Moser [14] ; (Left) Velocity profile; (Right) Non-dimensionalized channel width and velocity profile.

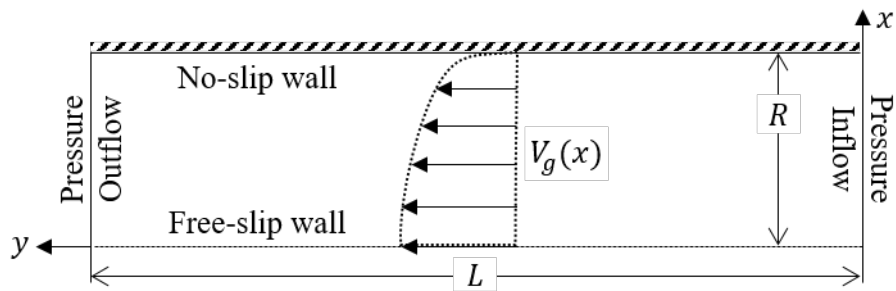


Fig. 5.20: Turbulent flow in a pipe

5.8.2 Setup

```
#####
#
# Author: Avinash Vaidheeswaran                               Date: July 2016 #
# Turbulent flow in a pipe problem:                            #
#                                                              #
# Turbulent flow through a pipe is simulated and the results are #
# compared with the data from Princeton superpipe.           #
#                                                              #
# Data source, accessed November, 2016                        #
# http://www.princeton.edu/~gasdyn/Superpipe_data/4.1727E+04.txt #
#                                                              #
#      -*-*-*-*-*-*-*-*-*- FSW 3 *-*-*-*-*-*-*-*-*-*- #
#      -1->                                                    -2-> #
#      PI -1->                                                    -2-> PO #
#      -1->                                                    -2-> #
#      ----- NSW 4 ----- #
#                                                              #
#####

RUN_NAME = 'FLD08'
DESCRIPTION = 'Pipe flow case'

#-----
# RUN CONTROL SECTION

UNITS = 'SI'
RUN_TYPE = 'NEW'

TSTOP = 1.0d8

DT = 0.1
DT_FAC = 1.0

ENERGY_EQ = .F.
SPECIES_EQ = .F.

GRAVITY = 0.0

CALL_USR = .T.

#-----
# NUMERICAL SECTION

DETECT_STALL = .F.

NORM_g = 0.0

#-----
# GEOMETRY SECTION

COORDINATES = 'CYLINDRICAL'

ZLENGTH = 6.23819 NO_K = .T.
XLENGTH = 0.06468 IMAX = 16
YLENGTH = 8.00 JMAX = 100
```

(continues on next page)

(continued from previous page)

```

#
# GAS-PHASE SECTION

RO_g0 = 1.1620      ! (kg/m3)
MU_g0 = 1.8487d-05 ! (Pa.s)

TURBULENCE_MODEL = 'K_EPSILON'

MU_GMAX = 1.0d6     ! (Pa.s)

#
# SOLIDS-PHASE SECTION

MMAX = 0

#
# INITIAL CONDITIONS SECTION

IC_X_w(1) =      0.00      ! (m)
IC_X_e(1) =      0.06468   ! (m)
IC_Y_s(1) =      0.00      ! (m)
IC_Y_n(1) =      8.00      ! (m)

IC_EP_G(1) =     1.00      ! (-)

IC_P_G(1) =      0.00      ! (Pa)

IC_U_G(1) =      0.00      ! (m/sec)
IC_V_G(1) =      5.00      ! (m/sec)

IC_K_TURB_G(1) = 0.047     ! (m2/s2)
IC_E_TURB_G(1) = 0.213     ! (m2/s3)

#
# BOUNDARY CONDITIONS SECTION

! The south boundary is a pressure inflow
!-----//
BC_X_w(1) =      0.00      ! (m)
BC_X_e(1) =      0.06468   ! (m)
BC_Y_s(1) =      0.00      ! (m)
BC_Y_n(1) =      0.00      ! (m)

BC_TYPE(1) =     'PI'

BC_EP_g(1) =     1.0       ! (-)

BC_P_g(1) =      20.684    ! (Pa)

BC_K_TURB_G(1) = 0.047     ! (m2/s2)
BC_E_TURB_G(1) = 0.213     ! (m2/s3)

! The north boundary is a pressure outlet.
!-----//

```

(continues on next page)

(continued from previous page)

```
BC_X_w(2) =      0.00      ! (m)
BC_X_e(2) =      0.06468   ! (m)
BC_Y_s(2) =      8.00      ! (m)
BC_Y_n(2) =      8.00      ! (m)

BC_TYPE(2) =      'PO'

BC_P_g(2) =      0.00      ! (Pa)

! The west boundary is a free-slip walls (FSW)
!-----//

BC_X_w(3) =      0.00      ! (m)
BC_X_e(3) =      0.00      ! (m)
BC_Y_s(3) =      0.00      ! (m)
BC_Y_n(3) =      8.00      ! (m)

BC_TYPE(3) =      'FSW'

! The east boundary is a no-slip wall (NSW)
!-----//

BC_X_w(4) =      0.06468   ! (m)
BC_X_e(4) =      0.06468   ! (m)
BC_Y_s(4) =      0.00      ! (m)
BC_Y_n(4) =      8.00      ! (m)

BC_TYPE(4) =      'NSW'

#-----
# OUTPUT CONTROL SECTION

RES_DT = 1.0d8
SPX_DT(1:9) = 9*1.0d8

FULL_LOG = .F.
RESID_STRING = 'P0' 'U0' 'V0' 'K0'

#-----
# DMP SETUP

! NODESI = 1  NODESJ = 1  NODESK = 1
```

5.8.3 Results

Pressure drop in the y-axial direction, domain width, gas density and viscosity were chosen to reflect the conditions of [36] for $Re = 41727$. A transient simulation was performed for better numerical stability. The solution was considered converged when the L_2 norms for the gas velocity components, u_g and v_g , turbulent kinetic energy, k_g , and rate of turbulent kinetic energy dissipation, ϵ_g , were all less than 10^{-10} .

The simulation was conducted with 16 cells in the x-axial direction. The mesh level ensures that the stream-ways velocity components in computational cells adjacent to the wall were located outside the buffer layer. Specifically, the first stream-ways velocity component was located at least 30 *wall units* from the wall to be consistent with the $k - \epsilon$ model wall function implementation.

$$\frac{\Delta x}{2} \frac{v_* \rho_g}{\mu_g} > 30 \quad (5.15)$$

Here, the friction velocity, v_* , is given by the Karman number, R^+ [36],

$$R^+ = \frac{Dv_*}{\nu} \quad (5.16)$$

where D is pipe diameter, and ν is the kinematic viscosity.

The MFIX results are shown in Fig. 5.21 along with the experimental data of Zagarola and Smits [36] for $Re = 41727$. The experimental dataset was accessed on November 10, 2016 from http://www.princeton.edu/~gasdyn/Superpipe_data/4.1727E+04.txt

The velocity profile is shown on the left, and the normalized velocity profile with respect to wall units is shown on the right. The velocity profile is given for two locations near the pipe exit, 7.2 m and 8.0 m respectively, with the maximum difference less than $10^{-2} \text{ m}\cdot\text{sec}^{-1}$, indicating that the flow is fully developed. The largest discrepancy between the experimental measurements and the simulation results occurs at the centerline of the domain where the simulation under-predicts the observed velocity by $0.3 \text{ m}\cdot\text{sec}^{-1}$.

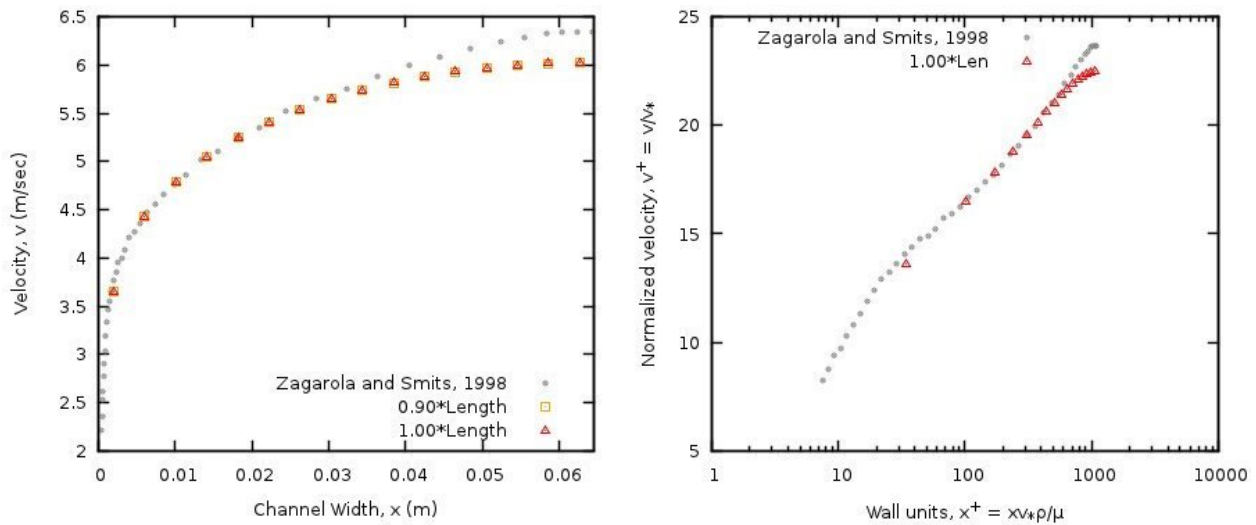


Fig. 5.21: 2D, turbulent pipe flow with the experimental data of DNS data of Zagarola and Smits [36]; (Left) Velocity profiles; (Right) Nondimensionalized channel width and velocity profile.

MFIX-DEM CODE VERIFICATION TEST CASES

The test cases presented in this chapter for the MFIX-DEM are summarized in [Table 6.1](#). Test cases have been selected based on the criteria for verification test selection outlined in [Section 3](#). All cases are executed in serial mode unless explicitly noted.

Table 6.1: Summary of MFiX-DEM tests by feature.

	01	02	03	04	05	06
Frequency†	C	C	C	C	C	C
Reference Dataset‡	A	A	A	A	P	A
Dimension	1D	1D	1D	1D	2D	1D
Coupled						✓
Momentum	✓	✓		✓	✓	✓
Thermal Energy						
Species Mass						
Time-Stepping						
Euler	✓					✓
Adams-Bashforth	✓	✓	✓	✓	✓	
Spring-Dashpot						
Linear	✓	✓	✓	✓	✓	✓
Hertzian					✓	
Collisions						
Particle-particle			✓		✓	
Particle-wall	✓	✓	✓	✓	✓	
Friction						
Particle-particle					✓	
Particle-wall				✓	✓	
Distributed Memory						
Shared Memory						

† C-Incorporated into the continuous integration server; M-Monthly; Q-Quarterly; X-Manual; D-Disabled

‡ A-Analytical solution; P-Published benchmark data; R-Regression data from previous code versions

6.1 DEM01: Freely-falling particle

This case serves to verify the MFiX-DEM linear spring-dashpot collision model as well as the accuracy of the time-stepping methods. This case is based on the work of Chen et al. [4] and the MFiX-DEM case was originally reported in Garg et al. [8].

6.1.1 Description

A smooth (frictionless), spherical particle falls freely under gravity from an initial height, h_0 , and bounces upon collision with a fixed wall. The translating motion of the particle is described in three stages, as depicted in Fig. 6.1. An analytic expression for particle motion during each stage is obtained.

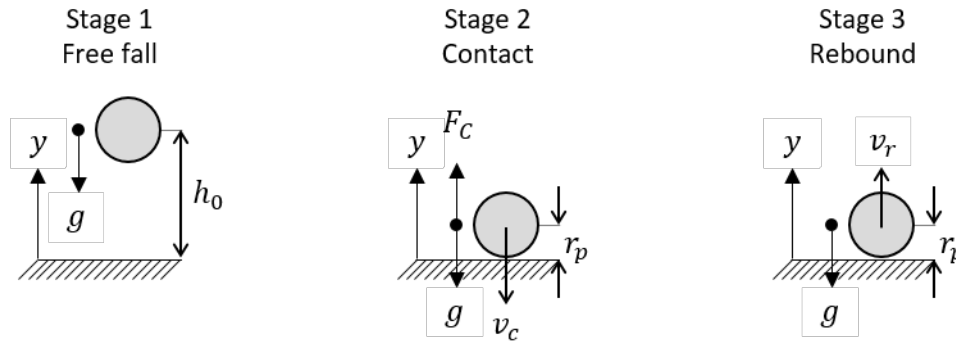


Fig. 6.1: A particle with radius r_p falling onto a fixed wall from an initial height of h_0 where \mathbf{g} is the gravitational force, \mathbf{F}_C is repulsive particle-wall collision force, \mathbf{v}_c is the pre-collision particle velocity, and \mathbf{v}_r is the post-collision particle velocity.

Stage 1: Free fall

A force balance on the particle provides an expression for particle motion during free fall,

$$\frac{d^2y}{dt^2} = -g; \quad y(0) = h_0; \quad \frac{dy}{dt}(0) = 0 \quad (6.1)$$

where y is the center position of the particle with respect to the wall and g is the acceleration due to gravity. The particle is initially at rest with a center distance of h_0 above the wall. The instantaneous velocity, v , and particle center position are given by

$$v(t) = -gt \quad (6.2)$$

$$y(t) = h_0 - \frac{1}{2}gt^2 \quad (6.3)$$

Stage 2: Contact

The free fall stage ends and the contact stage begins when the particle center position is equal to the particle radius. The particle-wall collision is treated using the linear spring-dashpot model such that the force balance on the particle during contact gives

$$\begin{aligned} \frac{d^2y}{dt^2} + 2\beta\omega_o \frac{dy}{dt} + \omega_o^2 y &= \omega_o^2 r_p - g; \\ y(0) = r_p; \quad \frac{dy}{dt}(0) &= -\sqrt{2g(h_0 - r_p)} \end{aligned} \quad (6.4)$$

where $\beta = \eta_n / (2\sqrt{k_n m_p})$ and $\omega_o = \sqrt{k_n / m_p}$. Here, k_n and η_n are the normal spring coefficient and damping coefficients for the particle-wall collision, and m_p is the particle mass. The initial particle velocity is obtained from combining Eq.6.2 and Eq.6.3 when the particle center position is equal to its radius. The instantaneous velocity and particle center position during contact for an underdamped system, $\beta < 1$, are given by

$$v(t) = \left[-\sqrt{2g(h_0 - r_p)} \cos(\phi t) + \frac{\beta\omega_o \sqrt{2g(h_0 - r_p)} - g}{\phi} \sin(\phi t) \right] \exp(-\beta\omega_o t) \quad (6.5)$$

$$y(t) = \left[\frac{g}{\omega_o^2} \cos(\phi t) + \frac{-\sqrt{2g(h_0 - r_p)} - \frac{\beta g}{\omega_o}}{\phi} \sin(\phi t) \right] \exp(-\beta\omega_o t) + \left(r_p - \frac{g}{\omega_o^2} \right) \quad (6.6)$$

where, $\phi = \sqrt{1 - \beta^2}\omega_o$

Stage 3: Rebound

The contact stage ends and the rebound stage begins when the particle center position is again equal to the particle radius. A force balance on the particle leads to an expression for the particle motion,

$$\frac{d^2 y}{dt^2} = -g; \quad y(0) = r_p; \quad \frac{dy}{dt}(0) = v_c. \quad (6.7)$$

The velocity at the start of the rebound stage is equal to the velocity at the end of the contact stage, v_c . It is obtained by solving Eq.6.6 for time when the particle center position is equal to the particle radius, then substituting the result into equation Eq.6.5. The instantaneous velocity, v , and particle center position, y , are given by

$$v(t) = v_c - gt \quad (6.8)$$

$$y(t) = r_p + v_c t - \frac{1}{2}gt^2. \quad (6.9)$$

6.1.2 Setup

Table 6.2: DEM-01 Setup, Initial and Boundary Conditions.

Computational/Physical model			
1D, Transient			
Granular flow (no gas)			
Gravity			
Thermal energy equation is not solved			
Geometry			
Coordinate system	Cartesian		
x-length	1.0	(m)	
y-length	1.0	(m)	
z-length	1.0	(m)	
Solids Properties			
Normal spring coefficient, k_n	varied	(N·m ⁻¹)	
Restitution coefficient, e_n	varied	()	
Friction coefficient, μ	0.0	()	
Solids 1 Type			
Diameter, d_p	0.2	(m)	
Density, ρ_s	2600	(kg·m ⁻³)	
Boundary Conditions			
All boundaries	Solid walls		

6.1.3 Results

Simulations of a freely-falling particle dropped from an initial height of 0.5m were conducted for four particle-wall normal spring coefficients, $[1.0, 2.5, 5.0, 10.0] \times 10^4 \text{ N}\cdot\text{m}^{-1}$, and five restitution coefficients, $[0.6, 0.7, 0.8, 0.9, 1.0]$. The test using a normal spring coefficient of $10^4 \text{ N}\cdot\text{m}^{-1}$ and restitution coefficient 0.6 were unsuccessful because this combination leads to the particle center crossing the fixed boundary indicating that the particle is located outside of the domain. The following results were obtained using the Euler time stepping method.

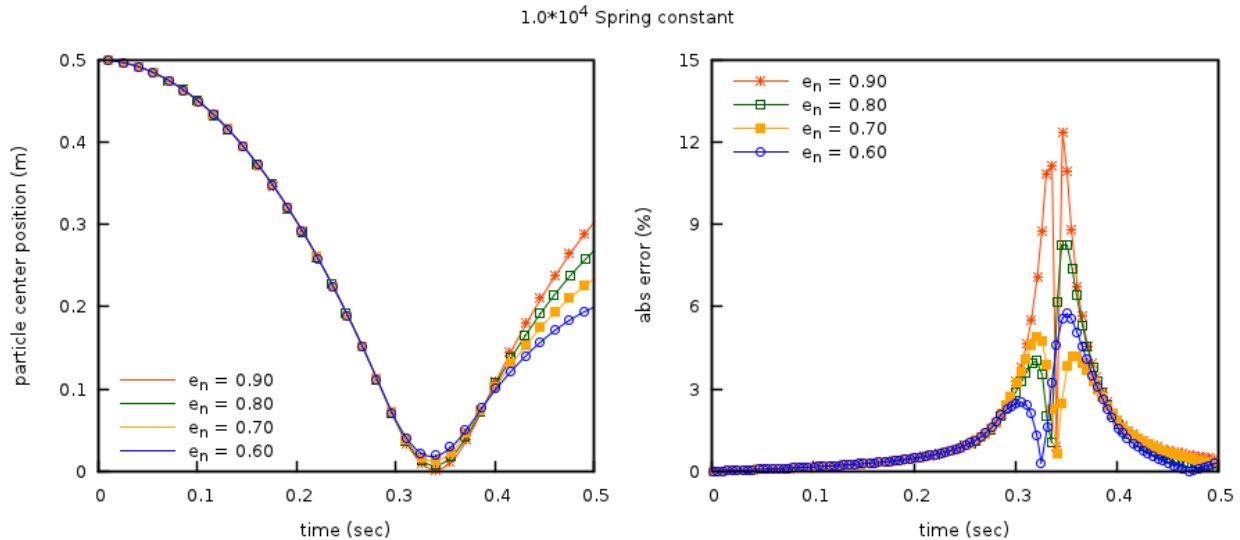


Fig. 6.2: Comparison of analytical solution and DEM results for a freely-falling particle using the Euler time-stepping method for varying restitution coefficient, normal spring coefficient, $\mathbf{k}_n = 10^4 \text{ N}\cdot\text{m}^{-1}$. (Left) Particle center position; analytical solutions shown as continuous lines, MFiX-DEM results as points. (Right) Percent absolute relative error between the analytical and MFiX-DEM particle center positions.

The particle center position for cases using a normal spring coefficient of $10^4 \text{ N}\cdot\text{m}^{-1}$ are shown in Fig. 6.2. These cases demonstrate the largest errors in particle center position during the contact stage. The large error is attributed to the particle center position approaching the fixed boundary, $y \rightarrow 0$, during the contact stage. This leads to near-zero values used in the absolute value of the relative error calculations. In all other cases, the absolute percent relative error remains below 3% with errors decreasing with increasing normal spring coefficient.

The particle velocity for cases using a slightly stiffer normal spring coefficient of $10^5 \text{ N}\cdot\text{m}^{-1}$ are shown in Fig. 6.3. Again, the large errors are primarily attributed to near-zero values used in the relative error calculations. The initial spike in error arises at the peak of the contact stage when the particle trajectory reverses, passing through zero. Similarly, large relative errors occur at the peak of the rebound stage when the particle trajectory again reverses direction.

Analysis of the time-stepping methods is limited to the free-fall stage and excludes error arising from the collision model. Pre- and post-collision results using the Euler and Adams-Bashforth methods with a normal spring coefficient of $10^5 \text{ N}\cdot\text{m}^{-1}$ are shown in Fig. 6.4. During the free fall stage (pre-collision), the Euler method shows a linear accumulation of error in particle position whereas the error in particle velocity is zero. The Adams-Bashforth method shows no (zero) error for both particle position and velocity. These results are consistent across all cases.

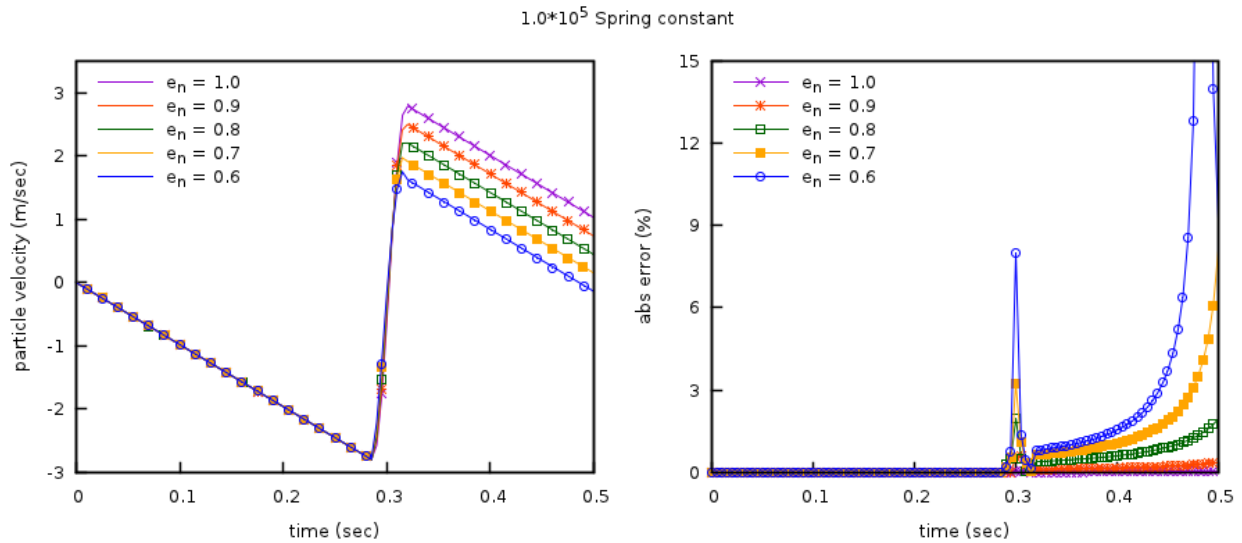


Fig. 6.3: Comparison of analytical solution and DEM results for a freely-falling particle using the Euler time-stepping method for varying restitution coefficients, and normal spring coefficient, $k_n = 10^5 \text{ N}\cdot\text{m}^{-1}$. (Left) Particle velocities; analytical solutions shown as continuous lines, MFIX-DEM results as points. (Right) Percent absolute relative error between the analytical and MFIX-DEM particle velocities.

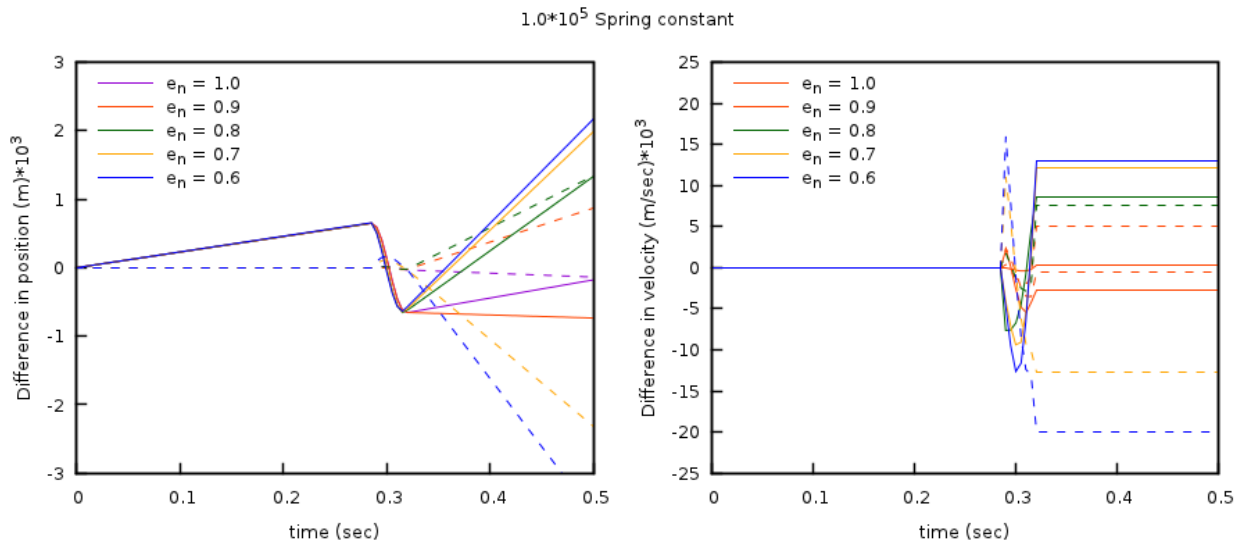


Fig. 6.4: Difference between analytical solution and MFIX-DEM results for a freely-falling particle with varying restitution coefficient and normal spring coefficient, $k_n = 10^5 \text{ N}\cdot\text{m}^{-1}$. Euler method shown as solid line. Adams-Bashforth method shown as dashed lines. (Left) Difference in particle position. (Right) Difference in particle velocity.

6.2 DEM02: Bouncing particle

This case provides a comparison between the MFiX-DEM linear spring-dashpot collision model and the *hard sphere* model where collisions are instantaneous. The hard sphere model can be seen as the limiting case where the normal spring coefficient is large, $k_n \rightarrow \infty$. This case was originally reported in [8].

6.2.1 Description

A smooth (frictionless), spherical particle falls freely under gravity from an initial height, h_0 , and bounces upon collision with a fixed wall Fig. 6.1. Assuming that the collision is instantaneous, the maximum height the particle reaches after the first collision (bounce), h_1^{\max} , is given by

$$h_1^{\max} = (h_0 - r_p) e_n^2 \quad (6.10)$$

where r_p is the particle radius, and e_n is the restitution coefficient. A general expression for the maximum height following the k^{th} bounce is

$$h_k^{\max} = (h_0 - r_p) e_n^{2k} + r_p. \quad (6.11)$$

6.2.2 Setup

Table 6.3: DEM-02 Setup, Initial and Boundary Conditions.

Computational/Physical model			
1D, Transient			
Granular flow (no gas)			
Gravity			
Thermal energy equation is not solved			
Geometry			
Coordinate system	Cartesian		
x-length	1.0	(m)	
y-length	1.0	(m)	
z-length	1.0	(m)	
Solids Properties			
Normal spring coefficient, k_n	<i>varied</i>	(N·m ⁻¹)	
Restitution coefficient, e_n	<i>varied</i>	()	
Friction coefficient, μ	0.0	()	
Solids 1 Type	DEM		
Diameter, d_p	0.2	(m)	
Density, ρ_s	2600	(kg·m ⁻³)	
Boundary Conditions			
All boundaries	Solid walls		

6.2.3 Results

Simulations of a freely-falling particle dropped from an initial height of 0.5m were conducted for three normal spring coefficients, $[0.5, 5.0, 50.0] \times 10^5 \text{ N}\cdot\text{m}^{-1}$, and six restitution coefficients, $[0.5, 0.6, 0.7, 0.8, 0.9, 1.0]$. All simulations employed the Adams-Bashforth time-stepping method. The maximum height attained after the k^{th} collision for all cases is shown in Fig. 6.5.

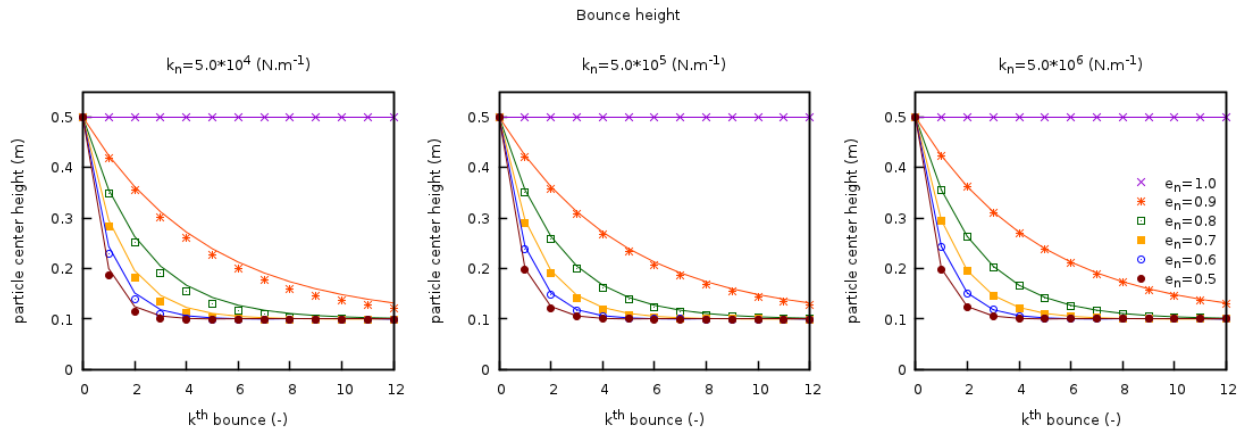


Fig. 6.5: Comparison between the analytic solution from a hard-sphere model (solid lines) and MFiX-DEM (symbols) of the maximum height reached after the k^{th} wall collision for a freely falling particle. Three values for the normal spring coefficient are used (left to right) with six restitution coefficients.

Fig. 6.6 illustrates the percent relative difference between the analytical solution for a hard-sphere model and the MFiX-DEM simulation. In the limit of the hard-sphere model (shown left to right by an increasing spring coefficient), the difference between the two collision models decreases.

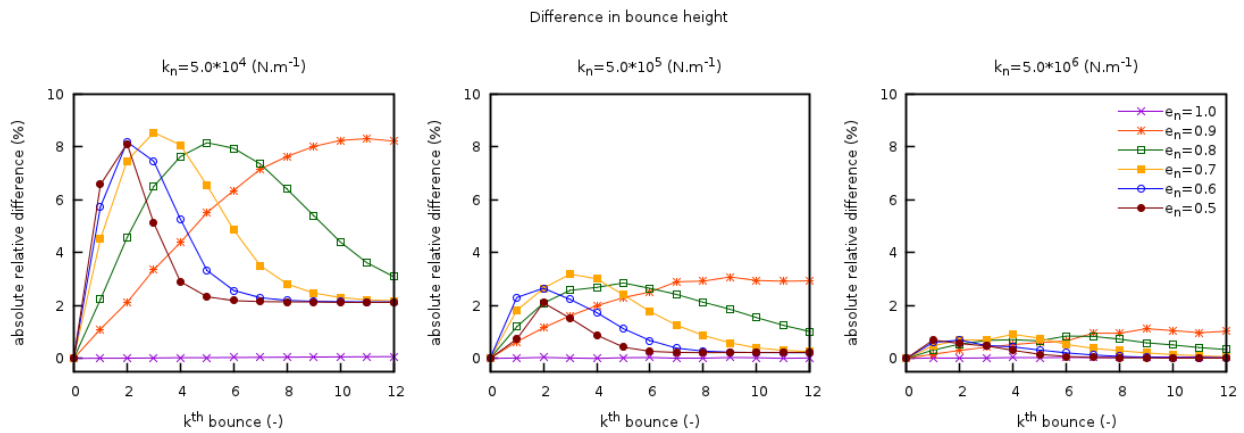


Fig. 6.6: Percent relative difference between the analytic solution for a hard-sphere model and MFiX-DEM of the maximum height reached after the k^{th} wall collision for a freely falling particle. Three values for the normal spring coefficient are used (left to right) with six restitution coefficients.

6.3 DEM03: Two stacked, compressed particles

This case serves to verify the MFiX-DEM linear spring-dashpot collision model through analysis of a multi-particle, enduring collision. This test case is based on the work of Chen et al. [4] and the MFiX-DEM test case was originally reported in Garg et al. [8].

6.3.1 Description

Two particles of equal radius, r_p , are stacked between two fixed walls such that the particles are compressed. The lower and upper walls are located at $y_l = 0.0$ and $y_w = 3.6r_p$ and the particle centers are initially located at $y_{10} = 0.25y_w$ and $y_{20} = 0.75y_w$. This configuration, illustrated in Fig. 6.7, ensures that the particles remain in contact and compressed.

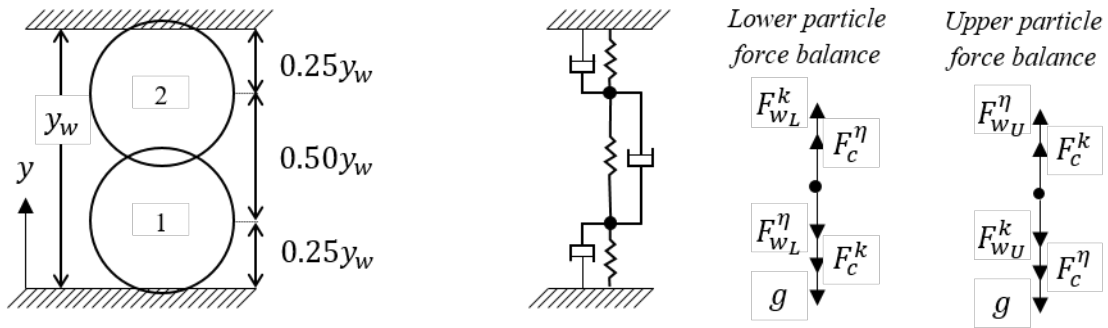


Fig. 6.7: Two smooth spherical particles stacked between two fixed walls so that the system is always under compression. A sketch of the problem mechanics is provided along with force balances for the lower and upper particles.

An expression for the acceleration of the lower particle (*particle 1*) is

$$\begin{aligned} \frac{d^2 y_1}{dt^2} = & -g - \frac{k_{nw}}{m_1} (y_1 - r_p) - \frac{\eta_{n1w}}{m_1} \frac{dy_1}{dt} \\ & - \frac{k_{n12}}{m_1} (2r_p - (y_2 - y_1)) - \frac{\eta_{n12}}{m_1} \left(\frac{dy_1}{dt} - \frac{dy_2}{dt} \right) \end{aligned} \quad (6.12)$$

where y_1 and y_2 are the particle center positions measured from the lower wall, g is the acceleration due to gravity, k_{nw} and k_{n12} are the particle-wall and particle-particle spring coefficients, η_{n1w} and η_{n12} are the particle-wall and particle-particle damping coefficients, and m_1 is the mass of particle 1. Similarly, acceleration of the upper particle (*particle 2*) is given by

$$\begin{aligned} \frac{d^2 y_2}{dt^2} = & -g - \frac{k_{nw}}{m_2} (r_p - (y_w - y_2)) - \frac{\eta_{n2w}}{m_2} \frac{dy_2}{dt} \\ & + \frac{k_{n12}}{m_2} (2r_p - (y_2 - y_1)) + \frac{\eta_{n12}}{m_2} \left(\frac{dy_1}{dt} - \frac{dy_2}{dt} \right) \end{aligned} \quad (6.13)$$

where η_{n2w} is the particle-wall damping coefficient for the upper particle, and m_2 is the mass of the upper particle.

6.3.2 Setup

Table 6.4: DEM-03 Setup, Initial and Boundary Conditions.

Computational/Physical model			
1D, Transient			
Granular flow (no gas)			
Gravity			
Thermal energy equation is not solved			
Geometry			
Coordinate system	Cartesian		
x-length	1.0	(m)	
y-length	0.0018	(m)	
z-length	0.0010	(m)	
Solids Properties			
Normal spring coefficient, k_n	10^3	(N·m ⁻¹)	
Restitution coefficient, e_n	<i>varied</i>	()	
Friction coefficient, μ	0.0	()	
Solids 1 Type	DEM		
Diameter, d_p	0.001	(m)	
Density, ρ_s	20000	(kg·m ⁻³)	
Solids 2 Type	DEM		
Diameter, d_p	0.001	(m)	
Density, ρ_s	10000	(kg·m ⁻³)	
Boundary Conditions			
All boundaries	Solid walls		

6.3.3 Results

Analytical solutions to equations Eq.6.12 and Eq.6.13 describing the motion of the particles are readily obtainable for perfectly elastic ($\eta_{n12} = \eta_{n1w} = \eta_{n2w} = 1.0$) particles of equal mass ($m_1 = m_2$). This is not the case for inelastic particles of different mass, therefore a fourth-order Runge-Kutta method is used to calculate a secondary numerical solution which is considered to be the analytical solution during the analysis.

Simulations were conducted for six friction coefficients, [0.5, 0.6, 0.7, 0.8, 0.9, 1.0], using the Adams-Bashforth time-stepping method. Fig. 6.8 shows the motion of the lower (left) and upper (right) particles as well as the absolute value of the relative error for a restitution coefficient of 1. The percent relative difference in results remains below 0.1% for this case. This is the largest observed difference across all cases with the difference in relative error decreasing with decreasing restitution coefficient.

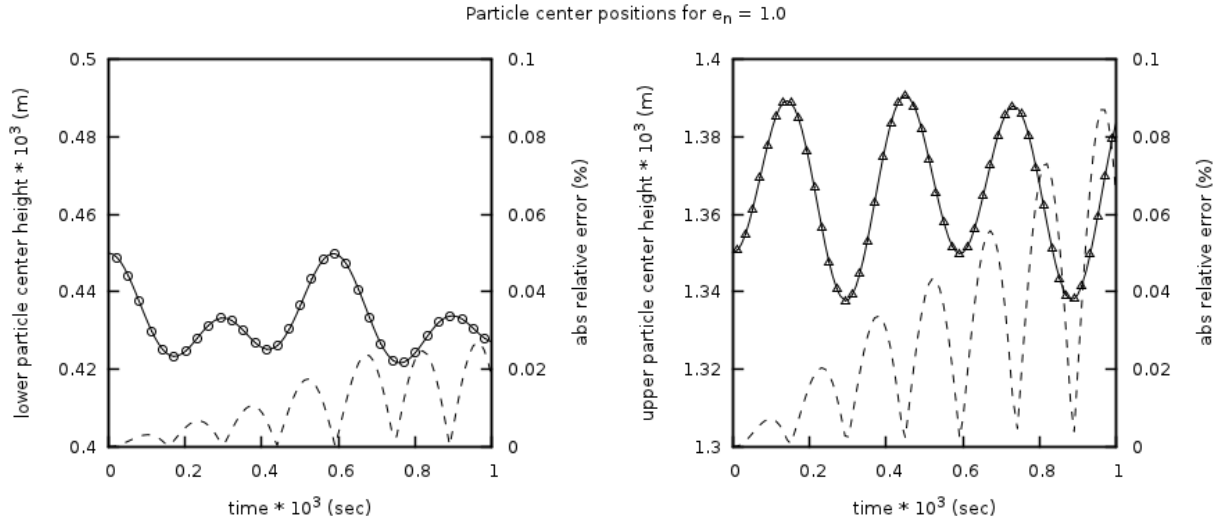


Fig. 6.8: Comparison between the fourth-order Runge-Kutta solution (solid line) and MFIX-DEM simulation (open symbols) for the center position of two stacked particles compressed between fixed walls for a restitution coefficient of 1. The absolute percent relative errors are shown as dashed lines.

6.4 DEM04: Slipping on a rough surface

This case serves to verify the MFIX-DEM soft-spring collision model through the analysis of the rolling friction model. This test case was originally reported in [8].

6.4.1 Description

A spherical particle of radius, r_p , finite translation velocity, u_0 , and zero angular velocity, ω_0 , is placed on a rough surface as illustrated in Fig. 6.9. The particle begins to roll while the translational velocity decreases because of rolling friction attributed to slip between the particle and the rough surface at the point of contact ($u \neq \omega r_p$). The rolling friction converts translation velocity to angular velocity until there is no slip at the contact point ($u = \omega r_p$). After the no-slip condition is reached, rolling friction ceases and the particle continues to move with constant translational and rotational velocities.

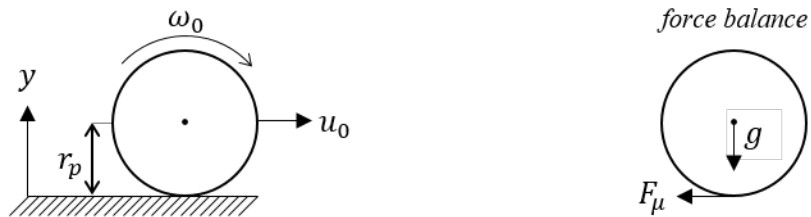


Fig. 6.9: A spherical particle with finite translational velocity and zero angular velocity is placed on a rough surface. Forces acting on the particle are indicated.

Kinetic friction is the only translational force acting on the particle and is given by

$$\frac{du}{dt} = \frac{d^2x}{dt^2} = -\mu g. \tag{6.14}$$

where g is the acceleration due to gravity, and μ is the coefficient of friction. Similarly, the angular velocity is given by

$$\frac{d\omega}{dt} = \frac{\mu g m r_p}{I} \quad (6.15)$$

where $I = 2mr_p^2/5$ and m are the particle moment of inertia and mass, respectively. Integrating equations (4-14) and (4-15) with initial conditions u_0 and ω_0 , an expression for the time when rolling friction ceases ($u = \omega r_p$) is obtained,

$$t_s = \frac{2u_0}{7\mu g} \quad (6.16)$$

6.4.2 Setup

Table 6.5: DEM-04 Setup, Initial and Boundary Conditions.

Computational/Physical model		
1D, Transient		
Granular flow (no gas)		
Gravity		
Thermal energy equation is not solved		
Geometry		
Coordinate system	Cartesian	
x-length	1.0	(m)
y-length	1.0	(m)
z-length	1.0	(m)
Solids Properties		
Normal spring coefficient, k_n	10^4	($\text{N}\cdot\text{m}^{-1}$)
Restitution coefficient, e_n	1.0	()
Friction coefficient, μ	<i>varied</i>	()
Solids 1 Type		
Diameter, d_p	0.001	(m)
Density, ρ_s	10,000	($\text{kg}\cdot\text{m}^{-3}$)
Boundary Conditions		
All boundaries	Solid walls	

6.4.3 Results

Simulations were conducted for nine restitution coefficients, [0.2, 0.3, 0.4, 0.4, 0.6, 0.7, 0.8, 0.9 1.0], using the Adams-Bashforth time-stepping method with the results shown in Fig. 6.10. The absolute relative percent error between the MFiX-DEM and analytical value for the non-dimensionalized time when rolling friction ceases, $t_s / (\mu g / u_0)$, is less than 1% for all reported conditions. Similarly, the absolute relative percent error between the MFiX-DEM and analytical value for the non-dimensionalized tangential and angular velocities is less than 0.1% for all reported conditions. Error between the MFiX-DEM and analytical values can be further reduced (not shown) by increasing the normal spring coefficient, k_n , which decreases the DEM solids time-step size.

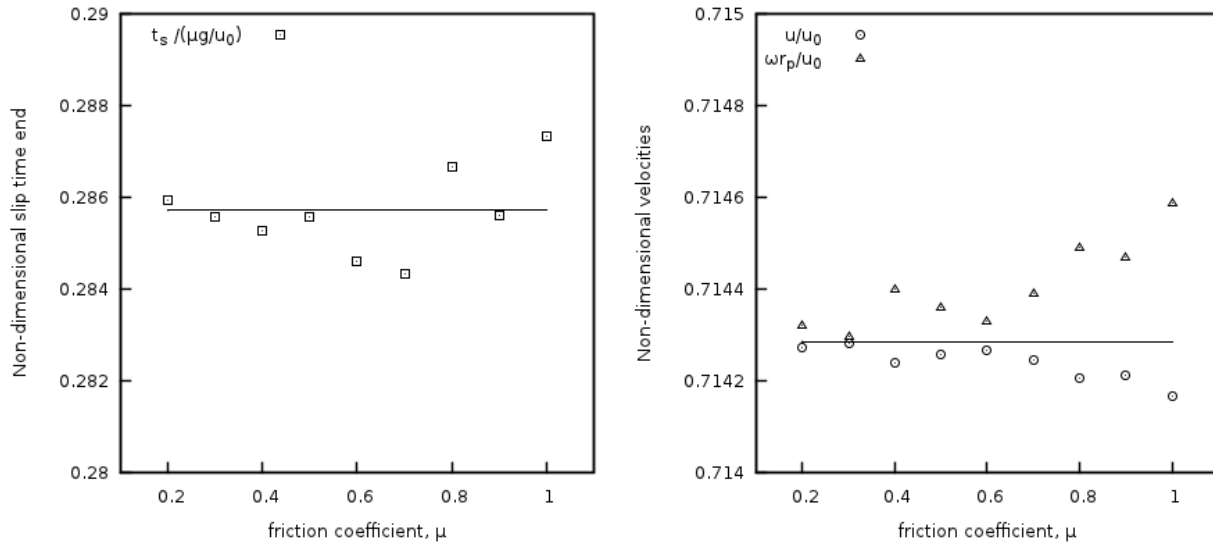


Fig. 6.10: Comparison between the analytical solution (solid line) and MFIX-DEM simulation (open symbols) of a particle with radius r_p slipping on a rough surface for various friction coefficients. (left) Dimensionless slip time end and (right) dimensionless equilibrium tangential, u , and angular, ω , velocities.

6.5 DEM05: Oblique particle collision

This case serves to verify the normal and tangential components of both the linear spring-dashpot and Hertzian collision models in MFIX DEM. This case is based on the modeling work of Di Renzo and Di Maio [20] and utilizes the experimental data of Kharaz, Gorham, and Salman [13].

6.5.1 Description

In the experiments of Kharaz, Gorham, and Salman [13], a spherical particle is dropped from a fixed height such that it collides with a rigid surface at a known velocity. The angle of the ridged surface is varied to test impact angles ranging from normal to glancing. The rebound angle, post-collision angular velocity, and observed tangential restitution coefficient were reported.

In the experiment, the particle strikes an angled anvil as illustrated in Fig. 6.11 (a). Rather than modeling an angled surface, the wall is kept level (flat) and the particle is given an initial trajectory corresponding to the angle found in the experiment as shown in Fig. 6.11 (b). The particle is initially positioned close to the wall and gravity is suppressed in the simulations to eliminate the effects of the rotated geometry with respect to the experimental apparatus.

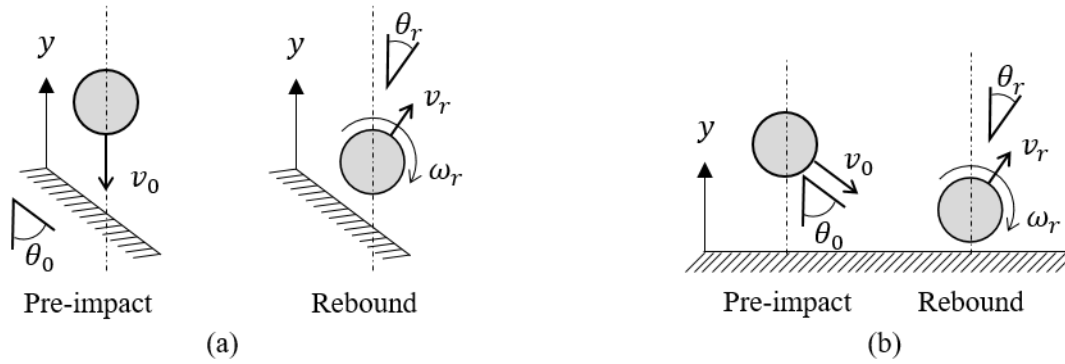


Fig. 6.11: Experimental setup of Kharaz, Gorham, and Salman [13] of a particle striking a fixed, angled anvil. (b) Simulation setup whereby the particle is given an initial velocity to replicate the particle striking an angled surface.

6.5.2 Setup

Table 6.6: DEM-05 Setup, Initial and Boundary Conditions.

Computational/Physical model			
1D, Transient			
Granular flow (no gas)			
Gravity			
Thermal energy equation is not solved			
Geometry			
Coordinate system	Cartesian		
x-length	0.5	(m)	
y-length	0.1	(m)	
z-length	0.5	(m)	
Solids Phase 1	DEM		
Diameter, d_p	0.005	(m)	
Density, ρ_s	4,000	($\text{kg}\cdot\text{m}^{-3}$)	
Solids Phase 2	DEM		
Diameter, d_p	0.005	(m)	
Density, ρ_s	5,000	($\text{kg}\cdot\text{m}^{-3}$)	
Boundary Conditions			
All boundaries	Solid walls		

The mechanical properties for the particle (solids phase 1) and the anvil (solids phase 2 and wall) are provided for both the linear spring-dashpot and Hertzian collision models. The second solids phase is given the same properties as the anvil for verification of both the particle-particle and particle-wall collision model implementations.

Table 6.7: Mechanical properties for particle and anvil.

	Linear	Hertzian
Solids Phase 1		
Normal spring coefficient, (N·m ⁻¹)	1.72 x 10 ⁷	–
Restitution coefficient, (N·m ⁻¹)	1.0	–
Young’s modulus		380 x 10 ⁹
Poisson ratio	–	0.23
Friction coefficient	0.092	0.092
Solids Phase 2		
Normal spring coefficient, (N·m ⁻¹)	1.72 x 10 ⁷	–
Restitution coefficient, (N·m ⁻¹)	1.0	–
Young’s modulus		70 x 10 ⁹
Poisson ratio	–	0.25
Friction coefficient	0.092	0.092

6.5.3 Results

Simulations were conducted using the linear spring-dashpot and Hertzian collision models. Each simulation contained a total of 93 particles. The particle-particle and particle-wall collision models were tested by varying the initial collision angles between 0 (normal) and 65 degrees (glancing). Gravity was suppressed in the simulations to eliminate the effects of the rotated geometry with respect to the experimental apparatus.

The rebound angle, observed tangential restitution coefficient, and post-collision angular velocity for particle-wall collisions are given in Fig. 6.12 with particle-particle collision results shown in Fig. 6.13. There is good agreement between the simulation results and experimental data for the rebound angle and post-collision angular velocity. Although both models over predict the observed tangential coefficient for steep (near-normal) collision angles, better agreement is observed with the linear spring-dashpot model for the parameters used.

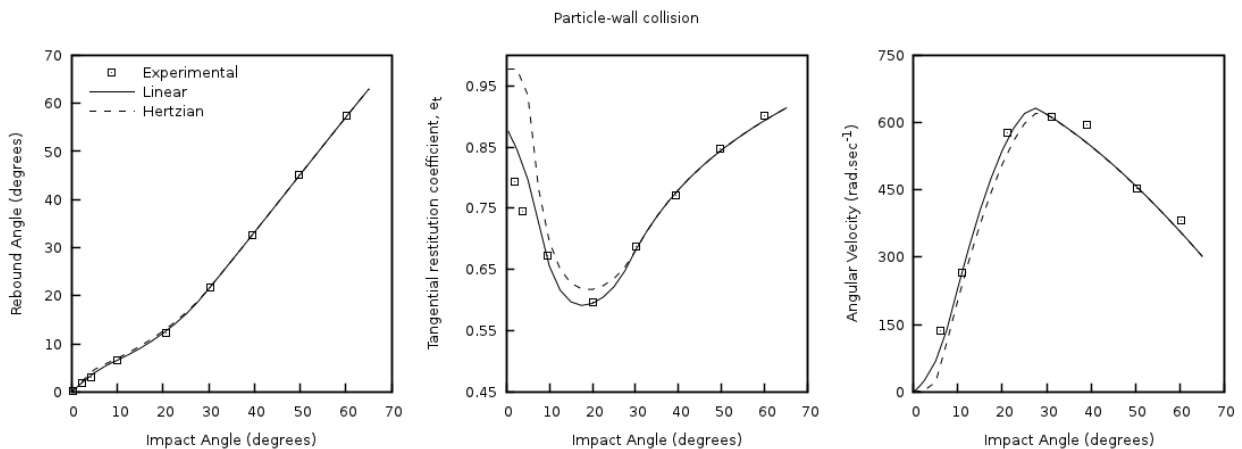


Fig. 6.12: Particle-wall oblique collision results for the linear spring-dashpot model (solid line), Hertzian model (dashed line), and experimental data (symbols) of Kharaz, Gorham, and Salman [13].

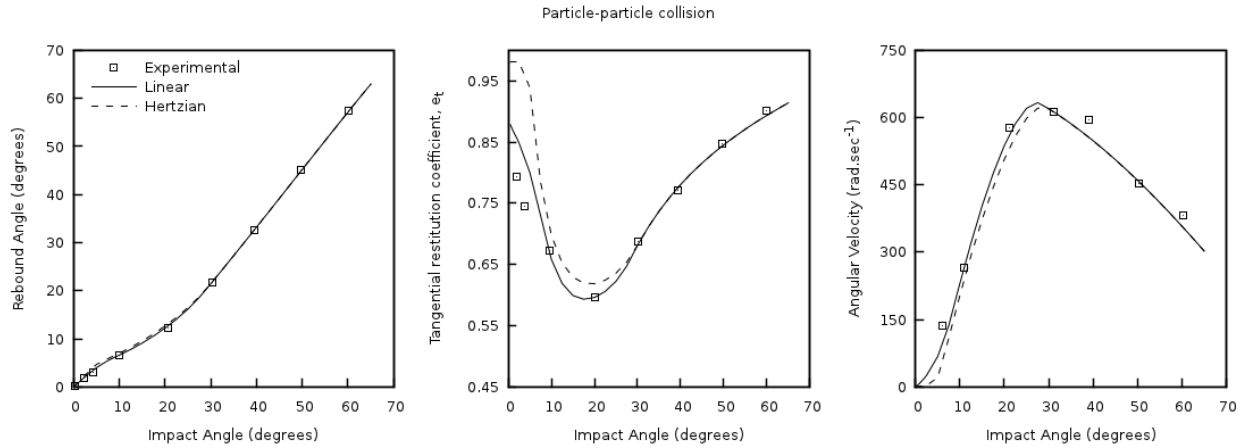


Fig. 6.13: Particle-particle oblique collision results for the linear spring-dashpot model (solid line), Hertzian model (dashed line), and experimental data (symbols) of Kharaz, Gorham, and Salman [13].

6.6 DEM06: Single particle, terminal velocity

This case investigates the interphase coupling of momentum equations through the gas-solids drag force. The original case was reported in [8] and has been expanded to test additional coupling schemes.

6.6.1 Description

A single particle initially at rest is released in a uniform gas stream as illustrated in Fig. 6.14 where the gravitational and gas-solids drag forces are the dominant forces acting on the particle. The velocity of the particle increases until it reaches its *terminal velocity* where the gravitational force is equal to the gas-solids drag force.

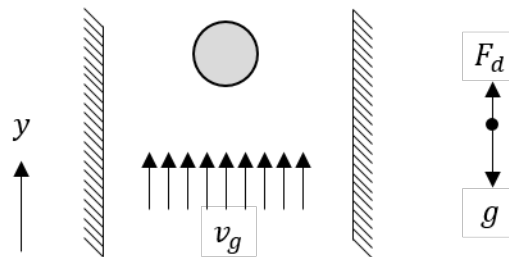


Fig. 6.14: A single spherical particle initially at rest is released in a uniform, vertical air flow. The dominant forces acting on the particle are the gas-solids drag force, F_d , and the gravitational force, g .

For a sufficiently small particle, the evolution of the particle velocity is given by

$$\frac{d^2y}{dt^2} = \frac{dv_p}{dt} = \frac{g(\rho_p - \rho_g)}{\rho_p} - \frac{3}{4} \frac{\rho_g \|v_p - v_g\|_2}{d_p \rho_p} C_d; \quad (6.17)$$

$$y(0) = h_0; \quad \frac{dy}{dt}(0) = 0$$

where y is the particle center position measured from the bottom wall, v_p and v_g are the particle and gas velocities, ρ_p and ρ_g are the particle and gas densities, d_p is the particle diameter, h_0 is the initial height of the particle, g is the acceleration due to gravity, and C_d is the drag coefficient. The drag coefficient is estimated here using the Schiller and Naumann [27]

correlation for a single particle in an unbounded medium,

$$C_d = \frac{24}{N_{\text{Re}}} (1 + 0.15 N_{\text{Re}}^{0.687}) \quad (6.18)$$

where N_{Re} is the Reynolds number based on the slip velocity between the particle and gas defined as

$$N_{\text{Re}} = \frac{\rho_g \|v_p - v_g\|_2 d_p}{\mu_g}. \quad (6.19)$$

6.6.2 Setup

Table 6.8: DEM-06 Setup, Initial and Boundary Conditions.

Computational/Physical model			
1D, Transient			
Multiphase flow (gas-solids)			
Gravity			
Thermal energy equation is not solved			
Geometry			
Coordinate system	Cartesian		
x-length	0.01	(m)	
y-length	0.10	(m)	
z-length	0.01	(m)	
Solids Properties			
Normal spring coefficient, k_n	10^{-1}	($\text{N}\cdot\text{m}^{-1}$)	
Restitution coefficient, e_n	1.0	()	
Friction coefficient, μ	0.0	()	
Solids 1 Type	DEM		
Diameter, d_p	10^{-4}	(m)	
Density, ρ_s	2,000	($\text{kg}\cdot\text{m}^{-3}$)	
Boundary Conditions			
South face (XZ-plane; $y=0.00\text{m}$)	Gas Mass Inflow		
<i>Pressure (gauge)</i>	0.00	(Pa)	
<i>Gas velocity, v_g</i>	0.40	($\text{m}\cdot\text{s}^{-1}$)	
North face (XZ-plane; $y=0.10\text{m}$)	Pressure Outflow		
<i>Pressure (gauge)</i>	0.00	(Pa)	
All other boundaries	Free-slip walls		

6.6.3 Results

A fourth-order Runge-Kutta method was used to calculate the solution to Eq.6.17 which was subsequently compared with the solutions of the seven MFIX-DEM simulations outlined below. The first set of simulations were one-way coupled such that only the gas phase volume fraction was affected by the presence of the particle. Specifically, gas-solids drag force was omitted from the gas phase momentum equations. This case best captured the above problem description where a single particle is freely falling through a uniform gas field. In the second group of tests the gas and solids were fully coupled. Three interpolation methods were used with both the one-way and fully coupled tests.

Table 6.9: Gas-solid interpolation.

Interpolation Scheme	Coupling	Filter size
Centroid	one-way	–
Garg_2012	one-way	–
DPVM_Square	one-way	2.0×10^{-3}
Centroid	full	–
Garg_2012	full	–
DPVM_Square	full	3.0×10^{-3}
DPVM_Square	full	4.0×10^{-3}

Fig. 6.15 illustrates a typical comparison of analytical particle velocity evolution over time obtained by Eq.6.17 and the numerical solution. A comparison of the absolute percent relative difference between the solutions is shown in Fig. 6.16. The numerical solution from simulations employing one-way coupling (left) compare well with the analytical solution of Eq.6.17 with the maximum absolute relative difference bounded above by 5×10^{-3} percent for the three cases. Additionally, the maximum absolute relative difference for cases with full coupling is bounded from above by 5 percent.

The large difference in results for the fully coupled cases should not be interpreted as error because the assumption of a uniform gas velocity used to establish Eq.6.17 is no longer valid when the gas-solids drag is allowed to affect the gas velocity as is the case in the fully coupled simulations. The suitability of this assumption, or lack thereof, is apparent from inspecting the results from different coupling schemes. The centroid method concentrates the gas-solids drag force in the fluid cell containing the particle center. As a result, gas velocity is impacted the most when compared to the other methods available. The divided particle volume method (DVPM) diffuses the gas-solids drag force over an area based on the filter width providing better agreement. Finally, the GARG_2012 scheme shows the best agreement as it diffuses the gas-solids drag force over the greatest area thereby providing greater consistency with the uniform flow field assumption.

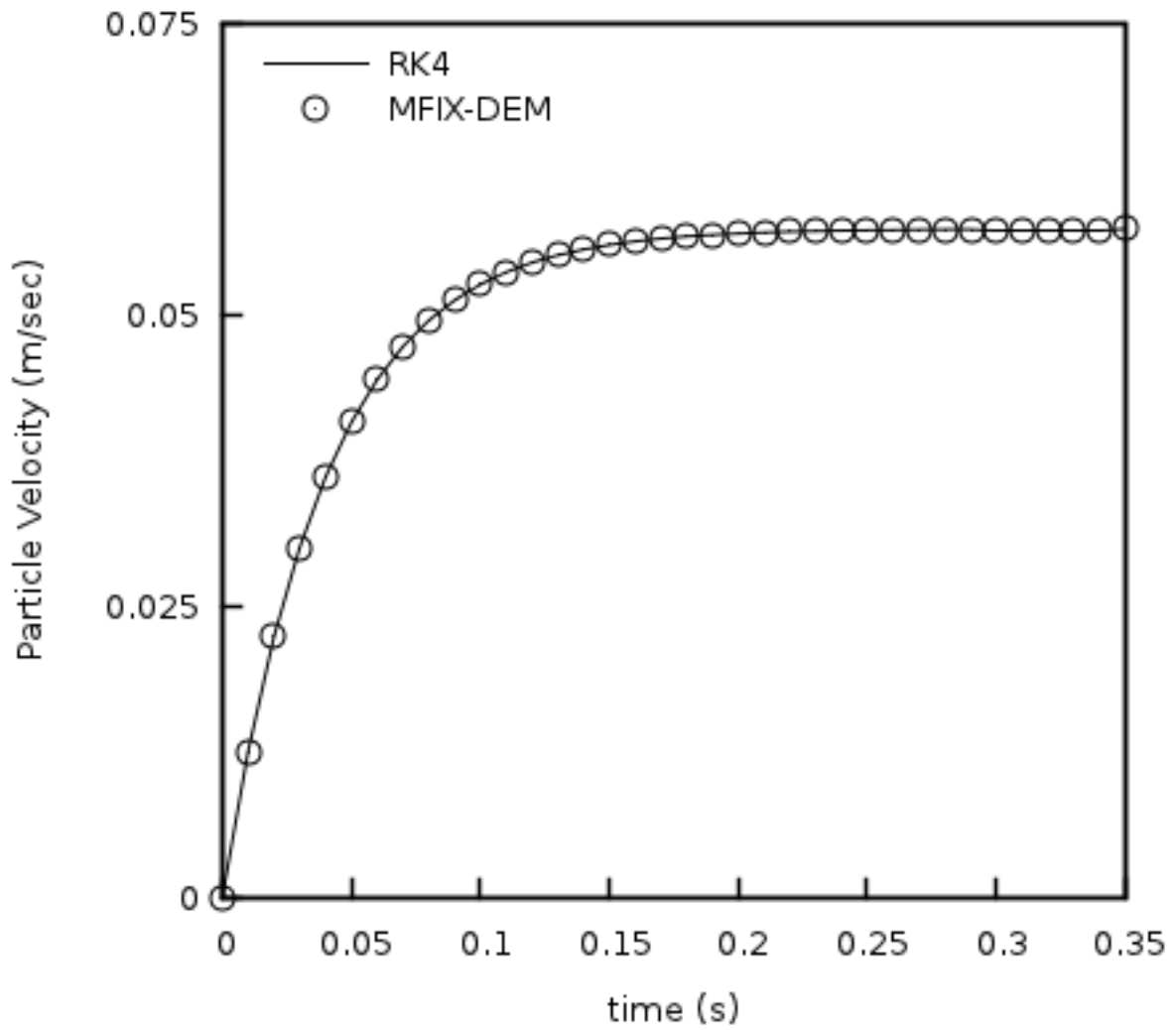


Fig. 6.15: Comparison of the particle velocity evolution obtained by Eq.6.17 and MFiX-DEM.

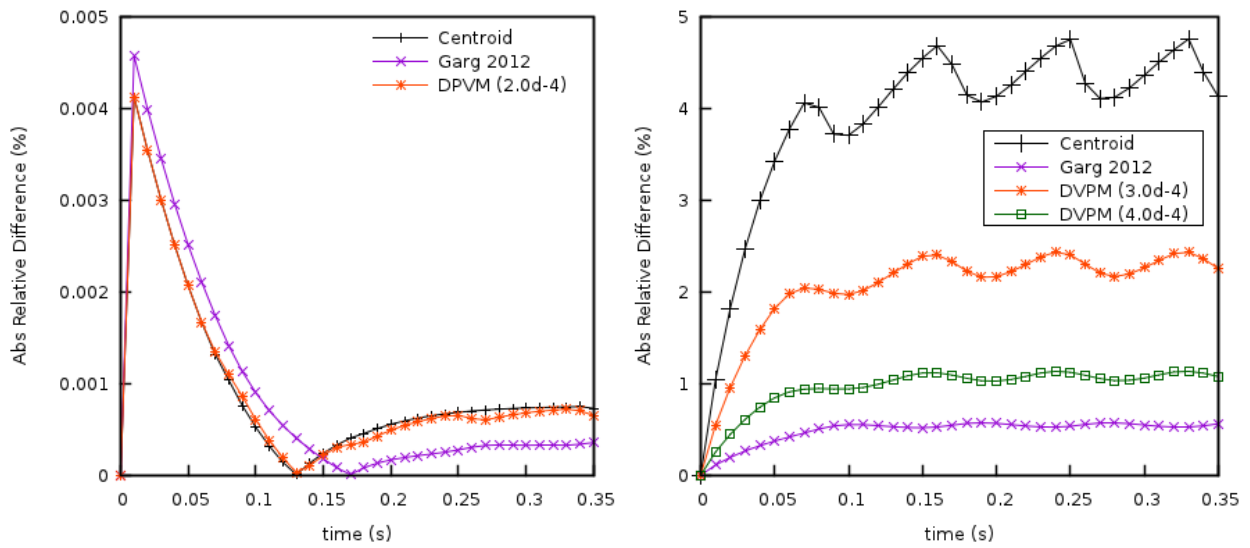


Fig. 6.16: Absolute percent relative difference between particle velocity evolution obtained by Eq.6.17 and MFIX-DEM. (left) Simulations with one-way gas-solids coupling. (right) Fully coupled simulations.

MFiX-PIC CODE VERIFICATION TEST CASES

The contents in this section are derived from the TRS report on MFiX-PIC V&V [32] published in 2020. The test cases presented in this chapter are summarized in Table 7.1. Under verification (PIC01-PIC05), the results from MFiX-PIC are compared with exact or analytical solutions, while experimental results are used for benchmarking under validation (PIC06 and PIC07).

Table 7.1: Summary of MFiX-DEM tests by feature.

	01	02	03	04	05	06	07
Frequency†	C	C	C	C	C	C	C
Reference Dataset‡	A	A	A	A	A	P	P
Dimension	3D						
Coupled		✓	✓	✓		✓	✓
Momentum	✓	✓	✓	✓		✓	✓
Thermal Energy					✓		
Particle Mass					✓		
Species Mass					✓		
Distributed Memory						✓	
Shared Memory							

† C-Incorporated into the continuous integration server; M-Monthly; Q-Quarterly; X-Manual; D-Disabled

‡ A-Analytical solution; P-Published benchmark data; R-Regression data from previous code versions

7.1 PIC01: Terminal velocity

7.1.1 Description

This case is similar to “DEM06: Single particle, terminal velocity”. A computational parcel containing physical particles is subjected to a uniform gas velocity. The statistical weight and initial gas volume fraction are adjusted such that all particles are accommodated in one parcel for the given grid resolution. The simulation results are compared with the analytical results obtained by solving the following system of Ordinary Differential Equations:

$$\frac{d^2y}{dt^2} = \frac{dv_p}{dt} = \frac{g(\rho_p - \rho_g)}{\rho_p} - \frac{3}{4}C_d \frac{\rho_g |v_p - v_g|^2}{\rho_p d_p} \quad (7.1)$$

The initial and boundary conditions are given by,

$$y(0) = h_0; \quad \frac{dy}{dt}(0) = 0 \quad (7.2)$$

where, y is the position of particle center measured from the bottom wall, v_p and v_g are the particle and gas velocities, ρ_p and ρ_g are particle and gas densities, d_p is the particle diameter, h_0 is the initial height of the particle, g is the acceleration due to gravity, and C_d is the drag coefficient. In this case, $C_d = 1$ is used for simplicity. The effect of the parcel on the gas phase is neglected since particle concentration is extremely dilute. Hence, the momentum equations for the gas-phase are not solved.

7.1.2 Setup

Table 7.2: PIC-01 Setup, Initial and Boundary Conditions.

Computational/Physical model			
3D, Transient			
Multiphase			
Gravity			
Thermal energy equation is not solved			
Turbulence equations are not solved (Laminar)			
Uniform mesh			
First order upwind discretization scheme			
Geometry			
Coordinate system	Cartesian		Grid partitions
x-length	0.01	(m)	5
y-length	0.30	(m)	60
z-length	0.01	(m)	5
Material			
Gas density, ρ_g	1.2	($\text{kg}\cdot\text{m}^{-3}$)	
Gas viscosity, μ_g	1.8E-05	(Pa·s)	
Solids Type	PIC		
Diameter, d_p	0.1	(m)	
Density, ρ_s	2000	($\text{kg}\cdot\text{m}^{-3}$)	
Solids Properties (PIC)			
Pressure linear scale factor, P_s	100.0	(Pa)	
Exponential scale factor, γ	3.0	(-)	
Statistical weight	100	(-)	
Initial Conditions			
x-velocity, u_g	0.0	($\text{m}\cdot\text{s}^{-1}$)	
y-velocity, v_g	0.4	($\text{m}\cdot\text{s}^{-1}$)	
z-velocity, w_g	0.0	($\text{m}\cdot\text{s}^{-1}$)	
Solids concentration, ϵ_s	0.0001	(-)	
Gas volume fraction at packing, ϵ_g^*	0.4	(-)	
Pressure, P_g	101,325	(Pa)	
Boundary Conditions			
South	0.4	($\text{m}\cdot\text{s}^{-1}$)	Mass inflow
North	101,325	(Pa)	Pressure outflow
West, east, top and bottom			Free-Slip wall

7.1.3 Results

As the parcel falls, its velocity increases initially, and reaches its terminal velocity when the gravitational force is balanced by the drag force. The numerical solution to the system of equations is obtained using 4th order Runge-Kutta method. The values are compared with the MFiX-PIC simulations as shown in Fig. 7.1. The velocity and position are accurately predicted by MFiX-PIC as was the case with MFiX-DEM.

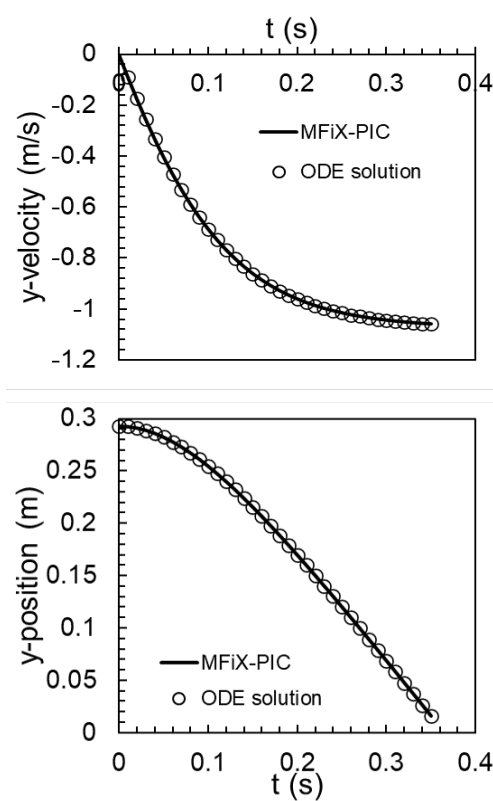


Fig. 7.1: Predictions using MFiX-PIC: velocity (top) and position (bottom).

7.2 PIC02: Advection in time varying flow field – velocity interpolation

7.2.1 Description

This is a code verification problem discussed in the DEM documentation of Garg et al. [8]. A total of 512 parcels are arranged on a sphere having a radius of 0.15 m centered at (0.35 m, 0.35 m, 0.35 m). The domain under consideration is a unit box (1.0 m X 1.0 m X 1.0 m) discretized uniformly having 32 cells in each direction. A time varying flow-field is prescribed as follows:

$$\begin{aligned}
 u_g &= 2\sin^2(\pi x)\sin(2\pi y)\sin(2\pi z)\cos\left(\frac{\pi t}{T}\right) \\
 v_g &= -\sin(2\pi x)\sin^2(\pi y)\sin(2\pi z)\cos\left(\frac{\pi t}{T}\right) \\
 w_g &= -\sin(2\pi x)\sin(2\pi y)\sin^2(\pi z)\cos\left(\frac{\pi t}{T}\right)
 \end{aligned}
 \tag{7.3}$$

7.2.2 Setup

Table 7.3: PIC-02 Setup, Initial and Boundary Conditions.

Computational/Physical model			
3D, Transient			
Multiphase			
Gravity			
Thermal energy equation is not solved			
Turbulence equations are not solved (Laminar)			
Uniform mesh			
First order upwind discretization scheme			
Geometry			
Coordinate system	Cartesian		Grid partitions
x-length	1.0	(m)	32
y-length	1.0	(m)	32
z-length	1.0	(m)	32
Material			
Gas density, ρ_g	1.2	($\text{kg}\cdot\text{m}^{-3}$)	
Gas viscosity, μ_g	1.8E-05	(Pa·s)	
Solids Type			
	PIC		
Diameter, d_p	0.01	(m)	
Density, ρ_s	2700	($\text{kg}\cdot\text{m}^{-3}$)	
Solids Properties (PIC)			
Pressure linear scale factor, P_s	100.0	(Pa)	
Exponential scale factor, γ	3.0	(-)	
Statistical weight	1	(-)	
Initial Conditions			
x-velocity, u_g	Eq.7.3	($\text{m}\cdot\text{s}^{-1}$)	
y-velocity, v_g	Eq.7.3	($\text{m}\cdot\text{s}^{-1}$)	
z-velocity, w_g	Eq.7.3	($\text{m}\cdot\text{s}^{-1}$)	
Gas volume fraction, ϵ_g	1.0	(-)	
Gas volume fraction at packing, ϵ_g^*	0.4	(-)	
Pressure, P_g	101,325	(Pa)	
Boundary Conditions			
All boundaries are cyclic			

A value of 0.25 is chosen for the time period T and the simulations are run for a total duration of 4 seconds which is equivalent to 16 cycles. The initial parcel configuration and velocities are specified through a particle_input.dat file, typical of MFiX runs that require an exact particle arrangement.

7.2.3 Results

The parcels are sheared in different directions since the center of the spherical arrangement is off from the center of the vortex field. Once the simulation begins, the configuration is deformed and then restored at multiples of time period T as shown in Fig. 7.2. The absolute difference between the exact location and the numerical solution is shown in Table 7.4. The maximum locational error is still within 0.01 m at the end of 16 cycles.

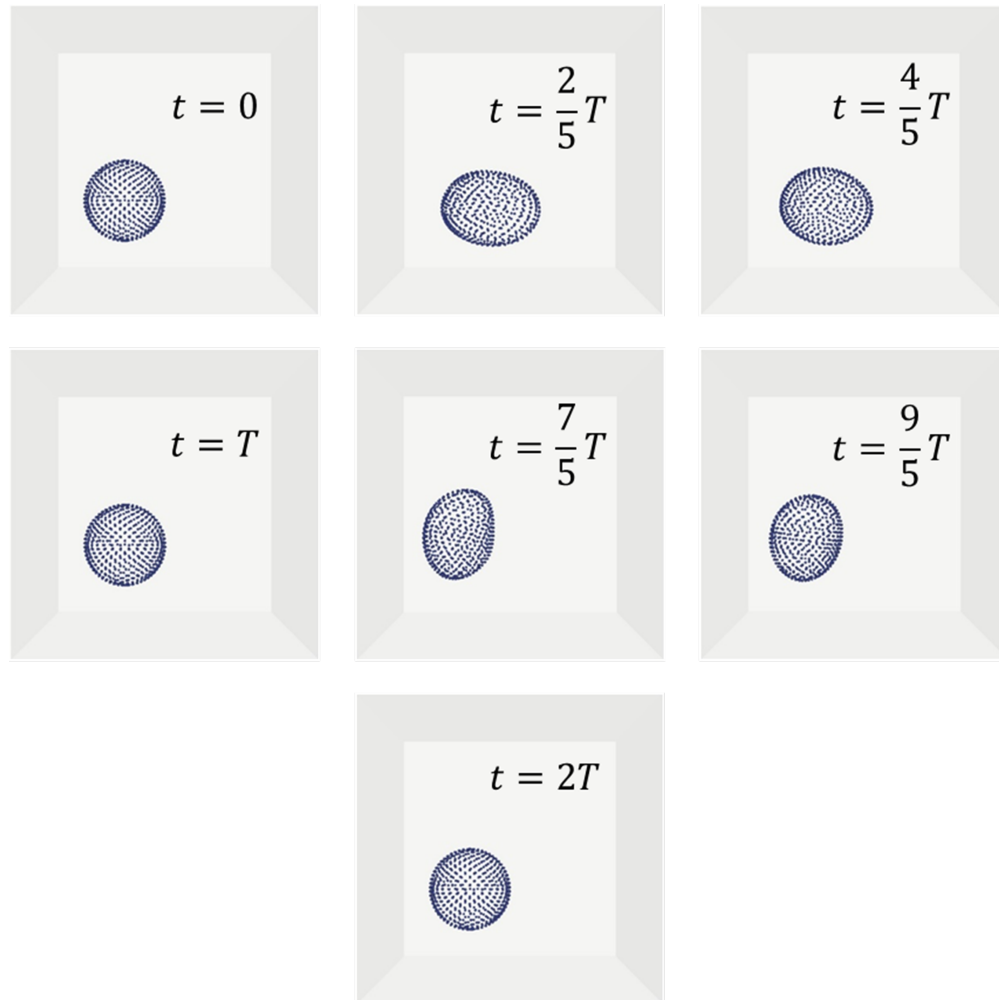


Fig. 7.2: Instantaneous location of parcels for the configuration centered at $X=0.35$ m, $Y=0.35$ m, $Z=0.35$ m. The time stamps are provided inside each snapshot.

Table 7.4: L1-Norms of Parcel Displacement for the Configuration Centered at (0.35 m, 0.35 m, 0.35 m) having a Radius of 0.15 m.

Physical Time (s)	Cycle	Maximum L1-Norm (m)
0.25	1	2.11E-03
0.50	2	1.22E-03
0.75	3	2.59E-03
1.00	4	2.44E-03
1.25	5	3.46E-03
1.50	6	3.65E-03
1.75	7	4.49E-03
2.00	8	4.87E-03
2.25	9	5.60E-03
2.50	10	6.08E-03
2.75	11	6.74E-03
3.00	12	7.29E-03
3.25	13	7.90E-03
3.50	14	8.51E-03
3.75	15	9.08E-03
4.00	16	9.72E-03

7.3 PIC03: Advection in time varying flow field – parcel volume deposition

7.3.1 Description

In this case the arrangement of 480 parcels having a radius of 0.15 m centered at the origin is considered. The objective is to test the following:

1. Periodic boundaries
2. Parcel volume deposition on Eulerian cells

The time varying flow-field is prescribed using Eq.7.3, where the time period T is 0.25 seconds. The domain under consideration and its discretization are identical to the set-up described in Section 2.2.1. The initial parcel configuration is specified through a particle_input.dat file.

7.3.2 Setup

Table 7.5: PIC-02 Setup, Initial and Boundary Conditions.

Computational/Physical model			
3D, Transient			
Multiphase			
Gravity			
Thermal energy equation is not solved			
Turbulence equations are not solved (Laminar)			
Uniform mesh			
First order upwind discretization scheme			

continues on next page

Table 7.5 – continued from previous page

Computational/Physical model			
Geometry			
Coordinate system	Cartesian		Grid partitions
x-length	1.0	(m)	32
y-length	1.0	(m)	32
z-length	1.0	(m)	32
Material			
Gas density, ρ_g	1.2	($\text{kg}\cdot\text{m}^{-3}$)	
Gas viscosity, μ_g	1.8E-05	(Pa·s)	
Solids Type	PIC		
Diameter, d_p	0.01	(m)	
Density, ρ_s	2700	($\text{kg}\cdot\text{m}^{-3}$)	
Solids Properties (PIC)			
Pressure linear scale factor, P_s	100.0	(Pa)	
Exponential scale factor, γ	3.0	(-)	
Statistical weight	1	(-)	
Initial Conditions			
x-velocity, u_g	Eq.7.3	($\text{m}\cdot\text{s}^{-1}$)	
y-velocity, v_g	Eq.7.3	($\text{m}\cdot\text{s}^{-1}$)	
z-velocity, w_g	Eq.7.3	($\text{m}\cdot\text{s}^{-1}$)	
Gas volume fraction, ϵ_g	1.0	(-)	
Gas volume fraction at packing, ϵ_g^*	0.4	(-)	
Pressure, P_g	101,325	(Pa)	
Boundary Conditions			
All boundaries are cyclic			

A value of 0.25 is chosen for the time period T and the simulations are run for a total duration of 4 seconds which is equivalent to 16 cycles. The initial parcel configuration and velocities are specified through a particle_input.dat file, typical of MFiX runs that require an exact particle arrangement.

7.3.3 Results

Once the simulation begins, parcels move in all possible directions and across the periodic boundaries as shown in Fig. 7.3. The volume conservation is examined by comparing the volume fractions of fluid and solid during the simulation as given in Table 7.6. The volume fraction of fluid is calculated by the code, based on interpolation of solid volumes on to the Eulerian cells and the volume fraction of solids is calculated using the particle count. It can be seen that fluid and solid volume fractions (ϵ_g, ϵ_s) do sum to 1 (very close to machine precision). This is indicated by the negligible relative error of the sum of phasic volume fractions in Table 7.6. Hence, this study concluded that the implementation of routines pertaining to periodicity and parcel-fluid interpolation are verified.

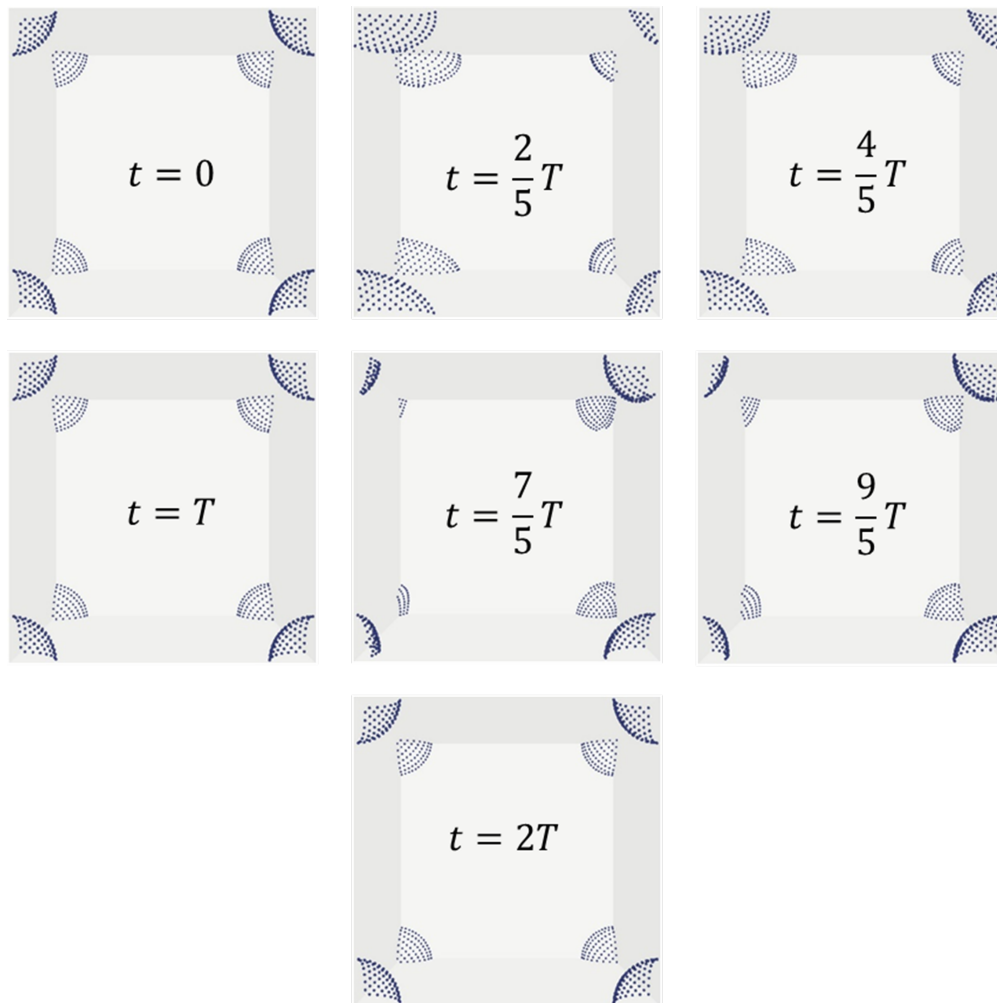


Fig. 7.3: Instantaneous location of parcels for the configuration centered at X=0 m, Y=0 m, Z=0 m. Time stamps are provided inside each snapshot.

Table 7.6: Absolute Error in Total Volume Fraction for the Configuration Centered at (0m, 0m, 0m).

Physical Time (s)	Cycle	ϵ_s	ϵ_g	Absolute Error
0.25	1	2.51E-04	9.997487E-01	6.66E-16
0.50	2	2.51E-04	9.997487E-01	8.88E-16
0.75	3	2.51E-04	9.997487E-01	3.33E-16
1.00	4	2.51E-04	9.997487E-01	8.88E-16
1.25	5	2.51E-04	9.997487E-01	4.44E-16
1.50	6	2.51E-04	9.997487E-01	1.33E-15
1.75	7	2.51E-04	9.997487E-01	8.88E-16
2.00	8	2.51E-04	9.997487E-01	0
2.25	9	2.51E-04	9.997487E-01	1.67E-15
2.50	10	2.51E-04	9.997487E-01	4.44E-16
2.75	11	2.51E-04	9.997487E-01	2.22E-16
3.00	12	2.51E-04	9.997487E-01	0
3.25	13	2.51E-04	9.997487E-01	4.44E-16
3.50	14	2.51E-04	9.997487E-01	1.11E-15
3.75	15	2.51E-04	9.997487E-01	1.11E-15
4.00	16	2.51E-04	9.997487E-01	6.66E-16

7.4 PIC04: Particle-Settling in Fluid

7.4.1 Description

MFiX-TFM, MFiX-DEM and MFiX-PIC are used to simulate the problem of particle settling. Spatial locations of concentration fronts at time $t = 1$ seconds are compared with the analytical expression given by,

$$x(t) = x_0 + tu_{shock} \quad (7.4)$$

The velocity of propagation of the shock wave (derived in Appendix B) is given by,

$$u_{shock} = - \left(j + \frac{(\epsilon_s \epsilon_g u_r)_B - (\epsilon_s \epsilon_g u_r)_A}{\epsilon_{sB} - \epsilon_{sA}} \right) \quad (7.5)$$

where the subscripts A and B denote the regions on either side of the shock as shown in Fig. 9.2. The volumetric flux is 0 in the case of settling. Also, the particle volume fraction in region A is 0 for the shock front traveling downwards. Hence the location of the shock is given by,

$$x(t) = x_0 - t(\epsilon_{g0} u_{r0}) \quad (7.6)$$

where, ϵ_{g0} is the initial gas volume fraction. The relative velocity using the Stokes drag law is given by,

$$u_{r0} = \frac{g \Delta \rho d_p^2}{18 \mu_g} \epsilon_{g0}^{3.65} \quad (7.7)$$

The location of the shock front corresponding to filling is given by,

$$x(t) = -t \left(\frac{(\epsilon_s^* \epsilon_g^* u_r^*) - (\epsilon_{s0} \epsilon_{g0} u_{r0})_A}{\epsilon_s^* - \epsilon_{s0}} \right) \quad (7.8)$$

7.4.2 Setup

Table 7.7: PIC-04 Setup, Initial and Boundary Conditions.

Computational/Physical model			
3D, Transient			
Multiphase			
Gravity			
Thermal energy equation is not solved			
Turbulence equations are not solved (Laminar)			
Uniform mesh			
First order upwind discretization scheme			
Geometry			
Coordinate system	Cartesian		Grid partitions
x-length	0.02	(m)	5
y-length	1.0	(m)	100
z-length	0.02	(m)	5
Material			
Gas density, ρ_g	1000.0	($\text{kg}\cdot\text{m}^{-3}$)	
Gas viscosity, μ_g	0.001	(Pa·s)	
Solids Type	PIC,DEM,TFM		
Diameter, d_p	0.01	(m)	
Density, ρ_s	2700	($\text{kg}\cdot\text{m}^{-3}$)	
Solids Properties (PIC)			
Pressure linear scale factor, P_s	10.0	(Pa)	
Exponential scale factor, γ	3.0	(-)	
Statistical weight	5	(-)	
Solids slip velocity factor	0.5	(-)	
Solids Properties (DEM)			
Coefficient of friction, μ_{pp}, μ_{pw}	0.1	(-)	
Coefficient of restitution, e_{pp}, e_{pw}	0.9	(-)	
Spring constant, k_{pp}, k_{pw}	100.0	($\text{kg}\cdot\text{m}^{-1}$)	
Initial Conditions			
x-velocity, u_g	0.0	($\text{m}\cdot\text{s}^{-1}$)	
y-velocity, v_g	0.0	($\text{m}\cdot\text{s}^{-1}$)	
z-velocity, w_g	0.0	($\text{m}\cdot\text{s}^{-1}$)	
Location of the shock	0.8	(m)	

continues on next page

Table 7.7 – continued from previous page

Computational/Physical model			
Gas volume fraction, ϵ_g	1.0	(-)	
Solids concentration, ϵ_{s0}	0.10, 0.15, 0.20	(-)	
Gas volume fraction at packing, ϵ_g^*	0.4	(-)	
Pressure, P_g	101,325	(Pa)	
Boundary Conditions			
Cyclic in x, z directions			
South boundary	0.0	(m·s ⁻¹)	Free-slip wall
North boundary	0.0	(m·s ⁻¹)	Free-slip wall

7.4.3 Results

The solutions from MFiX-PIC, MFiX-DEM, and MFiX-TFM are compared with the analytical expression in Fig. 7.4. Linear-hat scheme is used to interpolate between the Eulerian and Lagrangian fields. MFiX-TFM solutions based on continuum formulation are observed to be free from oscillations in the volume fraction field for all the cases considered. Besides, the time evolution of wave fronts is also shown for simulations corresponding to $\epsilon_{s0} = 0.15$ in Fig. 7.5. The results are in good agreement with the analytical solution. Further, the influence of initial solids fraction on the modelling accuracy is tested. The shock wave corresponding to filling (traveling upwards) is predicted reasonably well by all the models. This verifies the implementation of algorithms corresponding to packed regions. The analytical values along with model predictions are summarized in Table 7.8 and Table 7.9 for settling and filling wave fronts. The location of the filling wave front is determined by the occurrence of first local minima in the gradient of void fraction ϵ_g , while the settling wave front is determined by the last local minima in the gradient. The uncertainty values associated with the computational results correspond to cell width (0.01 m) since the shock front is estimated from discrete values.

Table 7.8: Location of Filling Wave Moving in the Direction of Gravity (m).

	$\epsilon_{s0} = 0.10$	$\epsilon_{s0} = 0.15$	$\epsilon_{s0} = 0.20$
Analytical	0.466	0.544	0.607
MFiX-PIC	0.471 ± 0.01	0.531 ± 0.01	0.585 ± 0.01
MFiX-DEM	0.455 ± 0.01	0.515 ± 0.01	0.575 ± 0.01
MFiX-TFM	0.485 ± 0.01	0.555 ± 0.01	0.605 ± 0.01

Table 7.9: Location of Filling Wave Moving Against the Direction of Gravity (m).

	$\epsilon_{s0} = 0.10$	$\epsilon_{s0} = 0.15$	$\epsilon_{s0} = 0.20$
Analytical	0.058	0.075	0.085
MFiX-PIC	0.065 ± 0.01	0.087 ± 0.01	0.101 ± 0.01
MFiX-DEM	0.073 ± 0.01	0.095 ± 0.01	0.115 ± 0.01
MFiX-TFM	0.065 ± 0.01	0.085 ± 0.01	0.095 ± 0.01

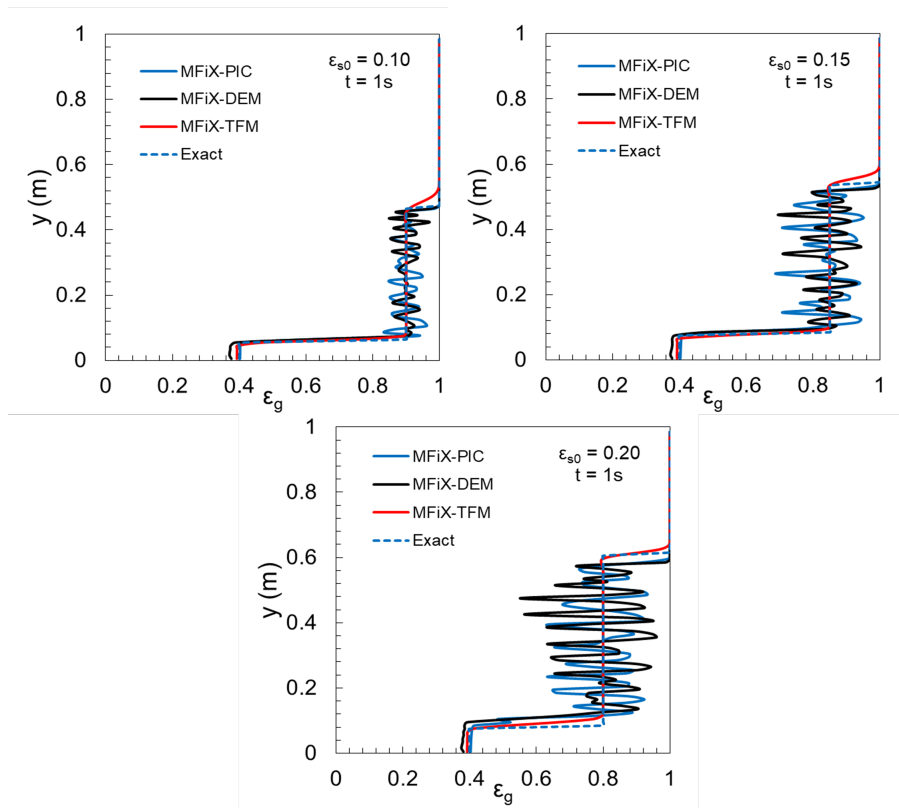


Fig. 7.4: Solutions for different initial particle concentrations: (a) 0.10, (b) 0.15, (c) 0.20.

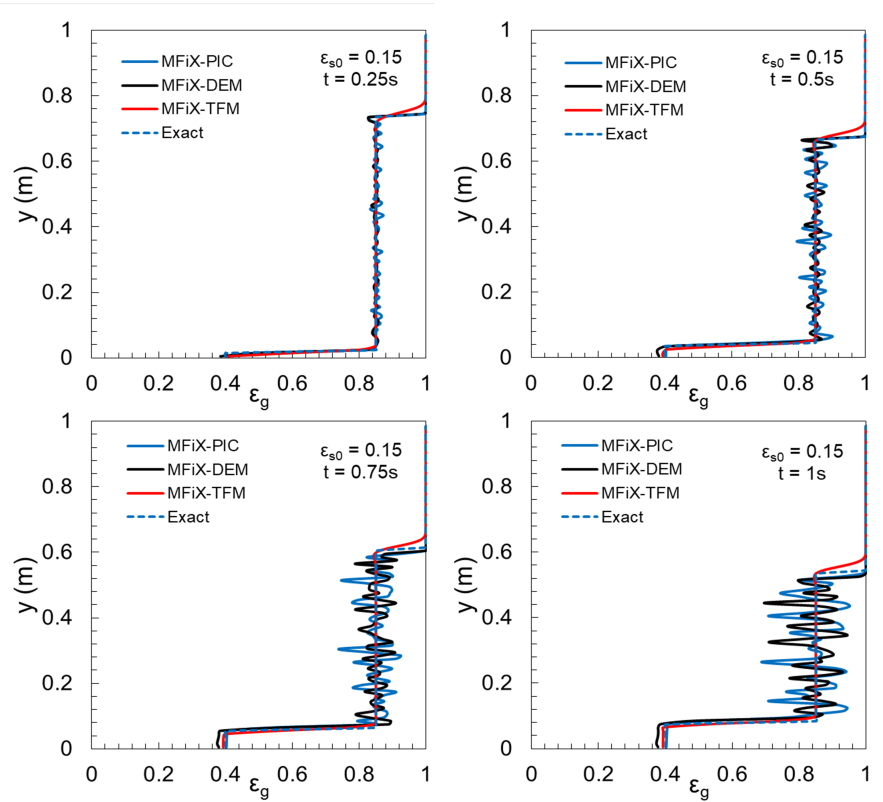


Fig. 7.5: Time evolution of shock fronts with 0.15 initial concentration.

7.5 PIC05: Evaporation

7.5.1 Description

This case is used to verify the transport equations governing energy and species conservation. The setup consists of a single parcel representing a droplet suspended in a humidified air stream. This reflects the wet bulb phenomenon, where evaporation from the droplet results in a lowered humidified air temperature. The following reaction represents species transfer from the suspended droplet:



Fifteen seconds of physical time is simulated to ensure the droplet achieves a steady-state (SS) temperature. The SS temperature should then compare with the theoretical wet-bulb temperature.

7.5.2 Setup

Table 7.10: PIC-05 Setup, Initial and Boundary Conditions.

Computational/Physical model			
3D, Transient			
Multiphase			
Gravity			
Turbulence equations are not solved			
Uniform mesh			
First order upwind discretization scheme			
Geometry			
Coordinate system	Cartesian		Grid partitions
x-length	0.01	(m)	1
y-length	0.01	(m)	1
z-length	0.01	(m)	1
Material			
Gas density, ρ_g	Ideal gas law	($\text{kg}\cdot\text{m}^{-3}$)	
Solids Type	PIC,DEM		
Diameter, d_p	0.2	(mm)	
Density, ρ_s	958.6	($\text{kg}\cdot\text{m}^{-3}$)	
Solids Properties (PIC)			
Pressure linear scale factor, P_s	0.0	(Pa)	
Exponential scale factor, γ	1.0	(-)	
Statistical weight	25	(-)	
Solids Properties (DEM)			
Coefficient of friction, μ_{pp}, μ_{pw}	0.0	(-)	
Coefficient of restitution, e_{pp}, e_{pw}	1.0	(-)	
Spring constant, k_{pp}, k_{pw}	0.1	($\text{kg}\cdot\text{m}^{-1}$)	
Initial Conditions			

continues on next page

Table 7.10 – continued from previous page

Computational/Physical model			
x-velocity, u_g	3.0	($\text{m}\cdot\text{s}^{-1}$)	
y-velocity, v_g	0.0	($\text{m}\cdot\text{s}^{-1}$)	
z-velocity, w_g	0.0	($\text{m}\cdot\text{s}^{-1}$)	
Gas volume fraction, ϵ_g	0.999894	(-)	
Gas volume fraction at packing, ϵ_g^*	0.4	(-)	
Pressure, P_g	101,325	(Pa)	
Gas temperature, T_g	303.15	(K)	
Solid temperature, T_s	303.15	(K)	
Species fraction of air, X_{g1}	Varied	(-)	
Species fraction of water vapor, X_{g2}	Varied	(-)	
Boundary Conditions			
West boundary	u_g Varied	($\text{kg}\cdot\text{s}^{-1}$)	Mass inflow
	X_{g1}, X_{g2} Varied	(-)	
East boundary	101,325	(Pa)	Pressure outflow
North and South boundaries			Free-slip walls
Top and Bottom boundaries			Free-slip walls

7.5.3 Results

MFiX-PIC and MFiX-DEM simulations are performed by varying the relative humidity of surrounding air. Table 7.8 summarizes the different settings of relative humidity and the corresponding wet bulb temperatures. Based on the comparison of the data from [17] it can be concluded that the predictions from MFiX-PIC simulations are accurate Table 7.8. Also, the results are consistent with the predictions from MFiX-DEM.

Table 7.11: Location of Filling Wave Moving in the Direction of Gravity (m).

Rel. Humidity (%)	X_{g1}	X_{g2}	Mass Flow Rate (g/s)	Wet Bulb T ($^{\circ}\text{C}$)
0	1.000000	0.000000	0.349315	10.5
10	0.997390	0.002610	0.348762	13.2
20	0.994771	0.005229	0.348208	15.7
30	0.992144	0.007856	0.347655	18.0
40	0.989509	0.010491	0.347102	20.1
50	0.986865	0.013135	0.346548	22.0
60	0.984212	0.015788	0.345995	23.8
70	0.981552	0.018448	0.345442	25.5
80	0.978882	0.021118	0.344888	27.1
90	0.976204	0.023796	0.344335	28.6
100	0.973518	0.026482	0.343281	30.0

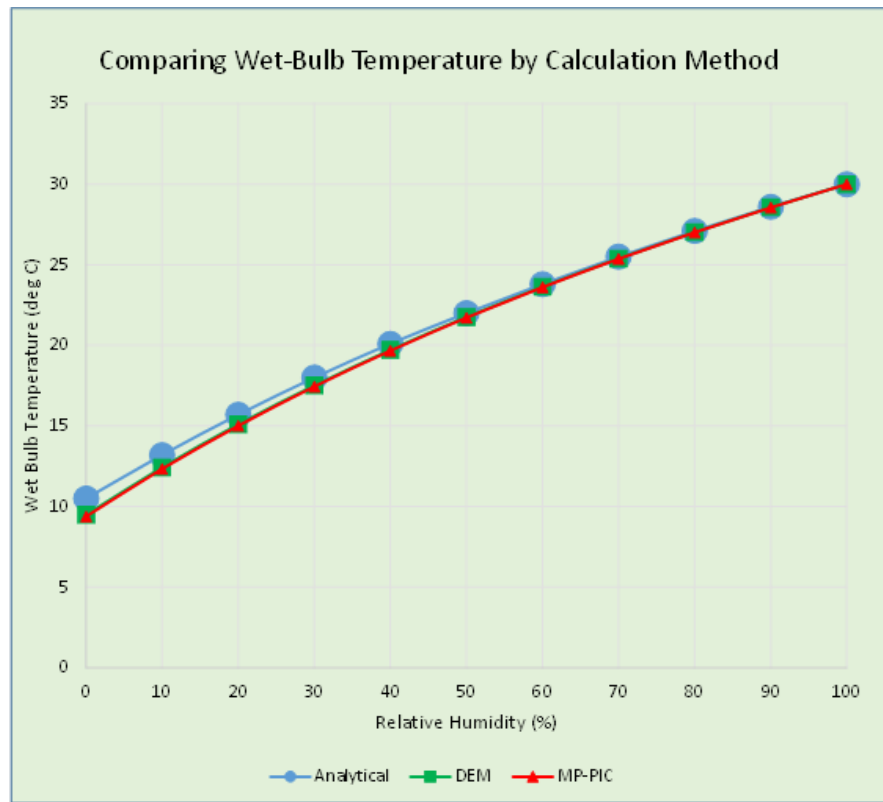


Fig. 7.6: Comparison of wet bulb temperatures between data, MFiX-DEM and MFiX-PIC.

7.6 PIC06: Rayleigh-Taylor Instability

7.6.1 Description

The simulation of Rayleigh-Taylor instability using PIC methodology follows the work of Snider [29]. The domain is initialized with a lighter phase at the bottom and a heavier phase at the top. When the simulation begins, the phases invert, and the growth of a mixing layer is recorded as a function of time. Researchers in the past have proposed the following functional form for the development of the mixing layer,

$$h = \alpha A g t^2 \tag{7.10}$$

where the non-dimensional parameter, A , used to characterize the system is Atwood number:

$$A = \frac{\rho_s - \rho_g}{\rho_s + \rho_g} \tag{7.11}$$

and the value of α is between 0.05 and 0.07 (Youngs [35]; Linden et al. [15]; Snider and Andrews [30]). A rectangular domain (0.1 m X 0.6 m X 0.1 m) is chosen for simulating this system. The values for fluid and particle properties are borrowed from the work of Snider [29]. A larger value of particle diameter is used and the interphase drag coefficient ($\propto 1/d_p$) is scaled accordingly. The list of parameters used in this exercise are summarized in Table 7.13.

Table 7.12: Material properties used in Rayleigh-Taylor Instability simulations

	Case 1	Case 2	Case 3
Particle diameter (m)	2 X 10 ⁻⁶	2 X 10 ⁻⁶	2 X 10 ⁻⁶
Particle density (kg/m ³)	3	5	7
Fluid density (kg/m ³)	1	1	1
Fluid viscosity (Pa-s)	0.001	0.001	0.001
Atwood number	0.1667	0.2857	0.4737
Drag coefficient, β (kg·m ⁻³ ·s ⁻¹)	100 $\rho_s \epsilon_s$	100 $\rho_s \epsilon_s$	100 $\rho_s \epsilon_s$

7.6.2 Setup

Table 7.13: PIC-06 Setup, Initial and Boundary Conditions.

Computational/Physical model			
3D, Transient			
Multiphase			
Gravity			
Thermal energy equation is not solved			
Turbulence equations are not solved (Laminar)			
Uniform mesh			
First order upwind discretization scheme			
Geometry			
Coordinate system	Cartesian		Grid partitions
x-length	0.10	(m)	40
y-length	0.60	(m)	240
z-length	0.10	(m)	40
Material			

continues on next page

Table 7.13 – continued from previous page

Computational/Physical model			
Gas density, ρ_g	1.0	($\text{kg}\cdot\text{m}^{-3}$)	
Gas viscosity, μ_g	1.8E-5	(Pa·s)	
Solids Type	PIC		
Diameter, d_p	0.001	(mm)	
Density, ρ_s	Table 7.12	($\text{kg}\cdot\text{m}^{-3}$)	
Solids Properties (PIC)			
Pressure linear scale factor, P_s	1.0	(Pa)	
Exponential scale factor, γ	4.0	(-)	
Statistical weight	7.2E+08	(-)	
Initial Conditions			
x-velocity, u_g	0.0	($\text{m}\cdot\text{s}^{-1}$)	
y-velocity, v_g	0.0	($\text{m}\cdot\text{s}^{-1}$)	
z-velocity, w_g	0.0	($\text{m}\cdot\text{s}^{-1}$)	
Gas volume fraction, ϵ_g	0.80	(-)	
Gas volume fraction at packing, ϵ_g^*	0.4	(-)	
Pressure, P_g	101,325	(Pa)	
Boundary Conditions			
Top boundary			Pressure outflow
All other boundaries			Free-slip walls

7.6.3 Results

The contour plots Fig. 7.7 show the evolution of volume fraction fields at the end of 1 second. The instability is triggered by a non-homogenous solids concentration field due to inherent randomness in generating the parcels. The instability is more pronounced at higher values of A. Fig. 7.8 shows the time evolution of the mixing layer, where the coordinates used by Snider [29] are used. The results are consistent with the work of Snider [29]. The analytical value for the slope of this curve based on Eq.7.10 is $\sqrt{\alpha}$, which is matched reasonably well by MFiX-PIC. As A increases, the particles reach the bottom of the domain sooner resulting in the associate curve reaching a plateau.

7.7 PIC07: Minimum fluidization

7.7.1 Description

A minimum fluidization test is used to validate the interphase momentum transfer between gas and particles. In contrast to particles settling in a quiescent fluid medium described in the case PIC, a gas phase enters the domain through the bottom boundary, initially through a fixed bed of particles. Once the minimum fluidization condition is reached, the particles change from a fixed state to a fluidized state. This action is accompanied by a change in pressure drop across the bed. The physical experiments were performed at NETL using high-density polyethylene (HDPE) particles in a rectangular domain (0.05 m X 0.20 m X 0.05 m). The mean diameter and density of HDPE are $870 \mu\text{m}$ and $860 \text{kg}\cdot\text{m}^{-3}$. Figure Fig. 7.9 shows the plot of pressure drop as a function of gas velocity, where the pressure drop is normalized by the weight of bed given by,

$$\Delta P^* = \frac{\Delta P}{\frac{mg}{A}} \quad (7.12)$$

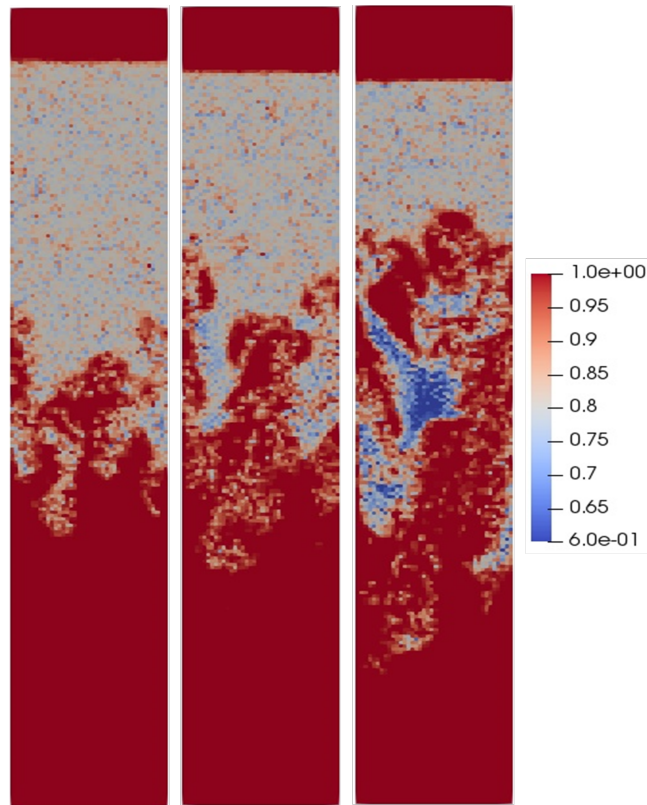


Fig. 7.7: Sectional view of volume fraction contour of the lighter phase at $t = 0.8s$; $A = 0.1667, 0.2857, \text{ and } 0.4737$ (left to right)

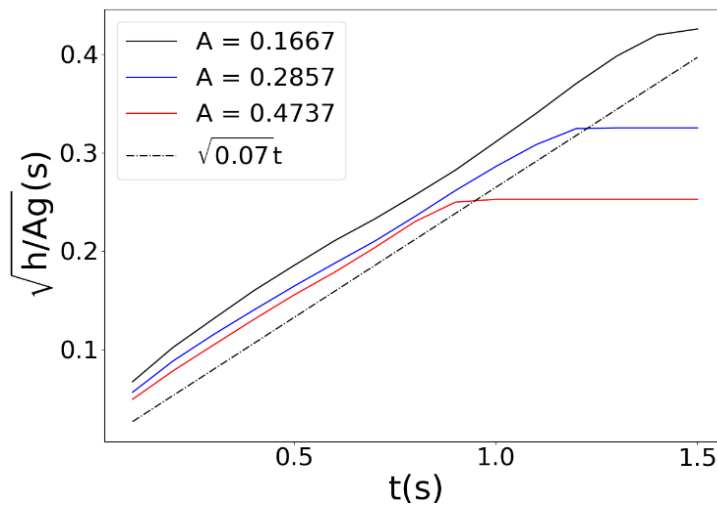


Fig. 7.8: Evolution of mixing layer for $A = 0.1667, 0.2857, \text{ and } 0.4737$. The dashed line is the theoretical solution, Eq.7.10.

where ΔP is the pressure drop across the bed, g is the mass of bed material, g is acceleration due to gravity and A is the cross-sectional area of the bed. There is a sharp transition between fixed and fluidized states which marks the minimum fluidization condition. The graphical abscissa at this transition is recognized as the minimum fluidization velocity and the ordinate is the pressure drop that corresponds to the weight of bed material. Based on linear fit between the two regions, minimum fluidization velocity for the case shown is 0.182 m/s .

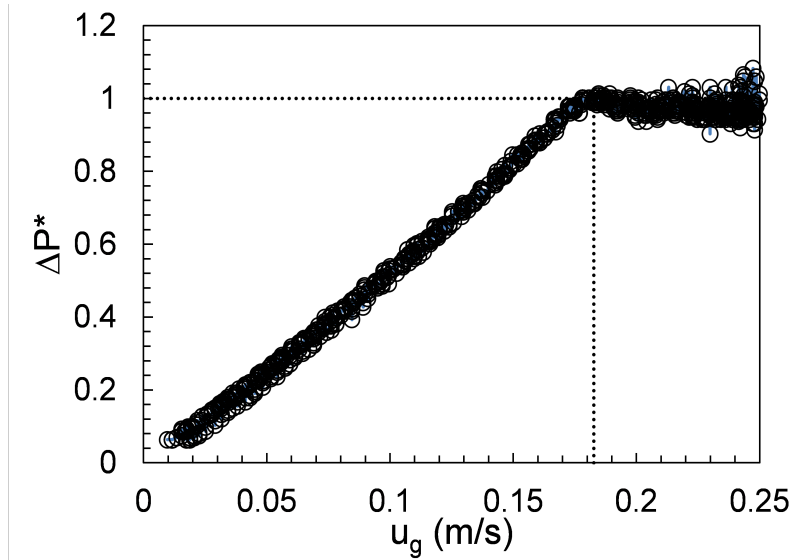


Fig. 7.9: Normalized pressure drop as a function of inlet gas velocity.

Considering the size of particles, it was decided to use a larger domain which could accommodate more computational parcels. Hence, this study used a rectangular domain (0.10 m X 0.40 m X 0.10 m). The drag correlation of Wen and Yu [3] is used for calculating the drag coefficient β given by,

$$C_d = \begin{cases} \frac{24}{Re}(1 + 0.15Re^{0.687}) & Re \leq 1000 \\ 0.44 & Re > 1000 \end{cases} \quad (7.13)$$

The particle's Reynolds number is defined as,

$$Re = \frac{\rho_g \epsilon_g |u_g - u_s| d_p}{\mu_g} \quad (7.14)$$

where, $\rho_g, \epsilon_g, u_g, \mu_g$ represent density, volume fraction, velocity, and dynamic viscosity of the gas phase. u_s, d_p are the velocity and diameter of particles in the solids phase (Note: d_p is the diameter of particle and not parcel).

7.7.2 Setup

Table 7.14: PIC-07 Setup, Initial and Boundary Conditions.

Computational/Physical model			
3D, Transient			
Multiphase			
Gravity			
Thermal energy equation is not solved			
Turbulence equations are not solved (Laminar)			
Uniform mesh			

continues on next page

Table 7.14 – continued from previous page

Computational/Physical model			
First order upwind discretization scheme			
Geometry			
Coordinate system	Cartesian		Grid partitions
x-length	0.10	(m)	10
y-length	0.40	(m)	40
z-length	0.10	(m)	10
Material			
Gas density, ρ_g	1.0	(kg·m ⁻³)	
Gas viscosity, μ_g	1.8E-5	(Pa·s)	
Solids Type	PIC		
Diameter, d_p	0.87	(mm)	
Density, ρ_s	860.0	(kg·m ⁻³)	
Solids Properties (PIC)			
Pressure linear scale factor, P_s	1.0	(Pa)	
Exponential scale factor, γ	4.0	(-)	
Statistical weight	4.0,5.0,10.0	(-)	
Gas volume fraction at packing, ϵ_g^*	0.44	(-)	
Initial Conditions			
x-velocity, u_g	0.0	(m·s ⁻¹)	
y-velocity, v_g	0.0	(m·s ⁻¹)	
z-velocity, w_g	0.0	(m·s ⁻¹)	
Gas volume fraction, ϵ_g	0.82	(-)	
Pressure, P_g	101,325	(Pa)	
Boundary Conditions			
South boundary, u_g	Varied	(m·s ⁻¹)	Mass inflow
North boundary, P_g	101,325	(Pa)	Pressure outflow
All other boundaries			No-slip walls

7.7.3 Results

Time-dependent boundary velocity for the gas-phase is specified through a user-defined subroutine. A linear ramp function is used, and pressure drop across the bed is extracted at regular intervals. It is worth reiterating that the domain considered for this numerical exercise is different from physical experiments, hence this study does not show the experimental curve in the resulting plots. However, minimum fluidization is expected to be the same barring minor differences due to factors including wall effects. The transition between fixed and fluidized states is not distinctly predicted by MFiX-PIC Fig. 7.10 as observed in the experiments. MFiX-PIC does not reproduce the behavior of HDPE particles at minimum fluidization velocity. This could be due to the nature of the particle-stress closure or uncertainty in model parameters. This could also point to a limitation of MFiX-PIC in modeling the fluidization transition from a fixed bed state. However, PIC is capable of predicting the pressure drop corresponding to the weight of bed material, further away from minimum fluidization conditions. Fig. 7.10 also highlights the negligible effect of parcel size for this case. Sensitivity of ϵ^* and P_s are also analyzed. For the range of P_s considered in this study, the behavior is unchanged for all practical purposes as observed in Fig. 7.11. However, as ϵ^* changed there is a noticeable difference in the fluidization behavior Fig. 7.12. Maximum sensitivity was observed for ϵ^* among other parameters considered in this study. A more systematic approach as outlined in Gel et al. [9] is required to draw further conclusions on the observed behavior.

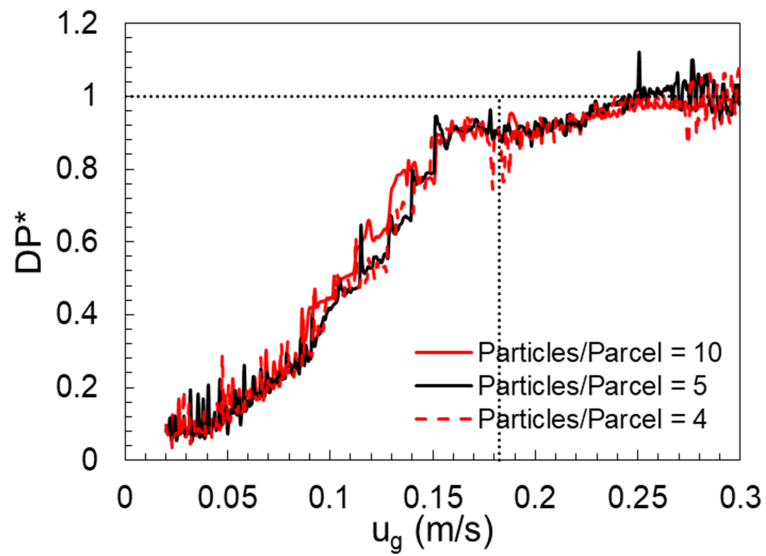


Fig. 7.10: Effect of statistical weight (particles per parcel) on fluidization curve using MFiX-PIC.

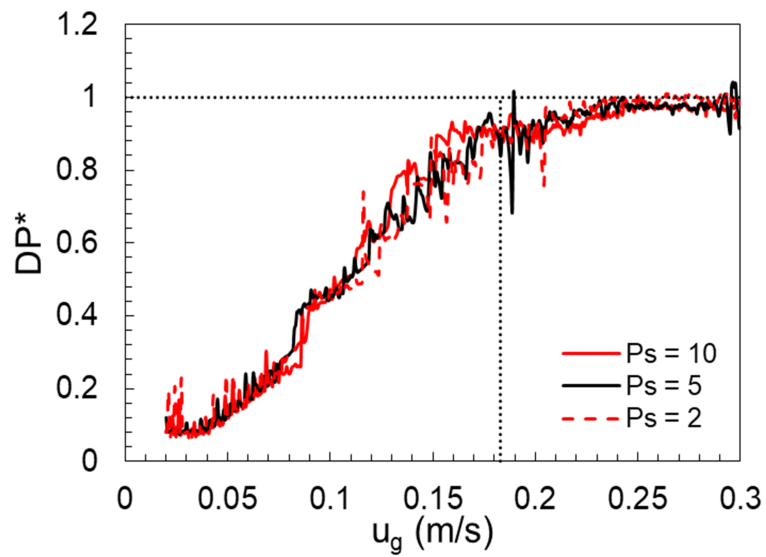


Fig. 7.11: Effect of varying P_s .

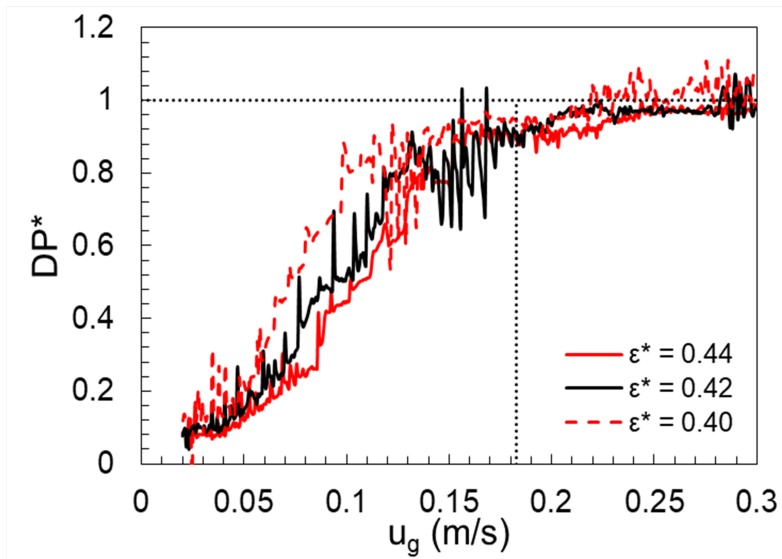


Fig. 7.12: Effect of varying gas volume fraction at packing ϵ_g^* .

MANUFACTURED SOLUTION MATHEMATICAL FORMS

(Note: All solution variables are in SI units.)

The baseline manufactured solution selected for the verification study is a combination of sine and cosine functions and takes the following general form [25], [1]

$$\begin{aligned} \phi(x, y, z) = & \phi_0 + \phi_x f_{\phi x} \left(\frac{a_{\phi x} \pi x}{L} \right) + \phi_y f_{\phi y} \left(\frac{a_{\phi y} \pi y}{L} \right) + \phi_z f_{\phi z} \left(\frac{a_{\phi z} \pi z}{L} \right) \\ & + \phi_{xy} f_{\phi xy} \left(\frac{a_{\phi xy} \pi xy}{L^2} \right) + \phi_{yz} f_{\phi yz} \left(\frac{a_{\phi yz} \pi yz}{L^2} \right) + \phi_{zx} f_{\phi zx} \left(\frac{a_{\phi zx} \pi zx}{L^2} \right) \end{aligned} \quad (8.1)$$

where, L is a characteristic length (herein, selected equal to the domain length or $L = 1$), and $\phi = [P_g, u_g, v_g, w_g, u_s, v_s, w_s, T_g, T_s]^T$ represents the set of primitive variables being tested for order of accuracy. The sinusoidal functions ($f_{\phi x}$, $f_{\phi y}$, etc.) selected are shown in Table 8.1

Table 8.1: Functions in baseline manufactured solutions.

Variable,	f_x	f_y	f_z	f_{xy}	f_{yz}	f_{zx}
u_g	sin	cos	cos	cos	sin	cos
v_g	sin	cos	cos	cos	sin	cos
w_g	cos	sin	cos	sin	sin	cos
u_s	sin	cos	cos	cos	sin	cos
v_s	sin	cos	cos	cos	sin	cos
w_s	cos	sin	cos	sin	sin	cos
P_g	cos	cos	sin	cos	sin	cos
T_g	cos	cos	sin	cos	sin	cos
T_s	cos	cos	sin	cos	sin	cos
ε_s	cos	cos	sin	–	–	–

The frequency constants ($a_{\phi x}$, $a_{\phi y}$, $a_{\phi xy}$, etc.) and the amplitude constants (ϕ_0 , ϕ_x , ϕ_{xy} , etc.) are selected to ensure functions that are smooth but show reasonable periodicity and magnitude within the domain. The frequency constants selected are shown in Table 8.2.

Table 8.2: Frequencies in baseline manufactured solutions.

Variable,	a_x	a_y	a_z	a_{xy}	a_{yz}	a_{zx}
u_g	0.5	0.85	0.4	0.6	0.8	0.9
v_g	0.8	0.8	0.5	0.9	0.4	0.6
w_g	0.85	0.9	0.5	0.4	0.8	0.75
u_s	0.5	0.85	0.4	0.6	0.8	0.9
v_s	0.8	0.8	0.5	0.9	0.4	0.6
w_s	0.85	0.9	0.5	0.4	0.8	0.75
P_g	0.4	0.45	0.85	0.75	0.7	0.8
T_g	0.75	1.25	0.8	0.65	0.5	0.6
T_s	0.5	0.9	0.8	0.5	0.65	0.4
ε_s	0.4	0.5	0.5	–	–	–

The amplitude constants selected are shown Table 8.3.

Table 8.3: Amplitudes in baseline manufactured solutions.

Variable,	0	x	y	z	xy	yz	zx
u_g	7	3	-4	-3	2	1.5	2
v_g	9	-5	4	5	-3	2.5	3.5
w_g	8	-4	3.5	4.2	-2.2	2.1	2.5
u_s	7	3	-4	-3	2	1.5	2
v_s	9	-5	4	5	-3	2.5	3.5
w_s	8	-4	3.5	4.2	-2.2	2.1	2.5
P_g	100	20	-50	20	-25	-10	10
T_g	350	10	-30	20	-12	10	8
T_s	300	15	-20	15	-10	12	10
ε_s	0.3	0.06	0.1	0.06	–	–	–

The baseline manufactured solutions presented above are used to generate manufactured solutions for the two-phase flow test cases. As an example, the manufactured solution for the test case presented in Section 4.6 is provided next.

The manufactured solutions for the scalar variables (P_g , T_g , and T_s) are simply obtained from Eq.8.1 and by substituting the appropriate functions and constants described above. For example, for the pressure variable (P_g), this function is as follow:

$$P_g = 100 + 20 \cos(0.4\pi x) - 50 \cos(0.45\pi y) + 20 \sin(0.85\pi z) - 25 \cos(0.75\pi xy) - 10 \sin(0.7\pi yz) + 10 \cos(0.8\pi zx) \quad (8.2)$$

The manufactured solutions for velocity components of the gas phase are obtained by taking the curl of the baseline velocity vector field, i.e.,

$$\vec{V}_g = u_g \hat{i} + v_g \hat{j} + w_g \hat{k} = \begin{vmatrix} \hat{i} & \hat{j} & \hat{k} \\ \frac{\partial}{\partial x} & \frac{\partial}{\partial y} & \frac{\partial}{\partial z} \\ \phi(u_g) & \phi(v_g) & \phi(w_g) \end{vmatrix} \quad (8.3)$$

where, for example, $\phi(u_g)$ is the baseline manufactured solution obtained from Eq.8.1, the functions, and the constants described above for the variable u_g . This results in a divergence free velocity field because $\nabla \cdot (\nabla \times \vec{H})$ is identically zero for any vector field, \vec{H} . Thus, the manufactured solution for u_g is given as:

$$u_g = -\pi y \cos(0.4\pi yz) + 2.5\pi \sin(0.5\pi z) + 2.1\pi x \sin(0.6\pi zx) - 0.88\pi x \cos(0.4\pi xy) + 3.15\pi \cos(0.9\pi y) + 0.68\pi z \cos(0.8\pi yz) \quad (8.4)$$

Similarly, the manufactured solution for v_g and w_g can be derived.

Finally, the manufactured solution for velocity components of the solids phase is selected as simply the following divergence free field:

$$u_s = 5 (0.5\pi (x + y + z)) \quad (8.5)$$

$$v_s = 5 (0.5\pi (x + y + z)) \quad (8.6)$$

$$w_s = 5 \quad (8.7)$$

Manufactured solutions for other MMS test cases presented are derived using the baseline manufactured solutions and appropriate constraints (divergence free field, boundary conditions, etc.). For a complete look at the MMS function and MMS source terms, please see the MMS_MOD.f file under the respective test case of the MFIX distribution.

8.1 MMS02 manufactured solutions

The manufactured solutions for the two-phase, 3D, curl-based functions with constant volume fraction are listed below.

Gas pressure:

$$p_g = p_{g0} + p_{gx} \cos(A_{p_{gx}} \pi x) + p_{gy} \cos(A_{p_{gy}} \pi y) + p_{gxy} \cos(A_{p_{gxy}} \pi xy) \\ + p_{gz} \sin(A_{p_{gz}} \pi z) + p_{gyz} \sin(A_{p_{gyz}} \pi yz) + p_{gzx} \cos(A_{p_{gzx}} \pi zx) \quad (8.8)$$

Gas velocity components:

$$u_g = A_{w_{gy}} \pi w_{gy} \cos(A_{w_{gy}} \pi y) + A_{w_{gxy}} \pi w_{gxy} x \cos(A_{w_{gxy}} \pi xy) \\ - A_{v_{gyz}} \pi v_{gyz} y \cos(A_{v_{gyz}} \pi yz) + A_{w_{gyz}} \pi w_{gyz} z \cos(A_{w_{gyz}} \pi yz) \\ + A_{v_{gz}} \pi v_{gz} \sin(A_{v_{gz}} \pi z) + A_{v_{gzx}} \pi v_{gzx} x \sin(A_{v_{gzx}} \pi zx) \quad (8.9)$$

$$v_g = -A_{w_{gxy}} \pi w_{gxy} y \cos(A_{w_{gxy}} \pi xy) + A_{u_{gyz}} \pi u_{gyz} y \cos(A_{u_{gyz}} \pi yz) \\ + A_{w_{gx}} \pi w_{gx} \sin(A_{w_{gx}} \pi x) - A_{u_{gz}} \pi u_{gz} \sin(A_{u_{gz}} \pi z) \\ - A_{u_{gzx}} \pi u_{gzx} x \sin(A_{u_{gzx}} \pi zx) + A_{w_{gzx}} \pi w_{gzx} z \sin(A_{w_{gzx}} \pi zx) \quad (8.10)$$

$$w_g = A_{v_{gx}} \pi v_{gx} \cos(A_{v_{gx}} \pi x) - A_{u_{gyz}} \pi u_{gyz} z \cos(A_{u_{gyz}} \pi yz) \\ + A_{u_{gy}} \pi u_{gy} \sin(A_{u_{gy}} \pi y) + A_{u_{gxy}} \pi u_{gxy} x \sin(A_{u_{gxy}} \pi xy) \\ - A_{v_{gxy}} \pi v_{gxy} y \sin(A_{v_{gxy}} \pi xy) - A_{v_{gzx}} \pi v_{gzx} z \sin(A_{v_{gzx}} \pi zx) \quad (8.11)$$

Solids velocity components:

$$u_m = u_{m0} \left(\frac{\pi}{2} (x + y + z) \right) \quad (8.12)$$

$$v_m = v_{m0} \left(\frac{\pi}{2} (x + y + z) \right) \quad (8.13)$$

$$w_m = w_{m0} \quad (8.14)$$

Gas and solids temperature:

$$T_g = T_{g0} + T_{gx} \cos(A_{T_{gx}} \pi x) + T_{gy} \cos(A_{T_{gy}} \pi y) + T_{gxy} \cos(A_{T_{gxy}} \pi xy) \\ + T_{gz} \sin(A_{T_{gz}} \pi z) + T_{gyz} \sin(A_{T_{gyz}} \pi yz) + T_{gzx} \cos(A_{T_{gzx}} \pi zx) \quad (8.15)$$

$$T_m = T_{m0} + T_{mx} \cos(A_{T_{mx}} \pi x) + T_{my} \cos(A_{T_{my}} \pi y) + T_{mxy} \cos(A_{T_{mxy}} \pi xy) \\ + T_{mz} \sin(A_{T_{mz}} \pi z) + T_{myz} \sin(A_{T_{myz}} \pi yz) + T_{mzx} \cos(A_{T_{mzx}} \pi zx) \quad (8.16)$$

Gas and solids volume fractions:

$$\varepsilon_g = 1 - (\varepsilon_{m0} + \varepsilon_{mx} \cos(A_{\varepsilon_{mx}} \pi x) + \varepsilon_{my} \cos(A_{\varepsilon_{my}} \pi y) + \varepsilon_{mxy} \cos(A_{\varepsilon_{mxy}} \pi xy) + \varepsilon_{mz} \sin(A_{\varepsilon_{mz}} \pi z) + \varepsilon_{myz} \sin(A_{\varepsilon_{myz}} \pi yz) + \varepsilon_{mzx} \cos(A_{\varepsilon_{mzx}} \pi zx)) \quad (8.17)$$

$$\varepsilon_m = \varepsilon_{m0} + \varepsilon_{mx} \cos(A_{\varepsilon_{mx}} \pi x) + \varepsilon_{my} \cos(A_{\varepsilon_{my}} \pi y) + \varepsilon_{mxy} \cos(A_{\varepsilon_{mxy}} \pi xy) + \varepsilon_{mz} \sin(A_{\varepsilon_{mz}} \pi z) + \varepsilon_{myz} \sin(A_{\varepsilon_{myz}} \pi yz) + \varepsilon_{mzx} \cos(A_{\varepsilon_{mzx}} \pi zx) \quad (8.18)$$

Solids granular temperature:

$$\theta_m = \theta_{m0} + \theta_{mx} \cos(A_{\theta_{mx}} \pi x) + \theta_{my} \cos(A_{\theta_{my}} \pi y) + \theta_{mxy} \cos(A_{\theta_{mxy}} \pi xy) + \theta_{mz} \sin(A_{\theta_{mz}} \pi z) + \theta_{myz} \sin(A_{\theta_{myz}} \pi yz) + \theta_{mzx} \cos(A_{\theta_{mzx}} \pi zx) \quad (8.19)$$

The parameters appearing in the manufactured solutions are as follows:

Table 8.4: Parameters in MMS02 manufactured solutions.

p_{g0}	100.0	v_{gx}	-5.0	w_{m0}	5.0	ε_{m0}	0.3
p_{gx}	20.0	v_{gy}	4.0	T_{g0}	350	ε_{mx}	0.0
p_{gy}	-50.0	v_{gz}	5.0	T_{gx}	10	ε_{my}	0.0
p_{gz}	20.0	v_{gxy}	-3.0	T_{gy}	-30	ε_{mz}	0.0
p_{gxy}	-25.0	v_{gyz}	2.5	T_{gz}	20	ε_{mxy}	0.0
p_{gyz}	-10.0	v_{gzx}	3.5	T_{gxy}	-12	ε_{myz}	0.0
p_{gzx}	10.0	$A_{v_{gx}}$	0.8	T_{gyz}	10	ε_{mzx}	0.0
$A_{p_{gx}}$	0.4	$A_{v_{gy}}$	0.8	T_{gzx}	8	$A_{\varepsilon_{mx}}$	0.5
$A_{p_{gy}}$	0.45	$A_{v_{gz}}$	0.5	$A_{T_{gx}}$	0.75	$A_{\varepsilon_{my}}$	0.5
$A_{p_{gz}}$	0.85	$A_{v_{gxy}}$	0.9	$A_{T_{gy}}$	1.25	$A_{\varepsilon_{mz}}$	0.5
$A_{p_{gxy}}$	0.75	$A_{v_{gyz}}$	0.4	$A_{T_{gz}}$	0.8	$A_{\varepsilon_{mxy}}$	0.4
$A_{p_{gyz}}$	0.7	$A_{v_{gzx}}$	0.6	$A_{T_{gxy}}$	0.65	$A_{\varepsilon_{myz}}$	0.4
$A_{p_{gzx}}$	0.8	w_{g0}	8.0	$A_{T_{gyz}}$	0.5	$A_{\varepsilon_{mzx}}$	0.4
u_{g0}	7.0	w_{gx}	-4.0	$A_{T_{gzx}}$	0.6	θ_{m0}	100.0
u_{gx}	3.0	w_{gy}	3.5	T_{m0}	300	θ_{mx}	5.0
u_{gy}	-4.0	w_{gz}	4.2	T_{mx}	15	θ_{my}	-10.0
u_{gz}	-3.0	w_{gxy}	-2.2	T_{my}	-20	θ_{mz}	12.0
u_{gxy}	2.0	w_{gyz}	2.1	T_{mz}	15	θ_{mxy}	-8.0
u_{gyz}	1.5	w_{gzx}	2.5	T_{mxy}	-10	θ_{myz}	10.0
u_{gzx}	-2.0	$A_{w_{gx}}$	0.85	T_{myz}	12	θ_{mzx}	7.0
$A_{u_{gx}}$	0.5	$A_{w_{gy}}$	0.9	T_{mzx}	10	$A_{\theta_{mx}}$	0.8
$A_{u_{gy}}$	0.85	$A_{w_{gz}}$	0.5	$A_{T_{mx}}$	0.5	$A_{\theta_{my}}$	1.25
$A_{u_{gz}}$	0.4	$A_{w_{gxy}}$	0.4	$A_{T_{my}}$	0.9	$A_{\theta_{mz}}$	0.7
$A_{u_{gxy}}$	0.6	$A_{w_{gyz}}$	0.8	$A_{T_{mz}}$	0.8	$A_{\theta_{mxy}}$	0.5
$A_{u_{gyz}}$	0.8	$A_{w_{gzx}}$	0.75	$A_{T_{mxy}}$	0.5	$A_{\theta_{myz}}$	0.6
$A_{u_{gzx}}$	0.9	u_{m0}	5.0	$A_{T_{myz}}$	0.65	$A_{\theta_{mzx}}$	0.7
v_{g0}	9.0	v_{m0}	5.0	$A_{T_{mzx}}$	0.4		

8.2 MMS03 manufactured solutions

The manufactured solutions for the two-phase, 3D, curl-based functions with variable volume fraction are listed below.

Gas pressure:

$$p_g = p_{g0} + p_{gx} \cos(A_{p_{gx}} \pi x) + p_{gy} \cos(A_{p_{gy}} \pi y) + p_{gxy} \cos(A_{p_{gxy}} \pi xy) \\ + p_{gz} \sin(A_{p_{gz}} \pi z) + p_{gyz} \sin(A_{p_{gyz}} \pi yz) + p_{gzx} \cos(A_{p_{gzx}} \pi zx) \quad (8.20)$$

Gas velocity components:

$$u_g = \frac{1}{\varepsilon_g} [A_{w_{gy}} \pi w_{gy} \cos(A_{w_{gy}} \pi y) + A_{w_{gxy}} \pi w_{gxy} x \cos(A_{w_{gxy}} \pi xy) \\ - A_{v_{gyz}} \pi v_{gyz} y \cos(A_{v_{gyz}} \pi yz) + A_{w_{gyz}} \pi w_{gyz} z \cos(A_{w_{gyz}} \pi yz) \\ + A_{v_{gzx}} \pi v_{gzx} \sin(A_{v_{gzx}} \pi z) + A_{v_{gzx}} \pi v_{gzx} x \sin(A_{v_{gzx}} \pi zx)] \quad (8.21)$$

$$v_g = \frac{1}{\varepsilon_g} [-A_{w_{gxy}} \pi w_{gxy} y \cos(A_{w_{gxy}} \pi xy) + A_{u_{gyz}} \pi u_{gyz} y \cos(A_{u_{gyz}} \pi yz) \\ + A_{w_{gx}} \pi w_{gx} \sin(A_{w_{gx}} \pi x) - A_{u_{gz}} \pi u_{gz} \sin(A_{u_{gz}} \pi z) \\ - A_{u_{gzx}} \pi u_{gzx} x \sin(A_{u_{gzx}} \pi zx) + A_{w_{gzx}} \pi w_{gzx} z \sin(A_{w_{gzx}} \pi zx)] \quad (8.22)$$

$$w_g = \frac{1}{\varepsilon_g} [A_{v_{gx}} \pi v_{gx} \cos(A_{v_{gx}} \pi x) - A_{u_{gyz}} \pi u_{gyz} z \cos(A_{u_{gyz}} \pi yz) \\ + A_{u_{gxy}} \pi u_{gxy} x \sin(A_{u_{gxy}} \pi xy) + A_{u_{gy}} \pi u_{gy} \sin(A_{u_{gy}} \pi y) \\ - A_{v_{gxy}} \pi v_{gxy} y \sin(A_{v_{gxy}} \pi xy) - A_{v_{gzx}} \pi v_{gzx} z \sin(A_{v_{gzx}} \pi zx)] \quad (8.23)$$

Solids velocity components:

$$u_m = \frac{1}{\varepsilon_m} \left[u_{m0} \left(\frac{\pi}{2} (x + y + z) \right) \right] \quad (8.24)$$

$$v_m = \frac{1}{\varepsilon_m} \left[v_{m0} \left(\frac{\pi}{2} (x + y + z) \right) \right] \quad (8.25)$$

$$w_m = \frac{1}{\varepsilon_m} w_{m0} \quad (8.26)$$

Gas and solids temperature:

$$T_g = T_{g0} + T_{gx} \cos(A_{T_{gx}} \pi x) + T_{gy} \cos(A_{T_{gy}} \pi y) + T_{gxy} \cos(A_{T_{gxy}} \pi xy) \\ + T_{gz} \sin(A_{T_{gz}} \pi z) + T_{gyz} \sin(A_{T_{gyz}} \pi yz) + T_{gzx} \cos(A_{T_{gzx}} \pi zx) \quad (8.27)$$

$$T_m = T_{m0} + T_{mx} \cos(A_{T_{mx}} \pi x) + T_{my} \cos(A_{T_{my}} \pi y) + T_{mxy} \cos(A_{T_{mxy}} \pi xy) \\ + T_{mz} \sin(A_{T_{mz}} \pi z) + T_{myz} \sin(A_{T_{myz}} \pi yz) + T_{mzx} \cos(A_{T_{mzx}} \pi zx) \quad (8.28)$$

Solids granular temperature:

$$\theta_m = \theta_{m0} + \theta_{mx} \cos(A_{\theta_{mx}} \pi x) + \theta_{my} \cos(A_{\theta_{my}} \pi y) + \theta_{mxy} \cos(A_{\theta_{mxy}} \pi xy) \\ + \theta_{mz} \sin(A_{\theta_{mz}} \pi z) + \theta_{myz} \sin(A_{\theta_{myz}} \pi yz) + \theta_{mzx} \cos(A_{\theta_{mzx}} \pi zx) \quad (8.29)$$

The parameters appearing in the manufactured solutions are as follows:

Table 8.5: Parameters in MMS03 manufactured solutions.

p_{g0}	100.0	v_{gx}	-5.0	w_{m0}	5.0	ε_{m0}	0.3
p_{gx}	20.0	v_{gy}	4.0	T_{g0}	350	ε_{mx}	0.06
p_{gy}	-50.0	v_{gz}	5.0	T_{gx}	10	ε_{my}	-0.1
p_{gz}	20.0	v_{gxy}	-3.0	T_{gy}	-30	ε_{mz}	0.06
p_{gxy}	-25.0	v_{gyz}	2.5	T_{gz}	20	ε_{mxy}	0.0
p_{gyz}	-10.0	v_{gzx}	3.5	T_{gxy}	-12	ε_{myz}	0.0
p_{gzx}	10.0	$A_{v_{gx}}$	0.8	T_{gyz}	10	ε_{mzx}	0.0
$A_{p_{gx}}$	0.4	$A_{v_{gy}}$	0.8	T_{gzx}	8	$A_{\varepsilon_{mx}}$	0.4
$A_{p_{gy}}$	0.45	$A_{v_{gz}}$	0.5	$A_{T_{gx}}$	0.75	$A_{\varepsilon_{my}}$	0.5
$A_{p_{gz}}$	0.85	$A_{v_{gxy}}$	0.9	$A_{T_{gy}}$	1.25	$A_{\varepsilon_{mz}}$	0.5
$A_{p_{gxy}}$	0.75	$A_{v_{gyz}}$	0.4	$A_{T_{gz}}$	0.8	$A_{\varepsilon_{mxy}}$	0.4
$A_{p_{gyz}}$	0.7	$A_{v_{gzx}}$	0.6	$A_{T_{gxy}}$	0.65	$A_{\varepsilon_{myz}}$	0.4
$A_{p_{gzx}}$	0.8	w_{g0}	8.0	$A_{T_{gyz}}$	0.5	$A_{\varepsilon_{mzx}}$	0.4
u_{g0}	7.0	w_{gx}	-4.0	$A_{T_{gzx}}$	0.6	θ_{m0}	100.0
u_{gx}	3.0	w_{gy}	3.5	T_{m0}	300	θ_{mx}	5.0
u_{gy}	-4.0	w_{gz}	4.2	T_{mx}	15	θ_{my}	-10.0
u_{gz}	-3.0	w_{gxy}	-2.2	T_{my}	-20	θ_{mz}	12.0
u_{gxy}	2.0	w_{gyz}	2.1	T_{mz}	15	θ_{mxy}	-8.0
u_{gyz}	1.5	w_{gzx}	2.5	T_{mxy}	-10	θ_{myz}	10.0
u_{gzx}	-2.0	$A_{w_{gx}}$	0.85	T_{myz}	12	θ_{mzx}	7.0
$A_{u_{gx}}$	0.5	$A_{w_{gy}}$	0.9	T_{mzx}	10	$A_{\theta_{mx}}$	0.8
$A_{u_{gy}}$	0.85	$A_{w_{gz}}$	0.5	$A_{T_{mx}}$	0.5	$A_{\theta_{my}}$	1.25
$A_{u_{gz}}$	0.4	$A_{w_{gxy}}$	0.4	$A_{T_{my}}$	0.9	$A_{\theta_{mz}}$	0.7
$A_{u_{gxy}}$	0.6	$A_{w_{gyz}}$	0.8	$A_{T_{mz}}$	0.8	$A_{\theta_{mxy}}$	0.5
$A_{u_{gyz}}$	0.8	$A_{w_{gzx}}$	0.75	$A_{T_{mxy}}$	0.5	$A_{\theta_{myz}}$	0.6
$A_{u_{gzx}}$	0.9	u_{m0}	5.0	$A_{T_{myz}}$	0.65	$A_{\theta_{mzx}}$	0.7
v_{g0}	9.0	v_{m0}	5.0	$A_{T_{mzx}}$	0.4		

8.3 MMS04 manufactured solutions

The manufactured solutions for the No-slip wall BC, single phase, 3D, curl-based functions are listed below.

Gas pressure:

$$\begin{aligned}
 p_g = & p_{g0} + p_{gx} \cos(A_{p_{gx}} \pi x) + p_{gy} \cos(A_{p_{gy}} \pi y) + p_{gxy} \cos(A_{p_{gxy}} \pi xy) \\
 & + p_{gz} \sin(A_{p_{gz}} \pi z) + p_{gyz} \sin(A_{p_{gyz}} \pi yz) + p_{gzx} \cos(A_{p_{gzx}} \pi zx)
 \end{aligned} \tag{8.30}$$

Gas velocity components:

$$\begin{aligned}
 u_g = & x^2 [A_{w_{gy}} \pi w_{gy} \cos(A_{w_{gy}} \pi y) + A_{w_{gxy}} \pi w_{gxy} x \cos(A_{w_{gxy}} \pi xy) \\
 & - A_{v_{gyz}} \pi v_{gyz} y \cos(A_{v_{gyz}} \pi yz) + A_{w_{gyz}} \pi w_{gyz} z \cos(A_{w_{gyz}} \pi yz) \\
 & + A_{v_{gz}} \pi v_{gz} \sin(A_{v_{gz}} \pi z) + A_{v_{gzx}} \pi v_{gzx} x \sin(A_{v_{gzx}} \pi zx)]
 \end{aligned} \tag{8.31}$$

$$\begin{aligned}
 v_g = & x^2 [-A_{w_{gxy}} \pi w_{gxy} y \cos(A_{w_{gxy}} \pi xy) + A_{u_{gyz}} \pi u_{gyz} y \cos(A_{u_{gyz}} \pi yz) \\
 & + A_{w_{gx}} \pi w_{gx} \sin(A_{w_{gx}} \pi x) - A_{u_{gz}} \pi u_{gz} \sin(A_{u_{gz}} \pi z) \\
 & - A_{u_{gzx}} \pi u_{gzx} x \sin(A_{u_{gzx}} \pi zx) + A_{w_{gzx}} \pi w_{gzx} z \sin(A_{w_{gzx}} \pi zx)] \\
 & + 2x [-w_{g0} - w_{gx} \cos(A_{w_{gx}} \pi x) - w_{gz} \cos(A_{w_{gz}} \pi z) \\
 & - w_{gzx} \cos(A_{w_{gzx}} \pi zx) - w_{gy} \sin(A_{w_{gy}} \pi y) \\
 & - w_{gxy} \sin(A_{w_{gxy}} \pi xy) - w_{gyz} \sin(A_{w_{gyz}} \pi yz)]
 \end{aligned} \tag{8.32}$$

$$\begin{aligned}
 w_g = x^2 [& A_{v_{gx}} \pi v_{gx} \cos(A_{v_{gx}} \pi x) - A_{u_{gyz}} \pi u_{gyz} z \cos(A_{u_{gyz}} \pi yz) \\
 & + A_{u_{gy}} \pi u_{gy} \sin(A_{u_{gy}} \pi y) + A_{u_{gxy}} \pi u_{gxy} x \sin(A_{u_{gxy}} \pi xy) \\
 & - A_{v_{gxy}} \pi v_{gxy} y \sin(A_{v_{gxy}} \pi xy) - A_{v_{gzx}} \pi v_{gzx} z \sin(A_{v_{gzx}} \pi zx)] \\
 & + 2x [v_{g0} + v_{gy} \cos(A_{v_{gy}} \pi y) + v_{gxy} \cos(A_{v_{gxy}} \pi xy) \\
 & + v_{gz} \cos(A_{v_{gz}} \pi z) + v_{gzx} \cos(A_{v_{gzx}} \pi zx) \\
 & + v_{gx} \sin(A_{v_{gx}} \pi x) + v_{gyz} \sin(A_{v_{gyz}} \pi yz)]
 \end{aligned} \tag{8.33}$$

Gas volume fraction:

$$\varepsilon_g = 1.0 \tag{8.34}$$

The parameters appearing in the manufactured solutions are as follows:

Table 8.6: Parameters in MMS04 manufactured solutions.

p_{g0}	100.0	v_{g0}	9.0	u_{g0}	7.0	w_{g0}	8.0
p_{gx}	20.0	v_{gx}	-5.0	u_{gx}	3.0	w_{gx}	-4.0
p_{gy}	-50.0	v_{gy}	4.0	u_{gy}	-4.0	w_{gy}	3.5
p_{gz}	20.0	v_{gz}	5.0	u_{gz}	-3.0	w_{gz}	4.2
p_{gxy}	-25.0	v_{gxy}	-3.0	u_{gxy}	2.0	w_{gxy}	-2.2
p_{gyz}	-10.0	v_{gyz}	2.5	u_{gyz}	1.5	w_{gyz}	2.1
p_{gzx}	10.0	v_{gzx}	3.5	u_{gzx}	-2.0	w_{gzx}	2.5
$A_{p_{gx}}$	0.4	$A_{v_{gx}}$	0.8	$A_{u_{gx}}$	0.5	$A_{w_{gx}}$	0.85
$A_{p_{gy}}$	0.45	$A_{v_{gy}}$	0.8	$A_{u_{gy}}$	0.85	$A_{w_{gy}}$	0.9
$A_{p_{gz}}$	0.85	$A_{v_{gz}}$	0.5	$A_{u_{gz}}$	0.4	$A_{w_{gz}}$	0.5
$A_{p_{gxy}}$	0.75	$A_{v_{gxy}}$	0.9	$A_{u_{gxy}}$	0.6	$A_{w_{gxy}}$	0.4
$A_{p_{gyz}}$	0.7	$A_{v_{gyz}}$	0.4	$A_{u_{gyz}}$	0.8	$A_{w_{gyz}}$	0.8
$A_{p_{gzx}}$	0.8	$A_{v_{gzx}}$	0.6	$A_{u_{gzx}}$	0.9	$A_{w_{gzx}}$	0.75

8.4 MMS05 manufactured solutions

The manufactured solutions for the Free-slip wall BC, single phase, 3D, curl-based functions are listed below.

Gas pressure:

$$\begin{aligned}
 p_g = p_{g0} + p_{gx} \cos(A_{p_{gx}} \pi x) + p_{gy} \cos(A_{p_{gy}} \pi y) + p_{gxy} \cos(A_{p_{gxy}} \pi xy) \\
 + p_{gz} \sin(A_{p_{gz}} \pi z) + p_{gyz} \sin(A_{p_{gyz}} \pi yz) + p_{gzx} \cos(A_{p_{gzx}} \pi zx)
 \end{aligned} \tag{8.35}$$

Gas velocity components:

$$\begin{aligned}
 u_g = x^3 [& A_{w_{gy}} \pi w_{gy} \cos(A_{w_{gy}} \pi y) + A_{w_{gxy}} \pi w_{gxy} x \cos(A_{w_{gxy}} \pi xy) \\
 & - A_{v_{gyz}} \pi v_{gyz} y \cos(A_{v_{gyz}} \pi yz) + A_{w_{gyz}} \pi w_{gyz} z \cos(A_{w_{gyz}} \pi yz) \\
 & + A_{v_{gz}} \pi v_{gz} \sin(A_{v_{gz}} \pi z) + A_{v_{gzx}} \pi v_{gzx} x \sin(A_{v_{gzx}} \pi zx)] \\
 v_g = v_{g0} + x^3 [& - A_{w_{gxy}} \pi w_{gxy} y \cos(A_{w_{gxy}} \pi xy) + A_{u_{gyz}} \pi u_{gyz} y \cos(A_{u_{gyz}} \pi yz) \\
 & + A_{w_{gx}} \pi w_{gx} \sin(A_{w_{gx}} \pi x) - A_{u_{gz}} \pi u_{gz} \sin(A_{u_{gz}} \pi z) \\
 & - A_{u_{gzx}} \pi u_{gzx} x \sin(A_{u_{gzx}} \pi zx) + A_{w_{gzx}} \pi w_{gzx} z \sin(A_{w_{gzx}} \pi zx)] \\
 & + 3x^2 [- w_{g0} - w_{gx} \cos(A_{w_{gx}} \pi x) - w_{gz} \cos(A_{w_{gz}} \pi z) \\
 & - w_{gzx} \cos(A_{w_{gzx}} \pi zx) - w_{gy} \sin(A_{w_{gy}} \pi y) \\
 & - w_{gxy} \sin(A_{w_{gxy}} \pi xy) - w_{gyz} \sin(A_{w_{gyz}} \pi yz)]
 \end{aligned} \tag{8.36}$$

$$\begin{aligned}
 w_g = & w_{g0} + x^3 [A_{v_{gx}} \pi v_{gx} \cos(A_{v_{gx}} \pi x) - A_{u_{gyz}} \pi u_{gyz} z \cos(A_{u_{gyz}} \pi yz) \\
 & + A_{u_{gxy}} \pi u_{gxy} x \sin(A_{u_{gxy}} \pi xy) + A_{u_{gy}} \pi u_{gy} \sin(A_{u_{gy}} \pi y) \\
 & - A_{v_{gxy}} \pi v_{gxy} y \sin(A_{v_{gxy}} \pi xy) - A_{v_{gzx}} \pi v_{gzx} z \sin(A_{v_{gzx}} \pi zx)] \\
 & + 3x^2 [v_{g0} + v_{gy} \cos(A_{v_{gy}} \pi y) + v_{gxy} \cos(A_{v_{gxy}} \pi xy) \\
 & + v_{gz} \cos(A_{v_{gz}} \pi z) + v_{gzx} \cos(A_{v_{gzx}} \pi zx) \\
 & + v_{gx} \sin(A_{v_{gx}} \pi x) + v_{gyz} \sin(A_{v_{gyz}} \pi yz)]
 \end{aligned} \tag{8.38}$$

Gas volume fraction:

$$\varepsilon_g = 1.0 \tag{8.39}$$

The parameters appearing in the manufactured solutions are as follows:

Table 8.7: Parameters in MMS05 manufactured solutions.

p_{g0}	100.0	v_{g0}	9.0	u_{g0}	7.0	w_{g0}	8.0
p_{gx}	20.0	v_{gx}	-5.0	u_{gx}	3.0	w_{gx}	-4.0
p_{gy}	-50.0	v_{gy}	4.0	u_{gy}	-4.0	w_{gy}	3.5
p_{gz}	20.0	v_{gz}	5.0	u_{gz}	-3.0	w_{gz}	4.2
p_{gxy}	-25.0	v_{gxy}	-3.0	u_{gxy}	2.0	w_{gxy}	-2.2
p_{gyz}	-10.0	v_{gyz}	2.5	u_{gyz}	1.5	w_{gyz}	2.1
p_{gzx}	10.0	v_{gzx}	3.5	u_{gzx}	-2.0	w_{gzx}	2.5
$A_{p_{gx}}$	0.4	$A_{v_{gx}}$	0.8	$A_{u_{gx}}$	0.5	$A_{w_{gx}}$	0.85
$A_{p_{gy}}$	0.45	$A_{v_{gy}}$	0.8	$A_{u_{gy}}$	0.85	$A_{w_{gy}}$	0.9
$A_{p_{gz}}$	0.85	$A_{v_{gz}}$	0.5	$A_{u_{gz}}$	0.4	$A_{w_{gz}}$	0.5
$A_{p_{gxy}}$	0.75	$A_{v_{gxy}}$	0.9	$A_{u_{gxy}}$	0.6	$A_{w_{gxy}}$	0.4
$A_{p_{gyz}}$	0.7	$A_{v_{gyz}}$	0.4	$A_{u_{gyz}}$	0.8	$A_{w_{gyz}}$	0.8
$A_{p_{gzx}}$	0.8	$A_{v_{gzx}}$	0.6	$A_{u_{gzx}}$	0.9	$A_{w_{gzx}}$	0.75

ANALYTICAL SOLUTION FOR PARTICLE-SETTLING IN FLUID

An analytical expression can be obtained for the velocity of kinematic shocks (also referred to as concentration shocks). Two shock fronts develop in a settling system as depicted in Fig. 9.1. One of the shocks propagates in the direction of gravity (downward), while the other is aligned with the direction of packing (upward).

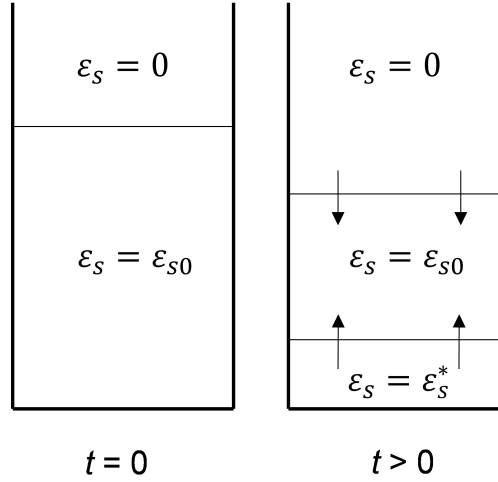


Fig. 9.1: Schematic showing the settling problem.

Settling is governed by the balance between drag, gravity, and buoyancy. Consider the two-fluid model (TFM) system of equations. The phasic continuity equations are given by,

$$\frac{\partial}{\partial t} \rho_g \epsilon_g + \frac{\partial}{\partial x_i} (\rho_g \epsilon_g u_{gj}) = R_g \quad (9.1)$$

$$\frac{\partial}{\partial t} \rho_s \epsilon_s + \frac{\partial}{\partial x_i} (\rho_s \epsilon_s u_{sj}) = R_s \quad (9.2)$$

where, $\rho_g, \epsilon_g, u_{gj}, R_g$ represent density, volume fraction, j^{th} component of velocity and mass source term of the gas-phase respectively. The corresponding terms in the solid phase continuity equations are represented with the subscript s . The phasic momentum equations are given by,

$$\frac{\partial}{\partial t} (\rho_g \epsilon_g u_{gi}) + \frac{\partial}{\partial x_i} (\rho_g \epsilon_g u_{gi} u_{gj}) = -\epsilon_g \frac{\partial P_g}{\partial x_i} + \frac{\partial}{\partial x_i} (\epsilon_g \tau_{gij}) + \beta (u_{si} - u_{gi}) + \rho_g \epsilon_g g_i + S_{gi} \quad (9.3)$$

$$\frac{\partial}{\partial t} (\rho_s \epsilon_s u_{si}) + \frac{\partial}{\partial x_i} (\rho_s \epsilon_s u_{si} u_{sj}) = -\epsilon_s \frac{\partial P_g}{\partial x_i} + \frac{\partial}{\partial x_i} (\epsilon_s \tau_{sij}) + \beta (u_{gi} - u_{si}) + \rho_s \epsilon_s g_i + S_{si} \quad (9.4)$$

P_g, τ_{gij}, S_{gi} represent pressure, shear stress and source term in the gas phase. τ_{sij} contains contributions from inter-particle collisions and S_{si} represents the momentum source term in the solids phase. The following assumptions are made for the settling problem.

1. One-dimensional system
2. Shear stress terms are negligible
3. Particle-particle and particle-wall interactions are negligible
4. Isothermal with no phase change
5. Both the phases are incompressible

Based on these assumptions, the continuity equations Eq.9.1, Eq.9.2 can be combined to give,

$$\frac{\partial}{\partial x}(\epsilon_g u_g) + \frac{\partial}{\partial x}(\epsilon_s u_s) = \frac{\partial j}{\partial x} = 0 \quad (9.5)$$

The notation for velocity components is dropped since one-dimensional analysis is used. It is seen that the volumetric flux, j is a constant for the problem considered. The momentum equations Eq.9.3, Eq.9.4 can be simplified to give,

$$-\frac{\partial P_g}{\partial x} + \frac{\beta}{\epsilon_g} u_r + \rho_g g = 0 \quad (9.6)$$

$$-\frac{\partial P_g}{\partial x} - \frac{\beta}{\epsilon_s} u_r + \rho_s g = 0 \quad (9.7)$$

where, $u_r = u_s - u_g$ is the relative velocity. Subtracting Eq.9.7 from Eq.9.6 gives a relation between the relative velocity, drag function β and acceleration due to gravity as follows,

$$u_r = \frac{g \Delta \rho}{\beta} \epsilon_g \epsilon_s \quad (9.8)$$

where, $\Delta \rho = \rho_s - \rho_g$. The drag function, β is given by,

$$\beta = \frac{3}{4} \frac{\rho_g \epsilon_g \epsilon_s C_D u_r}{d_p} \epsilon_g^{-2.65} \quad (9.9)$$

The drag coefficient for Stokes' law follows,

$$C_D = \frac{24}{Re} = \frac{24 \mu_g}{\rho_g u_r d_p \epsilon_g} \quad (9.10)$$

The final expression for relative velocity considering Stokes' drag law is given by,

$$u_r = \frac{g \Delta \rho d_p^2}{18 \mu_g} \epsilon_g^{3.65} \quad (9.11)$$

The laboratory and travelling frame of references are depicted in Fig. 9.2. The quantities are related as follows:

$$\begin{aligned} u'_{gA} &= u_{gA} + u_{shock}, \\ u'_{gB} &= u_{gB} + u_{shock}, \\ u'_{sA} &= u_{sA} + u_{shock}, \\ u'_{sB} &= u_{sB} + u_{shock} \end{aligned} \quad (9.12)$$

The variables with ' denote the travelling frame of reference. The phasic volumetric fluxes are related by,

$$\begin{aligned} j'_{gA} &= j_{gA} + \epsilon_{gA} u_{shock}, \\ j'_{gB} &= j_{gB} + \epsilon_{gB} u_{shock}, \\ j'_{sA} &= j_{sA} + \epsilon_{sA} u_{shock}, \\ j'_{sB} &= j_{sB} + \epsilon_{sB} u_{shock} \end{aligned} \quad (9.13)$$

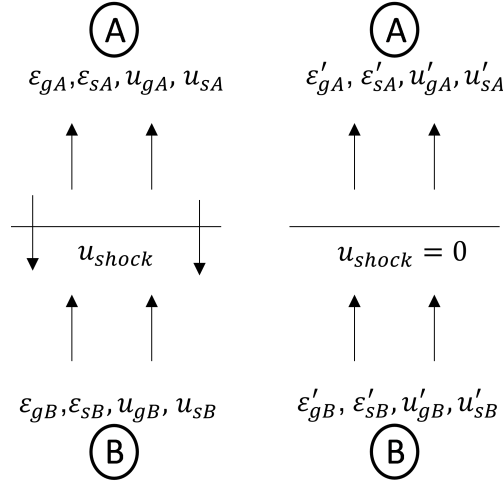


Fig. 9.2: Laboratory (left) and traveling (right) frame of references for the kinematic shock wave.

Since there is no exchange of mass before and after the kinematic shock, additional constraints are obtained as follows,

$$\begin{aligned} \dot{j}'_{gA} &= \dot{j}'_{gB}, \\ \dot{j}'_{sA} &= \dot{j}'_{sB} \end{aligned} \quad (9.14)$$

Simplifying Eq.9.12, Eq.9.13, Eq.9.14, the shock velocity is obtained as,

$$u_{shock} = -\frac{\dot{j}_{sB} - \dot{j}_{sA}}{\epsilon_{sB} - \epsilon_{sA}} \quad (9.15)$$

The phasic volumetric flux, j is related to the total volumetric flux and drift flux [33] as follows,

$$\dot{j}_s = \epsilon_s \dot{j} + \dot{j}_{gs} \quad (9.16)$$

where, the drift flux, \dot{j}_{gs} is related to the relative velocity [33] given by,

$$\dot{j}_{gs} = \epsilon_s (u_s - j) = \epsilon_s \epsilon_g u_r \quad (9.17)$$

Upon further simplification of Eq.9.15 using Eq.9.16 and Eq.9.17, the analytical expression for shock velocity is obtained as follows,

$$u_{shock} = -\left(j + \frac{(\epsilon_s \epsilon_g u_r)_B - (\epsilon_s \epsilon_g u_r)_A}{\epsilon_{sB} - \epsilon_{sA}} \right) \quad (9.18)$$

where, u_r is given by Eq.9.11.

REFERENCES

MMS02 MANUFACTURED SOLUTIONS

The manufactured solutions for the two-phase, 3D, curl-based functions with constant volume fraction are listed below.

Gas pressure:

$$p_g = p_{g0} + p_{gx} \cos(A_{p_{gx}} \pi x) + p_{gy} \cos(A_{p_{gy}} \pi y) + p_{gxy} \cos(A_{p_{gxy}} \pi xy) \\ + p_{gz} \sin(A_{p_{gz}} \pi z) + p_{gyz} \sin(A_{p_{gyz}} \pi yz) + p_{gzx} \cos(A_{p_{gzx}} \pi zx) \quad (1.1)$$

Gas velocity components:

$$u_g = A_{w_{gy}} \pi w_{gy} \cos(A_{w_{gy}} \pi y) + A_{w_{gxy}} \pi w_{gxy} x \cos(A_{w_{gxy}} \pi xy) \\ - A_{v_{gyz}} \pi v_{gyz} y \cos(A_{v_{gyz}} \pi yz) + A_{w_{gyz}} \pi w_{gyz} z \cos(A_{w_{gyz}} \pi yz) \\ + A_{v_{gz}} \pi v_{gz} \sin(A_{v_{gz}} \pi z) + A_{v_{gzx}} \pi v_{gzx} x \sin(A_{v_{gzx}} \pi zx) \quad (1.2)$$

$$v_g = -A_{w_{gxy}} \pi w_{gxy} y \cos(A_{w_{gxy}} \pi xy) + A_{u_{gyz}} \pi u_{gyz} y \cos(A_{u_{gyz}} \pi yz) \\ + A_{w_{gx}} \pi w_{gx} \sin(A_{w_{gx}} \pi x) - A_{u_{gz}} \pi u_{gz} \sin(A_{u_{gz}} \pi z) \\ - A_{u_{gzx}} \pi u_{gzx} x \sin(A_{u_{gzx}} \pi zx) + A_{w_{gzx}} \pi w_{gzx} z \sin(A_{w_{gzx}} \pi zx) \quad (1.3)$$

$$w_g = A_{v_{gx}} \pi v_{gx} \cos(A_{v_{gx}} \pi x) - A_{u_{gyz}} \pi u_{gyz} z \cos(A_{u_{gyz}} \pi yz) \\ + A_{u_{gy}} \pi u_{gy} \sin(A_{u_{gy}} \pi y) + A_{u_{gxy}} \pi u_{gxy} x \sin(A_{u_{gxy}} \pi xy) \\ - A_{v_{gxy}} \pi v_{gxy} y \sin(A_{v_{gxy}} \pi xy) - A_{v_{gzx}} \pi v_{gzx} z \sin(A_{v_{gzx}} \pi zx) \quad (1.4)$$

Solids velocity components:

$$u_m = u_{m0} \left(\frac{\pi}{2} (x + y + z) \right) \quad (1.5)$$

$$v_m = v_{m0} \left(\frac{\pi}{2} (x + y + z) \right) \quad (1.6)$$

$$w_m = w_{m0} \quad (1.7)$$

Gas and solids temperature:

$$T_g = T_{g0} + T_{gx} \cos(A_{T_{gx}} \pi x) + T_{gy} \cos(A_{T_{gy}} \pi y) + T_{gxy} \cos(A_{T_{gxy}} \pi xy) \\ + T_{gz} \sin(A_{T_{gz}} \pi z) + T_{gyz} \sin(A_{T_{gyz}} \pi yz) + T_{gzx} \cos(A_{T_{gzx}} \pi zx) \quad (1.8)$$

$$T_m = T_{m0} + T_{mx} \cos(A_{T_{mx}} \pi x) + T_{my} \cos(A_{T_{my}} \pi y) + T_{mxy} \cos(A_{T_{mxy}} \pi xy) \\ + T_{mz} \sin(A_{T_{mz}} \pi z) + T_{myz} \sin(A_{T_{myz}} \pi yz) + T_{mzx} \cos(A_{T_{mzx}} \pi zx) \quad (1.9)$$

Gas and solids volume fractions:

$$\varepsilon_g = 1 - (\varepsilon_{m0} + \varepsilon_{mx} \cos(A_{\varepsilon_{mx}} \pi x) + \varepsilon_{my} \cos(A_{\varepsilon_{my}} \pi y) + \varepsilon_{mxy} \cos(A_{\varepsilon_{mxy}} \pi xy) \\ + \varepsilon_{mz} \sin(A_{\varepsilon_{mz}} \pi z) + \varepsilon_{myz} \sin(A_{\varepsilon_{myz}} \pi yz) + \varepsilon_{mzx} \cos(A_{\varepsilon_{mzx}} \pi zx)) \quad (1.10)$$

$$\begin{aligned} \varepsilon_m = & \varepsilon_{m0} + \varepsilon_{mx} \cos(A_{\varepsilon_{mx}} \pi x) + \varepsilon_{my} \cos(A_{\varepsilon_{my}} \pi y) + \varepsilon_{mxy} \cos(A_{\varepsilon_{mxy}} \pi xy) \\ & + \varepsilon_{mz} \sin(A_{\varepsilon_{mz}} \pi z) + \varepsilon_{myz} \sin(A_{\varepsilon_{myz}} \pi yz) + \varepsilon_{mzx} \cos(A_{\varepsilon_{mzx}} \pi zx) \end{aligned} \quad (1.11)$$

Solids granular temperature:

$$\begin{aligned} \theta_m = & \theta_{m0} + \theta_{mx} \cos(A_{\theta_{mx}} \pi x) + \theta_{my} \cos(A_{\theta_{my}} \pi y) + \theta_{mxy} \cos(A_{\theta_{mxy}} \pi xy) \\ & + \theta_{mz} \sin(A_{\theta_{mz}} \pi z) + \theta_{myz} \sin(A_{\theta_{myz}} \pi yz) + \theta_{mzx} \cos(A_{\theta_{mzx}} \pi zx) \end{aligned} \quad (1.12)$$

The parameters appearing in the manufactured solutions are as follows:

Table 1.1: Parameters in MMS02 manufactured solutions.

p_{g0}	100.0	v_{gx}	-5.0	w_{m0}	5.0	ε_{m0}	0.3
p_{gx}	20.0	v_{gy}	4.0	T_{g0}	350	ε_{mx}	0.0
p_{gy}	-50.0	v_{gz}	5.0	T_{gx}	10	ε_{my}	0.0
p_{gz}	20.0	v_{gxy}	-3.0	T_{gy}	-30	ε_{mz}	0.0
p_{gxy}	-25.0	v_{gyz}	2.5	T_{gz}	20	ε_{mxy}	0.0
p_{gyz}	-10.0	v_{gzx}	3.5	T_{gxy}	-12	ε_{myz}	0.0
p_{gzx}	10.0	$A_{v_{gx}}$	0.8	T_{gyz}	10	ε_{mzx}	0.0
$A_{p_{gx}}$	0.4	$A_{v_{gy}}$	0.8	T_{gzx}	8	$A_{\varepsilon_{mx}}$	0.5
$A_{p_{gy}}$	0.45	$A_{v_{gz}}$	0.5	$A_{T_{gx}}$	0.75	$A_{\varepsilon_{my}}$	0.5
$A_{p_{gz}}$	0.85	$A_{v_{gxy}}$	0.9	$A_{T_{gy}}$	1.25	$A_{\varepsilon_{mz}}$	0.5
$A_{p_{gxy}}$	0.75	$A_{v_{gyz}}$	0.4	$A_{T_{gz}}$	0.8	$A_{\varepsilon_{mxy}}$	0.4
$A_{p_{gyz}}$	0.7	$A_{v_{gzx}}$	0.6	$A_{T_{gxy}}$	0.65	$A_{\varepsilon_{myz}}$	0.4
$A_{p_{gzx}}$	0.8	w_{g0}	8.0	$A_{T_{gyz}}$	0.5	$A_{\varepsilon_{mzx}}$	0.4
u_{g0}	7.0	w_{gx}	-4.0	$A_{T_{gzx}}$	0.6	θ_{m0}	100.0
u_{gx}	3.0	w_{gy}	3.5	T_{m0}	300	θ_{mx}	5.0
u_{gy}	-4.0	w_{gz}	4.2	T_{mx}	15	θ_{my}	-10.0
u_{gz}	-3.0	w_{gxy}	-2.2	T_{my}	-20	θ_{mz}	12.0
u_{gxy}	2.0	w_{gyz}	2.1	T_{mz}	15	θ_{mxy}	-8.0
u_{gyz}	1.5	w_{gzx}	2.5	T_{mxy}	-10	θ_{myz}	10.0
u_{gzx}	-2.0	$A_{w_{gx}}$	0.85	T_{myz}	12	θ_{mzx}	7.0
$A_{u_{gx}}$	0.5	$A_{w_{gy}}$	0.9	T_{mzx}	10	$A_{\theta_{mx}}$	0.8
$A_{u_{gy}}$	0.85	$A_{w_{gz}}$	0.5	$A_{T_{mx}}$	0.5	$A_{\theta_{my}}$	1.25
$A_{u_{gz}}$	0.4	$A_{w_{gxy}}$	0.4	$A_{T_{my}}$	0.9	$A_{\theta_{mz}}$	0.7
$A_{u_{gxy}}$	0.6	$A_{w_{gyz}}$	0.8	$A_{T_{mz}}$	0.8	$A_{\theta_{mxy}}$	0.5
$A_{u_{gyz}}$	0.8	$A_{w_{gzx}}$	0.75	$A_{T_{mxy}}$	0.5	$A_{\theta_{myz}}$	0.6
$A_{u_{gzx}}$	0.9	u_{m0}	5.0	$A_{T_{myz}}$	0.65	$A_{\theta_{mzx}}$	0.7
v_{g0}	9.0	v_{m0}	5.0	$A_{T_{mzx}}$	0.4		

MMS03 MANUFACTURED SOLUTIONS

The manufactured solutions for the two-phase, 3D, curl-based functions with variable volume fraction are listed below.

Gas pressure:

$$p_g = p_{g0} + p_{gx} \cos(A_{p_{gx}} \pi x) + p_{gy} \cos(A_{p_{gy}} \pi y) + p_{gxy} \cos(A_{p_{gxy}} \pi xy) \\ + p_{gz} \sin(A_{p_{gz}} \pi z) + p_{gyz} \sin(A_{p_{gyz}} \pi yz) + p_{gzx} \cos(A_{p_{gzx}} \pi zx) \quad (2.1)$$

Gas velocity components:

$$u_g = \frac{1}{\varepsilon_g} [A_{w_{gy}} \pi w_{gy} \cos(A_{w_{gy}} \pi y) + A_{w_{gxy}} \pi w_{gxy} x \cos(A_{w_{gxy}} \pi xy) \\ - A_{v_{gyz}} \pi v_{gyz} y \cos(A_{v_{gyz}} \pi yz) + A_{w_{gyz}} \pi w_{gyz} z \cos(A_{w_{gyz}} \pi yz) \\ + A_{v_{gz}} \pi v_{gz} \sin(A_{v_{gz}} \pi z) + A_{v_{gzx}} \pi v_{gzx} x \sin(A_{v_{gzx}} \pi zx)] \quad (2.2)$$

$$v_g = \frac{1}{\varepsilon_g} [-A_{w_{gxy}} \pi w_{gxy} y \cos(A_{w_{gxy}} \pi xy) + A_{u_{gyz}} \pi u_{gyz} y \cos(A_{u_{gyz}} \pi yz) \\ + A_{w_{gx}} \pi w_{gx} \sin(A_{w_{gx}} \pi x) - A_{u_{gz}} \pi u_{gz} \sin(A_{u_{gz}} \pi z) \\ - A_{u_{gzx}} \pi u_{gzx} x \sin(A_{u_{gzx}} \pi zx) + A_{w_{gzx}} \pi w_{gzx} z \sin(A_{w_{gzx}} \pi zx)] \quad (2.3)$$

$$w_g = \frac{1}{\varepsilon_g} [A_{v_{gx}} \pi v_{gx} \cos(A_{v_{gx}} \pi x) - A_{u_{gyz}} \pi u_{gyz} z \cos(A_{u_{gyz}} \pi yz) \\ + A_{u_{gxy}} \pi u_{gxy} x \sin(A_{u_{gxy}} \pi xy) + A_{u_{gy}} \pi u_{gy} \sin(A_{u_{gy}} \pi y) \\ - A_{v_{gxy}} \pi v_{gxy} y \sin(A_{v_{gxy}} \pi xy) - A_{v_{gzx}} \pi v_{gzx} z \sin(A_{v_{gzx}} \pi zx)] \quad (2.4)$$

Solids velocity components:

$$u_m = \frac{1}{\varepsilon_m} \left[u_{m0} \left(\frac{\pi}{2} (x + y + z) \right) \right] \quad (2.5)$$

$$v_m = \frac{1}{\varepsilon_m} \left[v_{m0} \left(\frac{\pi}{2} (x + y + z) \right) \right] \quad (2.6)$$

$$w_m = \frac{1}{\varepsilon_m} w_{m0} \quad (2.7)$$

Gas and solids temperature:

$$T_g = T_{g0} + T_{gx} \cos(A_{T_{gx}} \pi x) + T_{gy} \cos(A_{T_{gy}} \pi y) + T_{gxy} \cos(A_{T_{gxy}} \pi xy) \\ + T_{gz} \sin(A_{T_{gz}} \pi z) + T_{gyz} \sin(A_{T_{gyz}} \pi yz) + T_{gzx} \cos(A_{T_{gzx}} \pi zx) \quad (2.8)$$

$$T_m = T_{m0} + T_{mx} \cos(A_{T_{mx}} \pi x) + T_{my} \cos(A_{T_{my}} \pi y) + T_{mxy} \cos(A_{T_{mxy}} \pi xy) \\ + T_{mz} \sin(A_{T_{mz}} \pi z) + T_{myz} \sin(A_{T_{myz}} \pi yz) + T_{mzx} \cos(A_{T_{mzx}} \pi zx) \quad (2.9)$$

Solids granular temperature:

$$\begin{aligned} \theta_m = & \theta_{m0} + \theta_{mx} \cos(A_{\theta_{mx}} \pi x) + \theta_{my} \cos(A_{\theta_{my}} \pi y) + \theta_{mxy} \cos(A_{\theta_{mxy}} \pi xy) \\ & + \theta_{mz} \sin(A_{\theta_{mz}} \pi z) + \theta_{myz} \sin(A_{\theta_{myz}} \pi yz) + \theta_{mzx} \cos(A_{\theta_{mzx}} \pi zx) \end{aligned} \quad (2.10)$$

The parameters appearing in the manufactured solutions are as follows:

Table 2.1: Parameters in MMS03 manufactured solutions.

p_{g0}	100.0	v_{gx}	-5.0	w_{m0}	5.0	ε_{m0}	0.3
p_{gx}	20.0	v_{gy}	4.0	T_{g0}	350	ε_{mx}	0.06
p_{gy}	-50.0	v_{gz}	5.0	T_{gx}	10	ε_{my}	-0.1
p_{gz}	20.0	v_{gxy}	-3.0	T_{gy}	-30	ε_{mz}	0.06
p_{gxy}	-25.0	v_{gyz}	2.5	T_{gz}	20	ε_{mxy}	0.0
p_{gyz}	-10.0	v_{gzx}	3.5	T_{gxy}	-12	ε_{myz}	0.0
p_{gzx}	10.0	$A_{v_{gx}}$	0.8	T_{gyz}	10	ε_{mzx}	0.0
$A_{p_{gx}}$	0.4	$A_{v_{gy}}$	0.8	T_{gzx}	8	$A_{\varepsilon_{mx}}$	0.4
$A_{p_{gy}}$	0.45	$A_{v_{gz}}$	0.5	$A_{T_{gx}}$	0.75	$A_{\varepsilon_{my}}$	0.5
$A_{p_{gz}}$	0.85	$A_{v_{gxy}}$	0.9	$A_{T_{gy}}$	1.25	$A_{\varepsilon_{mz}}$	0.5
$A_{p_{gxy}}$	0.75	$A_{v_{gyz}}$	0.4	$A_{T_{gz}}$	0.8	$A_{\varepsilon_{mxy}}$	0.4
$A_{p_{gyz}}$	0.7	$A_{v_{gzx}}$	0.6	$A_{T_{gxy}}$	0.65	$A_{\varepsilon_{myz}}$	0.4
$A_{p_{gzx}}$	0.8	w_{g0}	8.0	$A_{T_{gyz}}$	0.5	$A_{\varepsilon_{mzx}}$	0.4
u_{g0}	7.0	w_{gx}	-4.0	$A_{T_{gzx}}$	0.6	θ_{m0}	100.0
u_{gx}	3.0	w_{gy}	3.5	T_{m0}	300	θ_{mx}	5.0
u_{gy}	-4.0	w_{gz}	4.2	T_{mx}	15	θ_{my}	-10.0
u_{gz}	-3.0	w_{gxy}	-2.2	T_{my}	-20	θ_{mz}	12.0
u_{gxy}	2.0	w_{gyz}	2.1	T_{mz}	15	θ_{mxy}	-8.0
u_{gyz}	1.5	w_{gzx}	2.5	T_{mxy}	-10	θ_{myz}	10.0
u_{gzx}	-2.0	$A_{w_{gx}}$	0.85	T_{myz}	12	θ_{mzx}	7.0
$A_{u_{gx}}$	0.5	$A_{w_{gy}}$	0.9	T_{mzx}	10	$A_{\theta_{mx}}$	0.8
$A_{u_{gy}}$	0.85	$A_{w_{gz}}$	0.5	$A_{T_{mx}}$	0.5	$A_{\theta_{my}}$	1.25
$A_{u_{gz}}$	0.4	$A_{w_{gxy}}$	0.4	$A_{T_{my}}$	0.9	$A_{\theta_{mz}}$	0.7
$A_{u_{gxy}}$	0.6	$A_{w_{gyz}}$	0.8	$A_{T_{mz}}$	0.8	$A_{\theta_{mxy}}$	0.5
$A_{u_{gyz}}$	0.8	$A_{w_{gzx}}$	0.75	$A_{T_{mxy}}$	0.5	$A_{\theta_{myz}}$	0.6
$A_{u_{gzx}}$	0.9	u_{m0}	5.0	$A_{T_{myz}}$	0.65	$A_{\theta_{mzx}}$	0.7
v_{g0}	9.0	v_{m0}	5.0	$A_{T_{mzx}}$	0.4		

MMS04 MANUFACTURED SOLUTIONS

The manufactured solutions for the No-slip wall BC, single phase, 3D, curl-based functions are listed below.

Gas pressure:

$$p_g = p_{g0} + p_{gx} \cos(A_{p_{gx}} \pi x) + p_{gy} \cos(A_{p_{gy}} \pi y) + p_{gxy} \cos(A_{p_{gxy}} \pi xy) \\ + p_{gz} \sin(A_{p_{gz}} \pi z) + p_{gyz} \sin(A_{p_{gyz}} \pi yz) + p_{gzx} \cos(A_{p_{gzx}} \pi zx) \quad (3.1)$$

Gas velocity components:

$$u_g = x^2 [A_{w_{gy}} \pi w_{gy} \cos(A_{w_{gy}} \pi y) + A_{w_{gxy}} \pi w_{gxy} x \cos(A_{w_{gxy}} \pi xy) \\ - A_{v_{gyz}} \pi v_{gyz} y \cos(A_{v_{gyz}} \pi yz) + A_{w_{gyz}} \pi w_{gyz} z \cos(A_{w_{gyz}} \pi yz) \\ + A_{v_{gz}} \pi v_{gz} \sin(A_{v_{gz}} \pi z) + A_{v_{gzx}} \pi v_{gzx} x \sin(A_{v_{gzx}} \pi zx)] \quad (3.2)$$

$$v_g = x^2 [-A_{w_{gxy}} \pi w_{gxy} y \cos(A_{w_{gxy}} \pi xy) + A_{u_{gyz}} \pi u_{gyz} y \cos(A_{u_{gyz}} \pi yz) \\ + A_{w_{gx}} \pi w_{gx} \sin(A_{w_{gx}} \pi x) - A_{u_{gz}} \pi u_{gz} \sin(A_{u_{gz}} \pi z) \\ - A_{u_{gzx}} \pi u_{gzx} x \sin(A_{u_{gzx}} \pi zx) + A_{w_{gzx}} \pi w_{gzx} z \sin(A_{w_{gzx}} \pi zx)] \\ + 2x [-w_{g0} - w_{gx} \cos(A_{w_{gx}} \pi x) - w_{gz} \cos(A_{w_{gz}} \pi z) \\ - w_{gzx} \cos(A_{w_{gzx}} \pi zx) - w_{gy} \sin(A_{w_{gy}} \pi y) \\ - w_{gxy} \sin(A_{w_{gxy}} \pi xy) - w_{gyz} \sin(A_{w_{gyz}} \pi yz)] \quad (3.3)$$

$$w_g = x^2 [A_{v_{gx}} \pi v_{gx} \cos(A_{v_{gx}} \pi x) - A_{u_{gyz}} \pi u_{gyz} z \cos(A_{u_{gyz}} \pi yz) \\ + A_{u_{gy}} \pi u_{gy} \sin(A_{u_{gy}} \pi y) + A_{u_{gxy}} \pi u_{gxy} x \sin(A_{u_{gxy}} \pi xy) \\ - A_{v_{gxy}} \pi v_{gxy} y \sin(A_{v_{gxy}} \pi xy) - A_{v_{gzx}} \pi v_{gzx} z \sin(A_{v_{gzx}} \pi zx)] \\ + 2x [v_{g0} + v_{gy} \cos(A_{v_{gy}} \pi y) + v_{gxy} \cos(A_{v_{gxy}} \pi xy) \\ + v_{gz} \cos(A_{v_{gz}} \pi z) + v_{gzx} \cos(A_{v_{gzx}} \pi zx) \\ + v_{gx} \sin(A_{v_{gx}} \pi x) + v_{gyz} \sin(A_{v_{gyz}} \pi yz)] \quad (3.4)$$

Gas volume fraction:

$$\varepsilon_g = 1.0 \quad (3.5)$$

The parameters appearing in the manufactured solutions are as follows:

Table 3.1: Parameters in MMS04 manufactured solutions.

p_{g0}	100.0	v_{g0}	9.0	u_{g0}	7.0	w_{g0}	8.0
p_{gx}	20.0	v_{gx}	-5.0	u_{gx}	3.0	w_{gx}	-4.0
p_{gy}	-50.0	v_{gy}	4.0	u_{gy}	-4.0	w_{gy}	3.5
p_{gz}	20.0	v_{gz}	5.0	u_{gz}	-3.0	w_{gz}	4.2
p_{gxy}	-25.0	v_{gxy}	-3.0	u_{gxy}	2.0	w_{gxy}	-2.2
p_{gyz}	-10.0	v_{gyz}	2.5	u_{gyz}	1.5	w_{gyz}	2.1
p_{gzx}	10.0	v_{gzx}	3.5	u_{gzx}	-2.0	w_{gzx}	2.5
$A_{p_{gx}}$	0.4	$A_{v_{gx}}$	0.8	$A_{u_{gx}}$	0.5	$A_{w_{gx}}$	0.85
$A_{p_{gy}}$	0.45	$A_{v_{gy}}$	0.8	$A_{u_{gy}}$	0.85	$A_{w_{gy}}$	0.9
$A_{p_{gz}}$	0.85	$A_{v_{gz}}$	0.5	$A_{u_{gz}}$	0.4	$A_{w_{gz}}$	0.5
$A_{p_{gxy}}$	0.75	$A_{v_{gxy}}$	0.9	$A_{u_{gxy}}$	0.6	$A_{w_{gxy}}$	0.4
$A_{p_{gyz}}$	0.7	$A_{v_{gyz}}$	0.4	$A_{u_{gyz}}$	0.8	$A_{w_{gyz}}$	0.8
$A_{p_{gzx}}$	0.8	$A_{v_{gzx}}$	0.6	$A_{u_{gzx}}$	0.9	$A_{w_{gzx}}$	0.75

MMS05 MANUFACTURED SOLUTIONS

The manufactured solutions for the Free-slip wall BC, single phase, 3D, curl-based functions are listed below.

Gas pressure:

$$p_g = p_{g0} + p_{gx} \cos(A_{p_{gx}} \pi x) + p_{gy} \cos(A_{p_{gy}} \pi y) + p_{gxy} \cos(A_{p_{gxy}} \pi xy) \\ + p_{gz} \sin(A_{p_{gz}} \pi z) + p_{gyz} \sin(A_{p_{gyz}} \pi yz) + p_{gzx} \cos(A_{p_{gzx}} \pi zx) \quad (4.1)$$

Gas velocity components:

$$u_g = x^3 [A_{w_{gy}} \pi w_{gy} \cos(A_{w_{gy}} \pi y) + A_{w_{gxy}} \pi w_{gxy} x \cos(A_{w_{gxy}} \pi xy) \\ - A_{v_{gyz}} \pi v_{gyz} y \cos(A_{v_{gyz}} \pi yz) + A_{w_{gyz}} \pi w_{gyz} z \cos(A_{w_{gyz}} \pi yz) \\ + A_{v_{gz}} \pi v_{gz} \sin(A_{v_{gz}} \pi z) + A_{v_{gzx}} \pi v_{gzx} x \sin(A_{v_{gzx}} \pi zx)] \quad (4.2)$$

$$v_g = v_{g0} + x^3 [-A_{w_{gxy}} \pi w_{gxy} y \cos(A_{w_{gxy}} \pi xy) + A_{u_{gyz}} \pi u_{gyz} y \cos(A_{u_{gyz}} \pi yz) \\ + A_{w_{gx}} \pi w_{gx} \sin(A_{w_{gx}} \pi x) - A_{u_{gz}} \pi u_{gz} \sin(A_{u_{gz}} \pi z) \\ - A_{u_{gzx}} \pi u_{gzx} x \sin(A_{u_{gzx}} \pi zx) + A_{w_{gzx}} \pi w_{gzx} z \sin(A_{w_{gzx}} \pi zx)] \\ + 3x^2 [-w_{g0} - w_{gx} \cos(A_{w_{gx}} \pi x) - w_{gz} \cos(A_{w_{gz}} \pi z) \\ - w_{gzx} \cos(A_{w_{gzx}} \pi zx) - w_{gy} \sin(A_{w_{gy}} \pi y) \\ - w_{gxy} \sin(A_{w_{gxy}} \pi xy) - w_{gyz} \sin(A_{w_{gyz}} \pi yz)] \quad (4.3)$$

$$w_g = w_{g0} + x^3 [A_{v_{gx}} \pi v_{gx} \cos(A_{v_{gx}} \pi x) - A_{u_{gyz}} \pi u_{gyz} z \cos(A_{u_{gyz}} \pi yz) \\ + A_{u_{gxy}} \pi u_{gxy} x \sin(A_{u_{gxy}} \pi xy) + A_{u_{gy}} \pi u_{gy} \sin(A_{u_{gy}} \pi y) \\ - A_{v_{gxy}} \pi v_{gxy} y \sin(A_{v_{gxy}} \pi xy) - A_{v_{gzx}} \pi v_{gzx} z \sin(A_{v_{gzx}} \pi zx)] \\ + 3x^2 [v_{g0} + v_{gy} \cos(A_{v_{gy}} \pi y) + v_{gxy} \cos(A_{v_{gxy}} \pi xy) \\ + v_{gz} \cos(A_{v_{gz}} \pi z) + v_{gzx} \cos(A_{v_{gzx}} \pi zx) \\ + v_{gx} \sin(A_{v_{gx}} \pi x) + v_{gyz} \sin(A_{v_{gyz}} \pi yz)] \quad (4.4)$$

Gas volume fraction:

$$\varepsilon_g = 1.0 \quad (4.5)$$

The parameters appearing in the manufactured solutions are as follows:

Table 4.1: Parameters in MMS05 manufactured solutions.

p_{g0}	100.0	v_{g0}	9.0	u_{g0}	7.0	w_{g0}	8.0
p_{gx}	20.0	v_{gx}	-5.0	u_{gx}	3.0	w_{gx}	-4.0
p_{gy}	-50.0	v_{gy}	4.0	u_{gy}	-4.0	w_{gy}	3.5
p_{gz}	20.0	v_{gz}	5.0	u_{gz}	-3.0	w_{gz}	4.2
p_{gxy}	-25.0	v_{gxy}	-3.0	u_{gxy}	2.0	w_{gxy}	-2.2
p_{gyz}	-10.0	v_{gyz}	2.5	u_{gyz}	1.5	w_{gyz}	2.1
p_{gzx}	10.0	v_{gzx}	3.5	u_{gzx}	-2.0	w_{gzx}	2.5
$A_{p_{gx}}$	0.4	$A_{v_{gx}}$	0.8	$A_{u_{gx}}$	0.5	$A_{w_{gx}}$	0.85
$A_{p_{gy}}$	0.45	$A_{v_{gy}}$	0.8	$A_{u_{gy}}$	0.85	$A_{w_{gy}}$	0.9
$A_{p_{gz}}$	0.85	$A_{v_{gz}}$	0.5	$A_{u_{gz}}$	0.4	$A_{w_{gz}}$	0.5
$A_{p_{gxy}}$	0.75	$A_{v_{gxy}}$	0.9	$A_{u_{gxy}}$	0.6	$A_{w_{gxy}}$	0.4
$A_{p_{gyz}}$	0.7	$A_{v_{gyz}}$	0.4	$A_{u_{gyz}}$	0.8	$A_{w_{gyz}}$	0.8
$A_{p_{gzx}}$	0.8	$A_{v_{gzx}}$	0.6	$A_{u_{gzx}}$	0.9	$A_{w_{gzx}}$	0.75

BIBLIOGRAPHY

- [1] J.W. Banks, T. Aslam, and W.J. Rider. On sub-linear convergence for linearly degenerate waves in capturing schemes. *Journal of Computational Physics*, 227(14):6985 – 7002, 2008. URL: <http://www.sciencedirect.com/science/article/pii/S0021999108002088>, doi:<https://doi.org/10.1016/j.jcp.2008.04.002>.
- [2] Ryan B. Bond, Curtis C. Ober, Patrick M. Knupp, and Steven W. Bova. Manufactured solution for computational fluid dynamics boundary condition verification. *AIAA Journal*, 45(9):2224–2236, 2007. URL: <https://doi.org/10.2514/1.28099>, arXiv:<https://doi.org/10.2514/1.28099>, doi:10.2514/1.28099.
- [3] C.Y. Wen and Y.H. Yu. Mechanics of fluidization. In *Chemical Engineering Progress Symposium Series*, volume 62, 100–111. 1966.
- [4] Feng Chen, Eric. C. Drumm, and Georges Guiochon. Prediction/verification of particle motion in one dimension with the discrete-element method. *International Journal of Geomechanics*, 7(5):344–352, 2007. URL: <https://ascelibrary.org/doi/abs/10.1061/%28ASCE%291532-3641%282007%297%3A5%28344%29>, doi:10.1061/(ASCE)1532-3641(2007)7:5(344).
- [5] A. Choudhary, C.J. Roy, J. Dietiker, M. Shahnam, and R. Garg. Code verification for multiphase flows using the method of manufactured solutions. In *ASME 2014 4th Joint US-European Fluids Engineering Division Summer Meeting*. August 2014.
- [6] Aniruddha Choudhary, Christopher J. Roy, Edward A. Luke, and Subrahmanya P. Veluri. Code verification of boundary conditions for compressible and incompressible computational fluid dynamics codes. *Computers & Fluids*, 126:153 – 169, 2016. URL: <http://www.sciencedirect.com/science/article/pii/S0045793015003916>, doi:<https://doi.org/10.1016/j.compfluid.2015.12.003>.
- [7] AIAA Standards Committee and others. AIAA Guide for the Verification and Validation of Computational Fluid Dynamics Simulations (G-077-1998). 1998.
- [8] Rahul Garg, Janine Galvin, Tingwen Li, and Sreekanth Pannala. Open-source mfix-dem software for gas–solids flows: part i—verification studies. *Powder Technology*, 220:122 – 137, 2012. Selected Papers from the 2010 NETL Multiphase Flow Workshop. URL: <http://www.sciencedirect.com/science/article/pii/S003259101100502X>, doi:<https://doi.org/10.1016/j.powtec.2011.09.019>.
- [9] Aytekin Gel, Avinash Vaidheeswaran, Jordan Musser, and Charles H Tong. Toward the development of a verification, validation, and uncertainty quantification framework for granular and multiphase flows—part 1: screening study and sensitivity analysis. *Journal of Verification, Validation and Uncertainty Quantification*, 2018.
- [10] U Ghia, K.N Ghia, and C.T Shin. High-re solutions for incompressible flow using the navier-stokes equations and a multigrid method. *Journal of Computational Physics*, 48(3):387 – 411, 1982. URL: <http://www.sciencedirect.com/science/article/pii/0021999182900584>, doi:[https://doi.org/10.1016/0021-9991\(82\)90058-4](https://doi.org/10.1016/0021-9991(82)90058-4).
- [11] Philip M. Gresho and Stevens T. Chan. On the theory of semi-implicit projection methods for viscous incompressible flow and its implementation via a finite element method that also introduces a nearly consistent mass matrix. part 2: implementation. *International Journal for Numerical Methods in Fluids*, 11(5):621–659, 1990. URL: <https://onlinelibrary.wiley.com/doi/abs/10.1002/flid.1650110510>, doi:10.1002/flid.1650110510.

- [12] Reghan J Hill, Donald L Koch, and Anthony JC Ladd. The first effects of fluid inertia on flows in ordered and random arrays of spheres. *Journal of Fluid Mechanics*, 448:213, 2001.
- [13] A.H. Kharaz, D.A. Gorham, and A.D. Salman. An experimental study of the elastic rebound of spheres. *Powder Technology*, 120(3):281 – 291, 2001. URL: <http://www.sciencedirect.com/science/article/pii/S0032591001002832>, doi:[https://doi.org/10.1016/S0032-5910\(01\)00283-2](https://doi.org/10.1016/S0032-5910(01)00283-2).
- [14] Myoungkyu Lee and Robert D. Moser. Direct numerical simulation of turbulent channel flow up to $Re_{\tau} \approx 5200$. *Journal of Fluid Mechanics*, 774:395–415, 2015. doi:[10.1017/jfm.2015.268](https://doi.org/10.1017/jfm.2015.268).
- [15] PF Linden, JM Redondo, and DL Youngs. Molecular mixing in rayleigh–taylor instability. *Journal of Fluid Mechanics*, 265:97–124, 1994.
- [16] R. Liska and B. Wendroff. Comparison of several difference schemes on 1d and 2d test problems for the euler equations. *SIAM Journal on Scientific Computing*, 11(5):621–659, 2003. URL: <https://onlinelibrary.wiley.com/doi/abs/10.1002/flid.1650110510>, doi:[10.1002/flid.1650110510](https://doi.org/10.1002/flid.1650110510).
- [17] Anthony F Mills. *Basic heat and mass transfer*. Prentice hall, 1999.
- [18] William L Oberkampf and Timothy G Trucano. Verification and validation in computational fluid dynamics. Technical Report, Sandia National Laboratories, 3 2002. doi:[10.2172/793406](https://doi.org/10.2172/793406).
- [19] William L. Oberkampf and Christopher J. Roy. *Verification and Validation in Scientific Computing*. Cambridge University Press, 2010. doi:[10.1017/CBO9780511760396](https://doi.org/10.1017/CBO9780511760396).
- [20] Alberto Di Renzo and Francesco Paolo Di Maio. Comparison of contact-force models for the simulation of collisions in dem-based granular flow codes. *Chemical Engineering Science*, 59(3):525 – 541, 2004. URL: <http://www.sciencedirect.com/science/article/pii/S0009250903005414>, doi:<https://doi.org/10.1016/j.ces.2003.09.037>.
- [21] Shane A. Richards. Completed richardson extrapolation in space and time. *Communications in Numerical Methods in Engineering*, 13(7):573–582, 1998. URL: <https://onlinelibrary.wiley.com/doi/abs/10.1002/%28SICI%291099-0887%28199707%2913%3A7%3C573%3A%3AAID-CNM84%3E3.0.CO%3B2-6>, doi:[10.1002/\(SICI\)1099-0887\(199707\)13:7<573::AID-CNM84>3.0.CO;2-6](https://doi.org/10.1002/(SICI)1099-0887(199707)13:7<573::AID-CNM84>3.0.CO;2-6).
- [22] P. J. Roache. Quantification of uncertainty in computational fluid dynamics. *Annual Review of Fluid Mechanics*, 29(1):123–160, 1997. URL: <https://doi.org/10.1146/annurev.fluid.29.1.123>, doi:[10.1146/annurev.fluid.29.1.123](https://doi.org/10.1146/annurev.fluid.29.1.123).
- [23] P. J. Roache and S. Steinberg. Symbolic manipulation and computational fluid dynamics. *AIAA Journal*, 22(10):1390–1394, 1984. URL: <https://doi.org/10.2514/3.8794>, doi:[10.2514/3.8794](https://doi.org/10.2514/3.8794).
- [24] Patrick J Roache. *Fundamentals of verification and validation*. Hermosa Publishers, 2009.
- [25] Christopher J. Roy. Grid convergence error analysis for mixed-order numerical schemes. *AIAA Journal*, 41(4):595–604, 2003. URL: <https://doi.org/10.2514/2.2013>, arXiv:<https://doi.org/10.2514/2.2013>, doi:[10.2514/2.2013](https://doi.org/10.2514/2.2013).
- [26] Christopher J. Roy. Review of code and solution verification procedures for computational simulation. *Journal of Computational Physics*, 205(1):131 – 156, 2005. URL: <http://www.sciencedirect.com/science/article/pii/S0021999104004619>, doi:<https://doi.org/10.1016/j.jcp.2004.10.036>.
- [27] L. Schiller and A. Naumann. Fundamental calculations in gravitational processing. *Zeitschrift Des Vereines Deutscher Ingenieure*, 77:318 – 320, 1933.
- [28] S. Schlesinger. Terminology for model credibility. *Simulation*, 32(3):103–104, 1979. URL: <https://doi.org/10.1177/003754977903200304>, doi:[10.1177/003754977903200304](https://doi.org/10.1177/003754977903200304).
- [29] Dale M Snider. An incompressible three-dimensional multiphase particle-in-cell model for dense particle flows. *Journal of computational physics*, 170(2):523–549, 2001.
- [30] DM Snider and MJ Andrews. The structure of shear driven mixing with an unstable thermal stratification. *Journal of Fluids Engineering*, 118:55–60, 1996.

- [31] Madhava Syamlal, Thomas J. O'Brien, Sofiane Benyahia, Aytekin Gel, and Sreekanth Pannala. Open-source software in computational research: a case study. *Model. Simul. Eng.*, 2008:1:1–1:10, January 2008. URL: <http://dx.doi.org/10.1155/2008/937542>, doi:10.1155/2008/937542.
- [32] A. Vaidheeswaran, J. Musser, and M.A. Clarke. Verification and validation of mfix-pic. Technical Report, U.S. Department of Energy, National Energy Technology Laboratory, 3 2020. doi:10.2172/1618293.
- [33] Graham B Wallis. *One-dimensional two-phase flow*. McGraw-Hill, 1969.
- [34] Yupeng Xu, Jordan Musser, Tingwen Li, Balaji Gopalan, Rupen Panday, Jonathan Tucker, Gregory Breault, Mary Ann Clarke, and William A Rogers. Numerical simulation and experimental study of the gas–solid flow behavior inside a full-loop circulating fluidized bed: evaluation of different drag models. *Industrial & Engineering Chemistry Research*, 57(2):740–750, 2018.
- [35] David L Youngs. Numerical simulation of turbulent mixing by rayleigh-taylor instability. *Physica D: Nonlinear Phenomena*, 12(1-3):32–44, 1984.
- [36] M. V. Zagarola and A. J. Smits. Mean-flow scaling of turbulent pipe flow. *Journal of Fluid Mechanics*, 373:33–79, 1998. doi:10.1017/S0022112098002419.